Biomimetic Antenna Design for an Atmospheric Probe

by

J. Craig Prather

A dissertation submitted to the Graduate Faculty of
Auburn University
in partial fulfillment of the
requirements for the Degree of
Doctor of Philosophy

Auburn, Alabama
August 3, 2019

Keywords: Antenna, Dipole, Flexible Dipole, Biomimetic Design

Approved by

Mark Adams, Assistant Professor of Electrical and Computer Engineering
Stuart Wentworth, Associate Professor of Electrical and Computer Engineering
Lloyd Riggs, Professor of Electrical and Computer Engineering
Thaddeus Roppel, Associate Professor of Electrical and Computer Engineering

Abstract

This dissertation discusses the design and implementation of a biomimetic, flexible antenna system for an airborne atmospheric probe. The antenna is designed for an airborne sensor system known as the GlobalSense eMote. This system is designed to be deployed into areas of atmospheric interest to collect and transmit *in-situ* atmospheric data back to a base station for processing. The eMote operates in an industrial, scientific, and medical band, 902 – 928 MHz. The eMote is designed to replace the larger, more costly environmental data collection devices currently on the market. The antenna system was inspired by the evolution of the maple seed in that it utilizes flexible rotors to autorotate when falling to decrease the fall speed to increase the collection of *in-situ* data. The antennas are dual ribbon dipoles and are implemented into the flexible rotors. This work describes in detail the simulation, design, and testing procedure that was implemented to create the antennas. Careful detail is given to the testing procedure and the results used to validate this work.

Acknowledgments

This work was supported by the National Oceanic and Atmospheric Administration (NOAA) under contract numbers WC-133-15-CN-0071 and WC-133R-16-CN-0113 in collaboration with Mano NanoTechnologies, Inc. Sandia National Laboratories also provided support through hardware testing and demonstrations.

I would like to thank my advisers, Dr. Mark Adams and Dr. Stuart Wentworth, for their advice and guidance on this project. I would also like to thank my fellow group members Haley Harrell, Michael Bolt, Tyler Horten, and Drew Addison for their significant assistance and support on this project.

Thanks also to Dr. Lloyd Riggs who has freely and often provided his time, assistance, and equipment to me for this research.

I would also like to thank my family and friends who have supported me throughout the research and reporting of this work. It would have been quite boring going to get Friday evening (fine, afternoon) beers at Hound without company to talk with and complain to.

Last, but most importantly, my wife, Caitlin, for both tolerating me and being supportive even though I have spent an excessive amount of hours in the office while pursuing this degree.

Contents

List of Figures

List of Tables

List of Abbreviations

Γ	Reflection coefficient
λ	Wavelength
ACARS	Aircraft Communication Addressing and Reporting System
CAD	Computer Aided Design
COTS	Commercial Off-the-Shelf
CP	Circularly Polarized
dB	Decibels
DUT	Device Under Test
FCC	Federal Communications Commission
GNSS	Global Navigation Satellite System
GPS	Global Positioning System
HFSS	High Frequency Simulation Solver
ISM	Industrial Scientific and Medical
MoM	Method of Moments
NOAA	National Oceanic and Atmospheric Administration
PCB	Printed Circuit Board
PIFA	Planar Inverted-F Antenna

RF Radio Frequency

RHCP Right-Hand Circularly Polarized

SBIR Small Business Innovation Research

SOTA State-of-the-Art

TDMA Time Division Multiple Access

VSWR Voltage Standing Wave Ratio

WMO World Meteorological Organization

Chapter 1

Introduction

In contemporary society, evolving communications systems drive a constant need for more advanced antenna designs. When designing a system, both the electrical needs and mechanical needs must be considered and the design teams must work in tandem to ensure both needs are met. Typical parameters of interest that impact system performance include size, weight, and power. Specific electrical parameters of interest include the performance of the antennas, the performance of the sensors, and the lifespan of the batteries. In order to optimize these systems, designers can look to nature for inspiration.

1.1 A Brief Overview of Meteorology and Atmospheric Sensing

Weather is critically important to humanity as it affects both the food production and general livelihood. Before weather prediction tools existed, humans worshipped several weather gods, including one of humanity's earliest civilizations, the Bronze Age Hurrians and later Hittites, who worshipped Teshub [1]. Many civilizations over time even made the weather god, or god of the skies, the head deity in their pantheons including the Hittites, Greeks, Romans, and Norse. Both early and contemporary civilizations and religions prayed and made sacrifices to their gods to have good weather as it impacted most of society.

One of the earliest recorded attempts of humans to attempt some level of meteorology can be found in the ancient Sanskrit texts, the Upanishads, around 3000 B.C.E. where cloud formation and cycles are mentioned [2]. The ancient Greek scholar, Thales of Miletus, in 600 B.C.E. guessed erroneously that the weather could be predicted by the constellations [3]. This was disproved in Aristotle's 350 B.C.E. treatise *Meterology* where he discussed

earth sciences [4]. This is the first known work that attempted to discuss a wide range of meteorological topics utilizing some scientific principles [3].

For nearly 2000 years, little advancement was made on the science of meteorology and atmospheric science until atmospheric measurement devices were first created. Some of the earliest measurements of rain were conducted in Palestine around the 1st century C.E [3]. A physicist, whose exact dates of life are unknown, proposed the idea of a thermoscope, or primitive thermometer [3]. This device was not realized until nearly 1600 when it was created by Galileo [3]. With the advent of devices to accurately measure atmospheric data, further refinements to predictions were made. In 1901, Cleveland Abbe published a paper stating that a numerical model could be made to predict the weather and presented some differential equations to predict some facets of the weather [5]. In 1955, the Joint Numerical Weather Prediction Unit (JNWPU) was created which was the first group to apply computers to create real-time operational numerical weather predictions [6]. A timeline in Figure 1.1 shows some of the important meterological events.

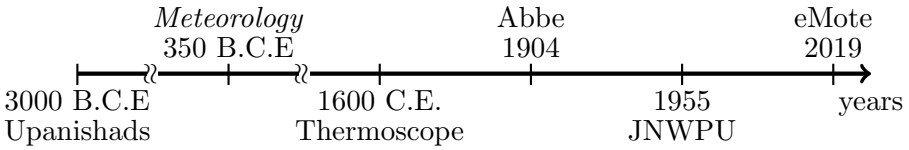

Figure 1.1: Timeline of Important Meteorological Events

1.2 Why New Sensors are Needed

With the improvement in sensors and the advent of computers and sophisticated models, atmospheric scientists have been able to create advanced and surprisingly accurate forecasting models using both directly and indirectly measured data. A significant amount of measured data is needed in order to simulate and verify these models. Atmospheric researchers have come to rely heavily on remote sensing technologies such as satellites and radar to monitor and predict the weather due to the lack of cost-effective sensor systems

that can collect a significant amount of *in-situ* weather data. However, additional *in-situ* measurements are needed to improve weather models and create more accurate forecasts. Current *in-situ* measurements for hurricane reconnaissance primarily rely on devices known as dropsondes, radiosondes, and the aircraft communication addressing and reporting system (ACARS). Dropsondes have a terminal velocity of 11 m/s at sea level and approximately 21 m/s at a 12 km altitude [7], radiosondes are launched with weather balloon systems [8], and ACARS data are collected at altitude during commercial flights [9]. While these systems provide critical *in-situ* data, few radiosondes or dropsondes can operate concurrently, which provides limited measurement density.

Improved forecast accuracy has significant social and economic benefits to society. Weather variability affects more than 3 percent of the United States gross domestic product, [10] and it is estimated that U.S. electric utilities could save $59 million per year with a 1°C improvement in temperature forecasts for scheduling day-ahead electricity generation from conventional power plants [11]. Additionally, improving the ability to accurately measure weather conditions in real time is beneficial to areas with frequent inclement weather. Much of the work in this dissertation was completed at Auburn University, which is located near areas with frequent violent tornadic activity as a recent study has shown that central Mississippi and western Alabama have the longest tracks of F2-F5 tornadoes in the continental United States [12]. An atmospheric measurement system with a higher density of *in-situ* measurements could aid in improving forecast accuracy.

There is a need to make less expensive devices that can be employed in larger numbers to make these *in-situ* measurements. The creation of such devices could have both environmental and economic benefits. One of the major complications with making these devices smaller and lighter is the limitation in appropriate antenna designs. This is the driving force for the antennas designed and demonstrated in this dissertation.

1.3 Global Sense eMote

The antennas were designed for the sensor called the eMote, where the name is a portmanteau of environmental remote sensor. The project is known as GlobalSense and it is a continuation of the work started by Dr. John Manobianco [13, 14] for large-scale environmental sensing. The designed device is a small, light-weight, energy-efficient, environmental probe. A mockup of the eMote system can be seen in Figure 1.2. An image of the final designed GlobalSense eMote can be seen in Figure 1.3. The eMote collects ambient data from pressure, temperature, and humidity sensors along with GPS position and velocity information and then transmits these data back to a receiver base station. The base station is configured of RF front ends which can each receive up to 16 eMotes when they transmit once per second, and the system can be configured to collect data from up to 2080 eMotes simultaneously with a 1 Hz transmission. The eMote is designed to have a low terminal velocity which provides greater dwell time in the atmosphere. The lower mass and slower terminal velocity, compared to other atmospheric sensors, ensure that the eMote will not damage any objects that it interacts with. It is designed for varied weather environments and can be deployed from either the ground via balloon or dropped from an aircraft, manned or unmanned.

In Figure 1.3, it can be seen that the eMote is comprised of a printed circuit board, or PCB, connected to dual asymmetrical rotors containing the antennas. The PCB contains the sensors, Sensirion's SHT25 and Measurement Specialties's MS5803-01BA07, along with the microcontroller and GPS receiver, which are Texas Instrument's CC430F5137 and U-blox's MAX-M8Q, respectively. The PCB also contains a battery holder for a 1/3N type lithium ion battery. The eMote has two antennas which are flexible dipoles; one dipole is designed for the GPS L1 band and the other is designed to operate at the 915 MHz industrial, scientific, and medical radio (ISM) band. The eMote will transmit at a low power in the ISM band so it will not require expensive FCC licensing. The work presented in this dissertation primarily focuses on the antenna design but also highlights some of the collected data.

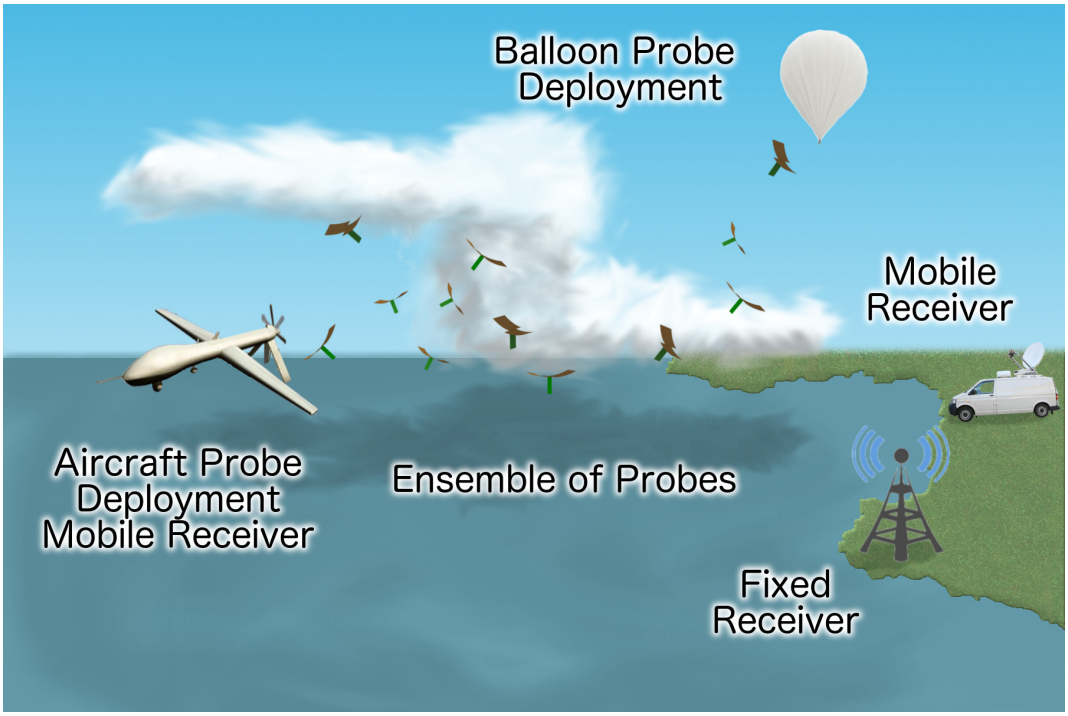

Figure 1.2: Concept of the eMote System

1.4 Research Methodology

A primary goal of the research effort was to dramatically decrease the fall speed without compromising performance which would inherently need some novel solutions to be developed. This led to research on biomimetic designs. The problem solving approach began with a review of current commercial off-the-shelf components and a review of the state-of-the-art in antenna literature. Components were found that could satisfy some of the needs of the project, but there was not a completely developed system to meet all needs. Following this review, the most applicable antenna designs were then modified to match the operational frequencies and desired mechanical demands. This methodology can be seen in Figure 1.4 These designs were then simulated in ANSYS's Electronics Desktop [15] in an iterative fashion until they were tuned to the design frequency and the most promising options were then pursued. Intermediate designs were fabricated in-house using standard photolithographic transfer methods and a LPKF s103 PCB milling machine [16]. The final design was then

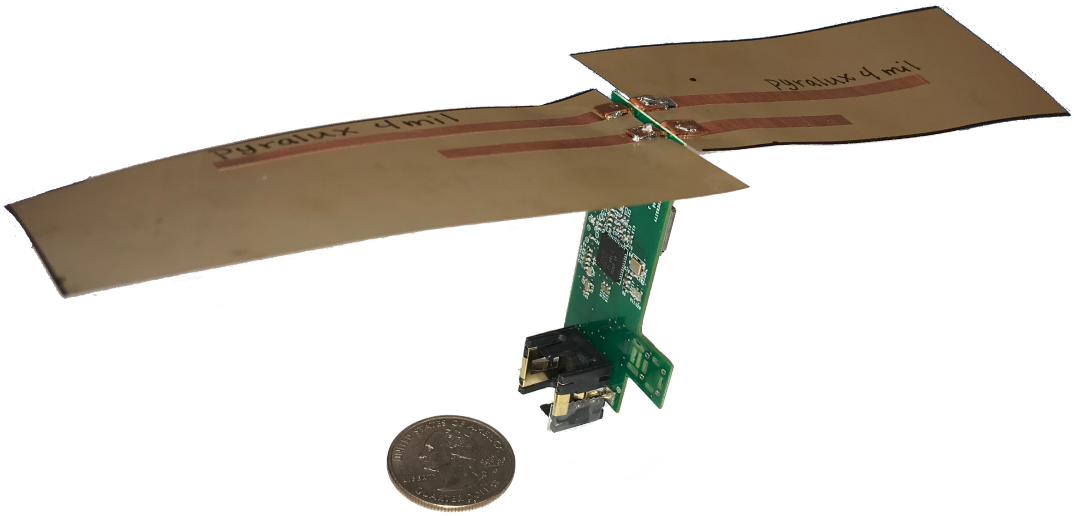

Figure 1.3: Image of Final eMote Design with a U.S. Quarter for Scale

manufactured by a boardhouse and tested in-house. The in-house test equipment was comprised of a network analyzer, Keysight FieldFox N9918A [17], and a spectrum analyzer, Tektronix RSA306B [18]. Antennas were connected to the network analyzer to measure network parameters and the voltage standing wave ratio, VSWR. Then the antennas were tested in an anechoic chamber utilizing both the spectrum analyzer and network analyzer.

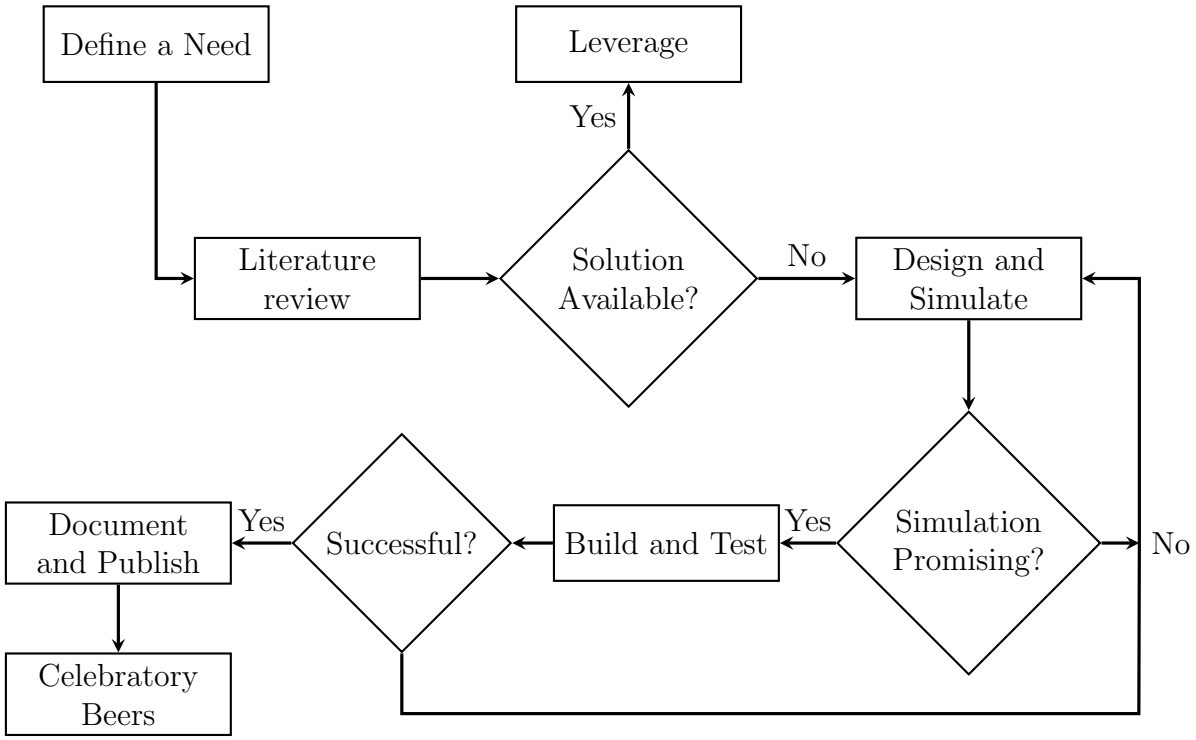

Figure 1.4: Flowchart of Research Methodology

Chapter 2

Background

2.1 Antenna Parameters

For a given antenna application, performance criteria must be established to validate a successful design. This chapter outlines the parameters of interest to the validation criteria, with an emphasis on some used to validate the presented antennas. For a more detailed discussion on basic electromagnetic principles see Wentworth [19], Arthur [20], or Inan, Inan, and Said [21].

2.1.1 S-parameters

While simple at low frequency, measuring device voltages and currents becomes difficult as frequency increases. This is because direct measurements involve the magnitude and phase of the traveling or standing wave [22]. It is therefore more useful to measure power ratios utilizing network parameters known as scattering parameters or S-parameters. S-parameter measurements employ easily realizable loads for characterization [19]. Scattering matrices are often used to characterize multiport networks, particularly at high frequencies, and as such are useful ways to characterize microwave components such as amplifiers, circulators, and oscillators. S-parameters can be easily related to the concepts of reflection, gain, loss, and isolation [19]. The equation below shows the scattering matrix for a two port network.

Theorem 2.1 *Two port scattering matrix*

$$\begin{bmatrix} V_1^- \\ V_2^- \end{bmatrix} = \begin{bmatrix} S_{11} & S_{12} \\ S_{21} & S_{22} \end{bmatrix} \begin{bmatrix} V_1^+ \\ V_2^+ \end{bmatrix}$$

Theorem 2.2 *Abbreviated two port scattering matrix*

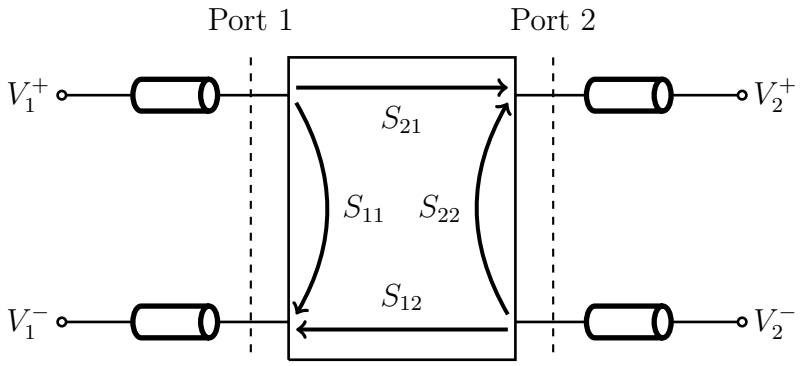

Figure 2.1: Scattering Matrix Formulation

$$\Big[V\Big]^- = \Big[S\Big]\Big[V\Big]^+$$

In a simplified system of the same characteristic impedance, Z_0, the S-parameter, S_{ab}, is defined as the fraction of the voltage waves entering port b that exits port a [19]. For the purposes of antenna design, there are two S-parameters that are of particular interest. One S-parameter that is critical to the design of an antenna is S_{11}. This term, S_{11}, is the reflection coefficient for a single port system, such as an antenna. The reflection coefficient can be defined as the amount of the electromagnetic wave that is reflected due to an impedance mismatch. The derivation can be seen in Theorem 2.3. Γ is the reflection coefficient which is defined in terms of characteristic impedance, Z_0, and load impedance, Z_L.

Theorem 2.3 *Reflection Coefficient*

$$\Gamma = \frac{Z_L - Z_0}{Z_L + Z_0}$$

The load impedance can be calculated in terms of S_{11} and characteristic impedance.

Theorem 2.4 *Impedance of Load*

$$Z_L = \frac{1 + S_{11}}{1 - S_{11}} Z_0$$

Theorem 2.5 *S_{11} for a one Port Network*

$$S_{11} = \frac{Z_L - Z_0}{Z_L + Z_0} = \Gamma$$

By the conservation of energy, the power that is not reflected is either transferred to heat as resistive loss or is radiated by the antenna. S-parameters are typically represented in the logarithmic unit decibels, dB. Measured S_{11} values of less than -10 dB are commonly used to define the effective bandwidth of an antenna as this denotes most of the power is not being reflected to the source. The other S-parameter of interest to a dual antenna design is S_{12} or S_{21}. There is the potential for the signal from one antenna to couple into another antenna, so this parameter shows the isolation between the antennas. The lower the value at the frequency of interest, the better the isolation is between devices. A value below -30 dB is defined as well isolated. Since antennas are reciprocal devices in that they transmit and receive with the same characteristics, S_{12} should be the same as S_{21} when determining coupling. See Figure 2.2 for a diagram of the measurement of S parameters on dual antennas.

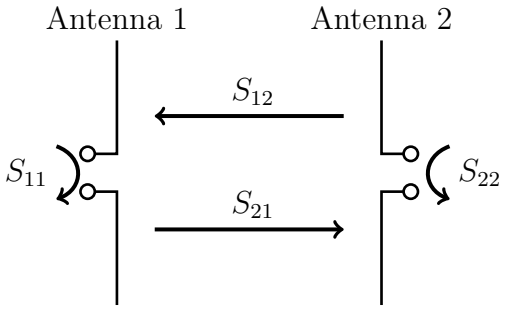

Figure 2.2: Scattering Parameter Measurement on Dual Antennas

The S-parameters are measured using network analyzers. For S_{11} measurements, a single carefully calibrated port connects the network analyzer to the device under test. For S_{12} or S_{21} measurements, the network analyzer undergoes a careful calibration on both ports. The two ports are then connected to the two ports of the device under test.

2.1.2 VSWR

The voltage standing wave ratio (VSWR) is "superposition of the incident and reflected waves" [19] that creates a standing wave.

Theorem 2.6 *Extrema of* V_{max}

$$V_{max} = 1 + |\Gamma_L|$$

$$V_{min} = 1 - |\Gamma_L|$$

The ratio of the maximum and minimum amplitudes is the voltage standing wave ratio.

Theorem 2.7 *VSWR Definition*

$$VSWR = \frac{V_{max}}{V_{min}} = \frac{1 + |\Gamma_L|}{1 - |\Gamma_L|}$$

The magnitude of the reflection coefficient, Γ_L, can range from 0 to 1, therefore VSWR can range from 1 to infinity. This parameter is used, similar to S_{11}, to calculate the effective bandwidth of the designed antenna. The ideal value for the VSWR is at or near 1 indicating very little reflected power and therefore a perfect match between the system and the antenna. This likely means most of the power is being radiated if the antenna has a high efficiency. The antenna is typically deemed to operate in the desired frequency band if the VSWR is less than 2, which correlates to S_{11} approximately less than or equal to -10 dB. For systems where a great match is not as important or very wide bandwidths are needed, a VSWR of less than 3, correlating to S_{11} approximately less than or equal to -6 dB, may be deemed acceptable. Figure 2.3 shows a plot of S_{11} for a preliminary ISM band antenna design.

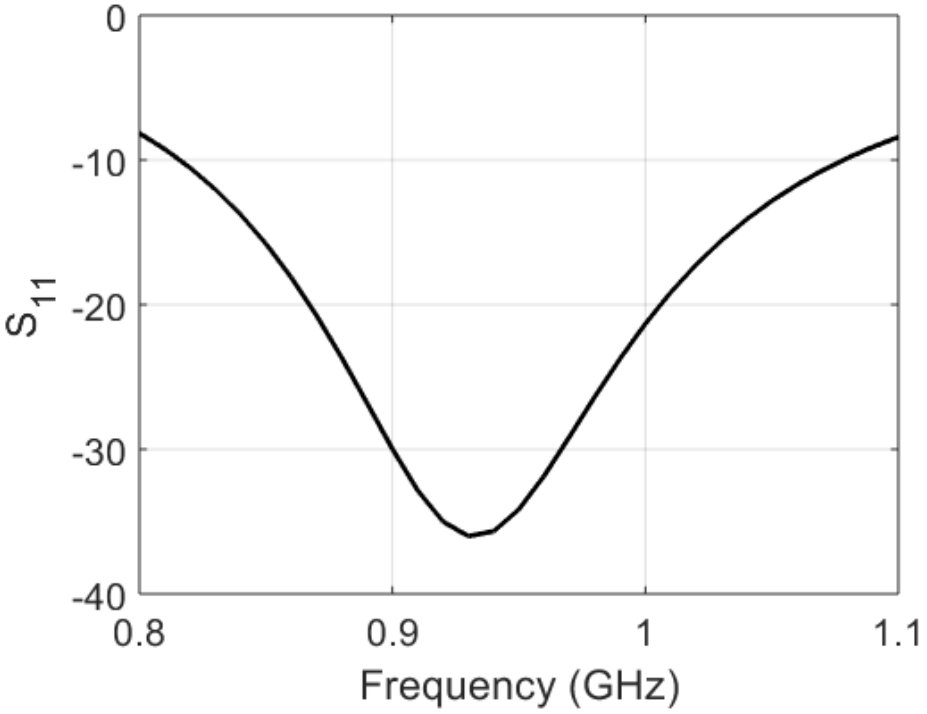

Figure 2.3: Simulated S_{11} Data for an ISM Band Antenna

2.1.3 Radiation Pattern

A radiation pattern, or antenna pattern, is used to visualize how an antenna radiates in a 3 dimensional space. The radiation pattern is often denoted as the far-field pattern as it is the representation of the far-field radiated power. It does not include the near-field reactive properties. The typical analogy used to describe the radiation pattern is a ball of modeling clay [23]. A perfect sphere of modeling clay would represent an isotropic radiation pattern because it radiates the same in all directions. If the sphere is squeezed without adding or removing any clay, then a new pattern is created through the distortion of the clay. To continue the analogy, there is the same amount of clay, but there is more in certain directions than others. Similarly, for an antenna, the total power radiated is the same, but there is more power density in certain directions than others. The radiation pattern can be

expressed in the electric field, E-plane, or the magnetic field, H-plane. The H-plane and E-plane are orthogonal to one another. Figure 2.4 shows the 3 dimensional and 2 dimensional radiation pattern of an antenna simulated in ANSYS HFSS.

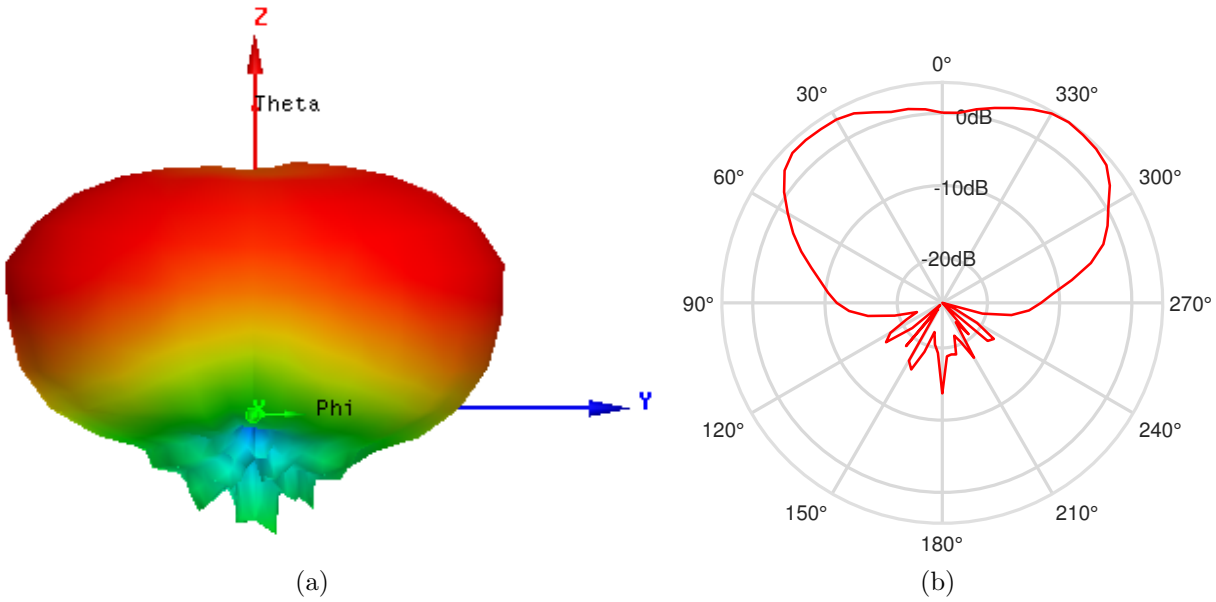

(a) (b)

Figure 2.4: Simulated Antenna Patterns (a) 3D Plot (b) 2D Polar Plot

2.1.4 Directivity and Gain

The directivity of an antenna can be defined as how much the antenna concentrates its radiated energy in a certain direction, or as defined by Stutzman: "the ratio of the radiation intensity in a certain direction to the average radiation intensity" [23]. When the directivity of an antenna is discussed, it is typically defined as the direction of maximum radiation. Directivity of an antenna would be equal to gain if the antenna was a perfectly efficient radiator. In order to properly define directivity of an antenna, the beam solid angle, Ω_A, has to be defined.

Theorem 2.8 *Beam Solid Angle*

$$\Omega_A = \int \int_{sphere} |F(\theta, \phi)|^2 d\Omega$$

The beam solid angle is the surface integral of the radiation pattern, $F(\theta, \phi)$. The radiation pattern is the angular variation of the normalized magnitude of the radiated power around the antenna [23]. This includes directional patterns, shaped main beams, and omnidirectional patterns.

Theorem 2.9 *Directivity*

$$D = \frac{4\pi}{\Omega_A}$$

Directivity is dependent entirely on the shape of the radiation pattern. To find the directivity as a function of the power pattern, $|F(\theta, \phi)|$, the directive gain is used. The maximum value of $|F(\theta, \phi)|$ is unity, the maximum value of directivity as a function of the angle is D [23].

Theorem 2.10 *Directive Gain*

$$D(\theta, \phi) = D|F(\theta, \phi)|^2$$

Unlike directivity, gain is defined by more than just the radiation pattern of the antenna. Gain is defined as the amount of power radiated in a certain direction compared to the amount of power radiated by a perfect isotropic radiator. This takes into account the efficiency and directivity of the antenna. Gain measurements of an antenna do not typically take into account the impedance mismatch or the polarization mismatch [23]. Gain can be empirically defined as:

Theorem 2.11 *Gain*

$$G = \frac{4\pi U_m}{P_m}$$

where U_m and P_m are, respectively, the maximum radiation intensity and the net power accepted by the antenna from the transmitter [23]. When a direction is not specified, the gain of an antenna is typically stated as the maximum gain.

Most antennas are highly efficient radiators, with the exception of electrically small antennas. Radiation efficiency e_r is between 0 and 1 and is defined in Theorem 2.12.

Theorem 2.12 *Radiation Efficiency*

$$e_r = \frac{P_{radiated}}{P_{input}}$$

If the efficiency is not specified, then it is typically assumed to be greater than 90%. Care must be made when reading articles with antennas that undergo techniques to reduce the overall size of the antenna as it typically will reduce the radiation efficiency, and articles often fail to mention the efficiency and only report directivity when efficiency is poor. This was an issue encountered with an initial electrically small antenna design [24]. With this concept in mind, the radiation efficiency must be considered when calculating gain. Therefore, the gain can be approximated as the radiation efficiency multiplied by the directivity [23].

Theorem 2.13 *Gain*

$$G = e_r D$$

The values for the gain and directivity of an antenna are typically expressed with the unit dB. For an antenna, they are normally denoted as the gain or directivity relative to an ideal isotropic radiator (dBi), but are generally just shortened to dB. The maximum gain of a perfectly efficient isotropic antenna would be 0 dB as it radiates the same power in all directions.

2.2 Dipole Antennas

One of the simpler antennas to conceptually understand is the dipole antenna. The simple dipole typically consists of a wire fed at the center. The dipole antenna is often represented and manufactured as 2 wires, as seen in Figure 2.5 with an air gap in the middle. The tip to tip length of the wires sum to slightly less than half a wavelength at the design frequency for the most popular half-wave dipole antenna. Wavelength, λ, is defined in freespace as the speed of light, c, divided by the frequency of interest, f.

Theorem 2.14 *Wavelength*

$$\lambda = \frac{c}{f}$$

Figure 2.5: Dipole Model with Current Path Shown

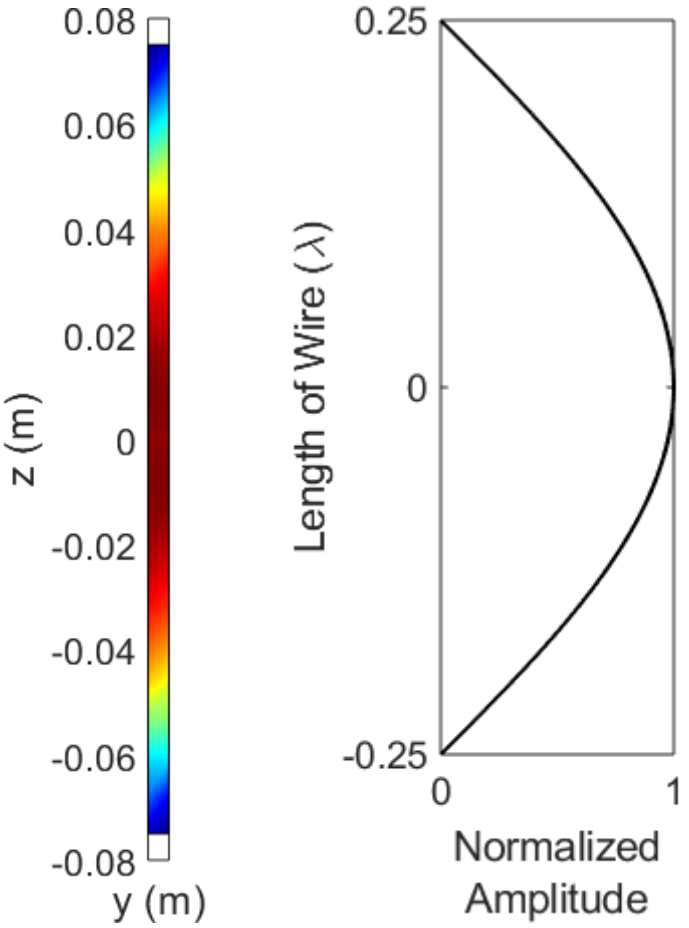

(a) (b)

Figure 2.6: $\lambda/2$ Dipole Current (a) Density (b) Distribution

The basic dipole is simple to construct and model, so it is often used in real world applications. It is relatively simple to visualize how the dipole antenna operates. The current

distribution of a thin $\lambda/2$ linear dipole antenna is maximum at the center, and tapers to zero at the end of the wire. A model of the current distribution of a dipole antenna can be seen in Figure 2.6. This figure was created with MATLAB Antenna Toolbox for a dipole tuned for 1 GHz. The code used to generate this can be seen in Appendix A.2. The figure shows the increased current density with the darker color. From this figure, it can be seen the current could be represented as a curve going from wire tip to wire tip with the maximum at the center and zero at the tips as seen in Figure 2.6. A simple dipole can be manufactured by soldering two wires to an SMA adapter. In Figure 2.7 a dipole designed to operate at the 2.4 GHz ISM band can be seen.

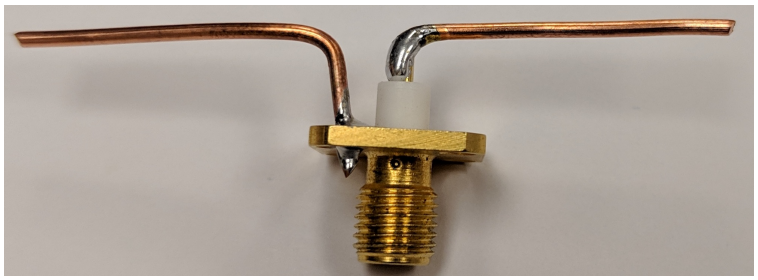

Figure 2.7: 2.4 GHz ISM Band $\lambda/2$ Dipole

2.2.1 Method of Moments

So far, only the $\lambda/2$ dipole has been considered, but other lengths of the dipole can also be analyzed. A method to analytically solve some electromagnetic problems that do not need a closed form solution is Method of Moments (known lovingly as MoM), first presented by Harrington [25]. This method uses an integral equation, casting the induced current as an integral equation where the known current density is part of the integrand. Then Method of Moments, as described below, can be applied to solve for the current density in the integrand and the fields scattered can be found by using radiation integrals [26].

When applying the Method of Moments technique, the object being analyzed is broken into smaller segments, which is called meshing. Each piece of the mesh affects the other pieces of the mesh as the current flows through entire wire. As the current in each segment

of the mesh effects all other segments in the mesh, and vice versa, matrices can be built to describe, the voltage, current, and impedance along the wire [25]. The matrices can then be analyzed and parameters of interest can be found. For more detail on the method of moments, read Harrington's text [25] or Balanis's text [26].

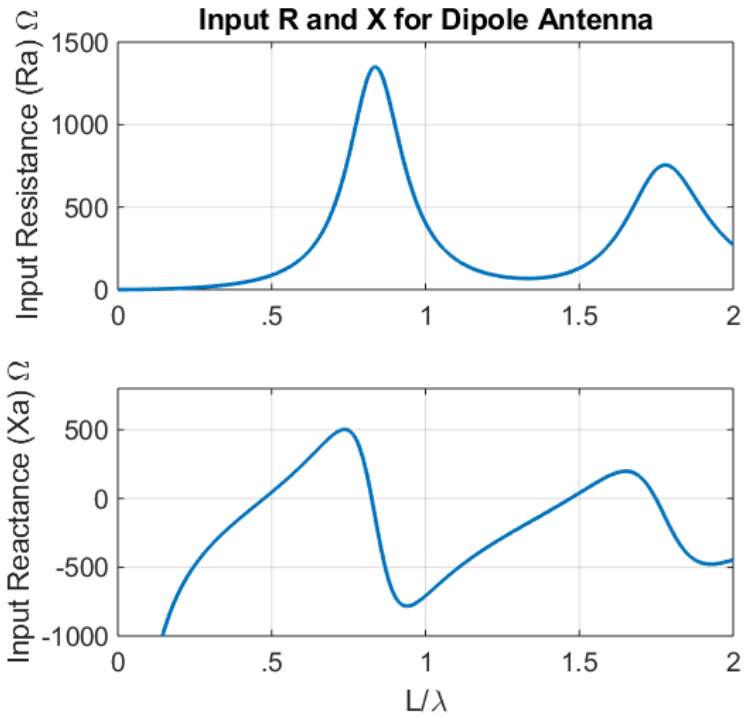

Figure 2.8: Input Impedance for a Center-Fed Dipole Antenna

Method of Moments can be used to analytically explain a few things about the dipole antenna. First consider antenna resonance. An antenna is typically deemed resonant when the complex portion of the impedance is equal to or near 0. At this point, the real portion of the impedance can be matched to the driving structure, which is often 50 Ω.

Theorem 2.15 *Complex Impedance*

$$Z = R + jX$$

Where R is the resistive or real part and X is the complex or reactive part. In Figure 2.8 the real and complex portions of the input impedance components can be seen for a dipole with

a length between 0 and 2 λ. The horizontal axis shows the length of the dipole with respect to a wavelength. It can be noted that slightly below λ equal to 0.5 the complex portion of the impedance is equal to 0. This correlates to a real impedance of approximately 70 Ω for an infinitely thin dipole which is relatively close to the standard system impedance of 50 Ω. A dipole antenna is often designed and tuned by starting with the length of the wire near 0.5 λ and then trimming the ends to tune it. This can be done in simulation or directly by trimming the wire antenna while measuring the antenna impedance. There are other lengths where the dipole input reactance is 0, but the input resistance is farther from 50 Ω making it more difficult to match the real potion of the impedance.

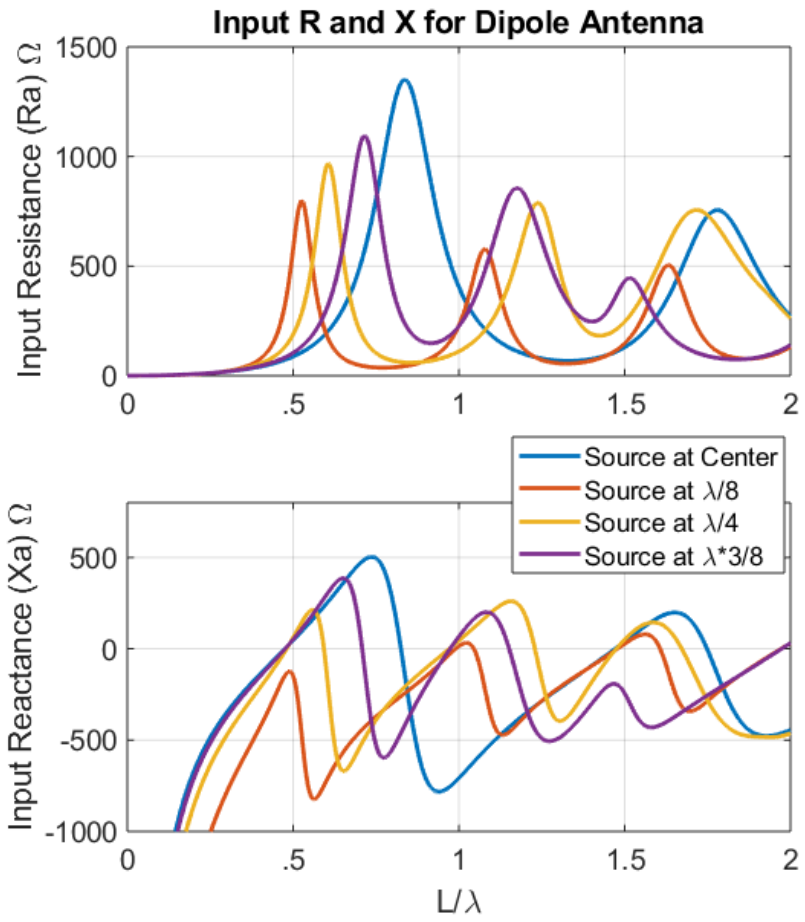

Figure 2.9: Input Impedance for a Dipole Antenna with Varied Feed Locations

Method of Moments also allows for easy simulation of the effects of feeding the antenna at different locations along the wire. Since the dipole works by creating a voltage differential at the ends of the antenna, it is intuitive that the feed should be in the center to allow the current to flow into one feed and out the other. In Figure 2.9 the impedance of a variable length dipole with feeds at different locations can be seen. It is noted that the further away the feed is from the center, the worse the impedance match will be as the wave cannot evenly develop across the antenna. This can be further validated by looking at the VSWR with the feeds at different locations as seen in Figure 2.10.

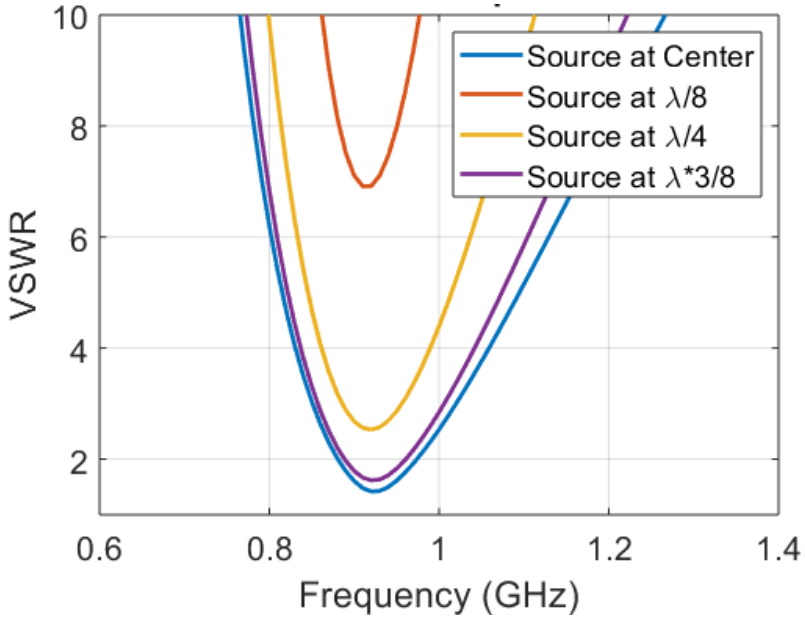

Figure 2.10: Voltage Standing Wave Ratio of a Dipole with Feeds at Different Locations

The resonant bandwidth of a dipole can be increased by widening the dipole [27]. This is validated by simulation as seen in Figure 2.11 and can be confirmed experimentally [23]. Another item of interest is that as the width is increased, the resonant frequency also decreases; therefore the designer must simulate to find how much the length needs to be decreased. The dipole also transitions well to a printed structure, which is sometimes convenient as it is simpler to make using standard printed circuit board, or PCB, techniques.

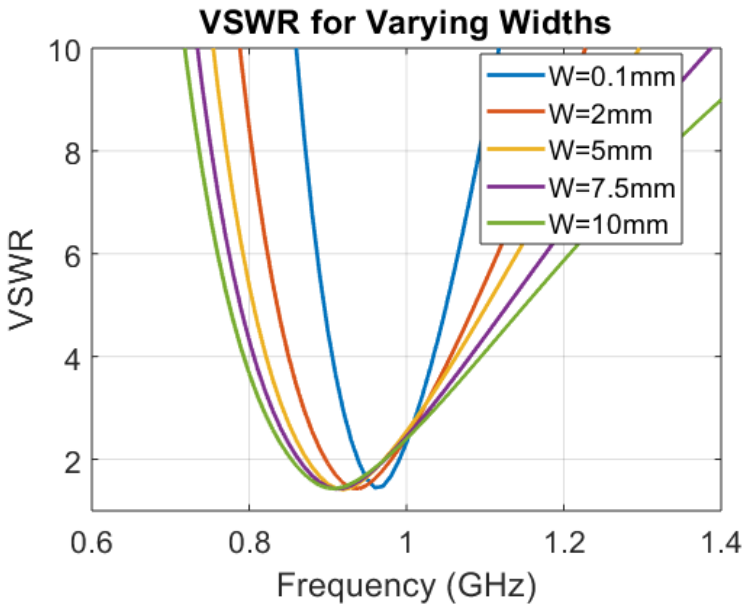

Figure 2.11: Voltage Standing Wave Ratio of a Dipoles with Different Widths

2.3 Microstrip Patch Antennas

A popular antenna is the patch, which is easy to construct and feed with microstrip. This type of antenna is commonly a thin strip of copper on either a rigid or a flexible substrate. Rigid antenna substrates are most common. These may be inexpensive, lower frequency substrates such as FR4 (a flame retardant glass-reinforced epoxy laminate material), or more expensive materials typically designed for higher frequencies such as ceramics and teflon based materials like Rogers RT/Duroid type substrates. Since antenna performance depends on the substrate material properties, the intrinsic parameters of the substrate modify the behavior of the radiating element. The relative permittivity, ϵ_r, called by boardhouses and manufacturers the dielectric constant, D_k, is a critical parameter to the design of a microstrip antenna. Typical relative permittivity values of PCB substrates range from 1 to 10 depending on the material, and the relative permittivity of air is approximately 1.

The effective wavelength of the antenna is determined by the permittivity of the substrate. Increasing the permittivity of the substrate decreases the effective wavelength which

leads to a decrease in the size of a microstrip patch antenna. However, increasing the permittivity will often decrease the bandwidth and efficiency of the antenna if the other design factors are held constant. The bandwidth reduction can be compensated for by increasing the thickness of the substrate [23]. Further decreases in the resonant frequency can be obtained by increasing the permeability of the substrate, up to 30% [28], but higher permeability substrates are not as readily available for PCB design. The choice of substrate type and permittivity provides the antenna designer with another parameter to modify in the antenna design process.

The substrate's loss tangent must be considered when designing RF PCBs. The loss tangent comes from what is known as dielectric dampening, ϵ'', and is related to the complex permittivity of the material [22]. This, coupled with the conductivity, σ, is used to calculate the loss tangent, often denoted as $tan\delta$. A larger loss tangent, as the name implies, will increase the loss in the substrate. This factor is frequency dependent, and in cheaper substrates, such as FR4, can be quite substantial and not uniform when frequencies exceed 1 GHz. Often antenna engineers will rely on more expensive substrates to reduce the loss tangent when efficiency is a concern or for high frequency designs.

There are many common designs and variations of the patch antenna. The simplest design is the $\frac{\lambda}{2}$ rectangular patch [19]. This simple design is easy to implement. More complex designs often necessitate the use of a modeling software [19] such as ANSYS's HFSS or Keysight's Momentum 3D Planar EM Simulator [29]. An antenna simulated in Keysight's Momentum software, utilizing MoM, is shown in Figure 2.12. The current intensities are shown on the antenna where red is the most intense and blue is the least intense. As was done for dipole antennas, the patch may be discretized and the current on each segment could be integrated to determine the radiation pattern.

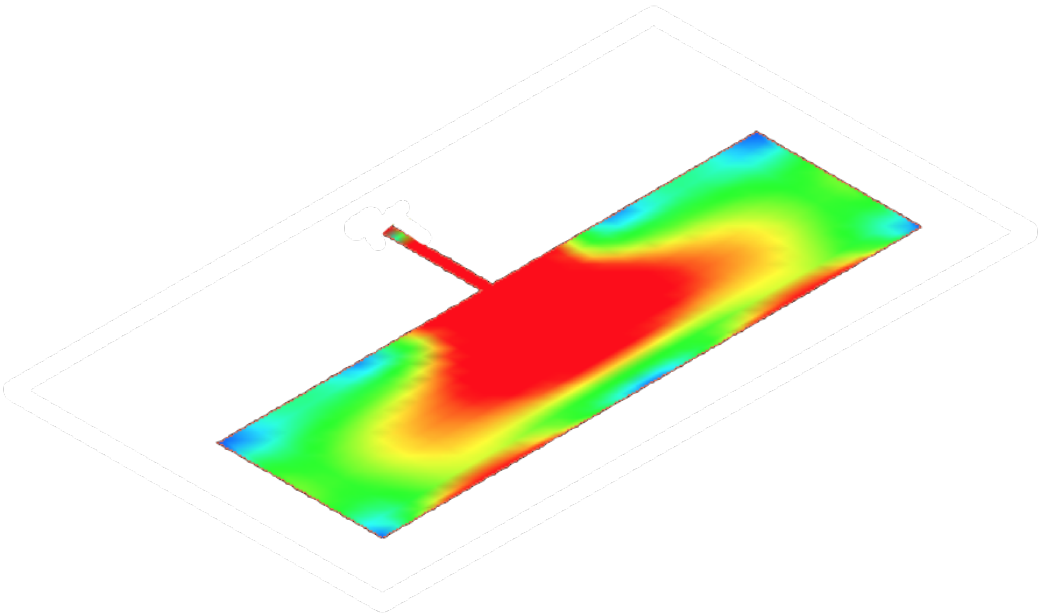

Figure 2.12: $\lambda/2$ Microstrip Patch Antenna Simulated in Keysight's Momentum

2.4 The Design Frequency Bands

Two frequencies were needed for the eMote system. One frequency is the 915 MHz band for transmission to a base station receiver. The other frequency required was for GNSS reception.

2.4.1 GPS/GNSS

The GPS antenna was designed to operate at the GPS L1 band which is centered at 1575.42 MHz [30]. This band was chosen over the L2C centered at 1227.60 MHz [30] and L5C centered at 1176.45 MHz [31] bands as it is the highest frequency band provided, which leads to a smaller final antenna design. Choosing this frequency provides an additional benefit as it is commonly used and there are many commercial receivers available.

The L1 bandwidth is 20.46 MHz centered at 1575.42 MHz. Therefore, the antenna needs to be resonant between 1565.17 and 1585.63 MHz [30]. The GPS L1 signal is right hand circularly polarized, RHCP [30], so any system designed to receive GPS L1 frequencies will

Table 2.1: GNSS L1 Frequency Bands

System	Signal	Center Frequency (MHz)
GPS	L1 C/A	1575.42
GLONASS	L1 C/A	1598
Galileo	L1	1575.42
BeiDou	B1I	1561.098

need a RHCP antenna or accept the loss due to a polarization mismatch. The loss due to a linearly polarized antenna receiving a circularly polarized signal is 3 dB [32].

There are several other Global Navigation Satellite Systems (GNSS) available. The European Space Agency operates Galileo, Russia operates GLONASS, and China operates BeiDou and these systems have satellites which transmit in bands adjacent to the GPS L1C band [33]. Table 2.1 shows transmit bands of nearby systems. Other countries and consortiums, such as India, Japan, Korea, and South America are in the process of developing, or have already developed local augmented GNSS systems [34]. Since many of the different agencies that produce GNSS signals operate in adjacent bands, receivers have been created that can receive the signals from multiple satellite systems.

2.4.2 ISM

The FCC (Federal Communications Commission) offers several unlicensed industrial, scientific, and medical (ISM) bands where users can transmit without obtaining a license if the output power is sufficiently low [35]. The ISM bands were designated to allow for testing and low power applications without the need for costly licensing. Although, devices deployed commercially are required to undergo compliance testing. The ISM band that the eMote system was designed to use is the 902 – 928 MHz band. This ISM band is a International Telecommunication Union Region 2 band which includes the Americas and some of the eastern Pacific Islands [36]. The U.S. regulations on ISM band transmission of a spread spectrum are listed in the FCC regulation 15.247 for frequency hopping and digitally

modulated systems [37]. The antenna must be fixed to the system and cannot be replaced with another antenna after the device has been verified to meet the transmitting requirements. The unlicensed ISM systems are provided no regulatory protection from interference. The maximum field strength at 3 meters is 50 $\frac{mV}{m^2}$ for quasi-peak measurements with the harmonics below $500\frac{\mu V}{m^2}$ (FCC regulation 15.249) [37].

2.5 Literature Review

At the onset of the project, a literature review of the state-of-the-art research was completed as there are no commercial off-the-shelf small antennas available that would fit the needs of this design. Several textbooks were referenced [19, 23, 38, 39] initially to verify the fundamental understanding of electromagnetics and the antenna design process. In the texts, there were several types of antennas referenced that led to the begining of the design process. The first antenna types researched and simulated were the basic $\frac{\lambda}{2}$ [23] and $\frac{\lambda}{4}$ [40] patch antennas. These designs were quickly ruled out because of the large area required for both ground plane and patch element; therefore, this research focused on finding a smaller antenna to minimize the mass and size of the board.

The preliminary design focused on a RHCP GPS L1 band antenna. The first such antenna investigated was the circularly polarized (CP) microstrip antenna by Iwasaki [41]. This antenna design did not radiate at the correct frequency and had a narrow bandwidth. It was deemed, based off of the research presented in the paper, that modifying the operating frequency of the antenna would not provide a large enough bandwidth for successful GPS operation. Similarly, other designs did not have a large enough circularly polarized bandwidth [42, 43, 44]. Research shifted to antennas with a sufficiently large bandwidth for operation. Antennas were considered that did not operate at the desired frequency, as modifications could be made to the antennas to change the resonant frequency. Several designs were found, but most were either too large [45, 46, 47, 48], used special substrate structures not practical for manufacturing [49, 50], or had large air-gaps difficult to implement in an

airborne probe [51, 52]. The final design that had the best compromise of bandwidth, ease of fabrication, and practicality was based on the antenna designed by Chen [53]. Chen's design was not resonant at the GPS L1 frequency band, but was modified to operate at the correct frequency. This was later deemed as too large and heavy so the design was changed to a planar inverted-F antenna (PIFA) as seen in Chapter 3, then a flexible dipole as seen in Chapter 5.

For the ISM band transmit antenna, a linearly polarized design was chosen to minimize antenna size. Several types of antennas were found that could radiate at the desired frequency ranges. The first was a dielectric resonator antenna [54, 55]. This antenna was very interesting and could allow good performance, but the dielectric material adds too much mass and would be difficult to manufacture. Other PCB antenna styles were then analyzed, such as the PIFA [24]. This type of antenna has been utilized in many devices and configurations. The PIFA is commonly found in cell phones [56, 57, 58, 59]. Many modifications of the PIFA have been documented [60, 61] which led to the selection of the PIFA as the basis of first design for the ISM band transmitter. This device was fabricated and tested in the initial prototype before a printed dipole was selected as the final design.

Chapter 3

Initial Design

As quickly learned, the first design typically is not the best solution. This was the case for the design of the first eMote. The initial prototype is discussed in more detail in reference [24]. The initial design was a cap and stem based system where the cap contained the antennas, processor with integrated transmitter, and the GPS receiver. The stem contained the battery and sensors. In Figure 3.1 you can see a CAD model of the original eMote, and in Figure 3.2 you can see the original fabricated eMote. The original plan was to add a lightweight extender to the "cap" to further decrease the fall speed which can be seen in the CAD model. This was a plan that was not followed when the eMote transitioned to a biomimetic design.

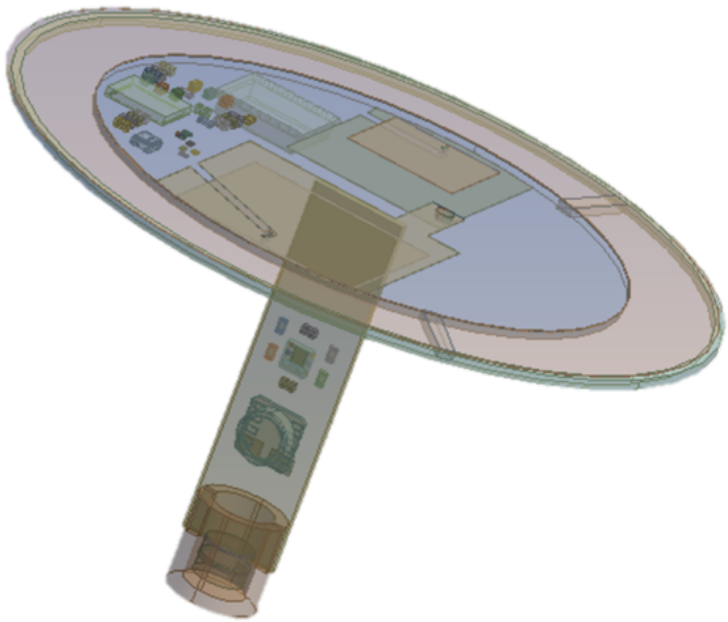

Figure 3.1: CAD Model of eMote Prototype

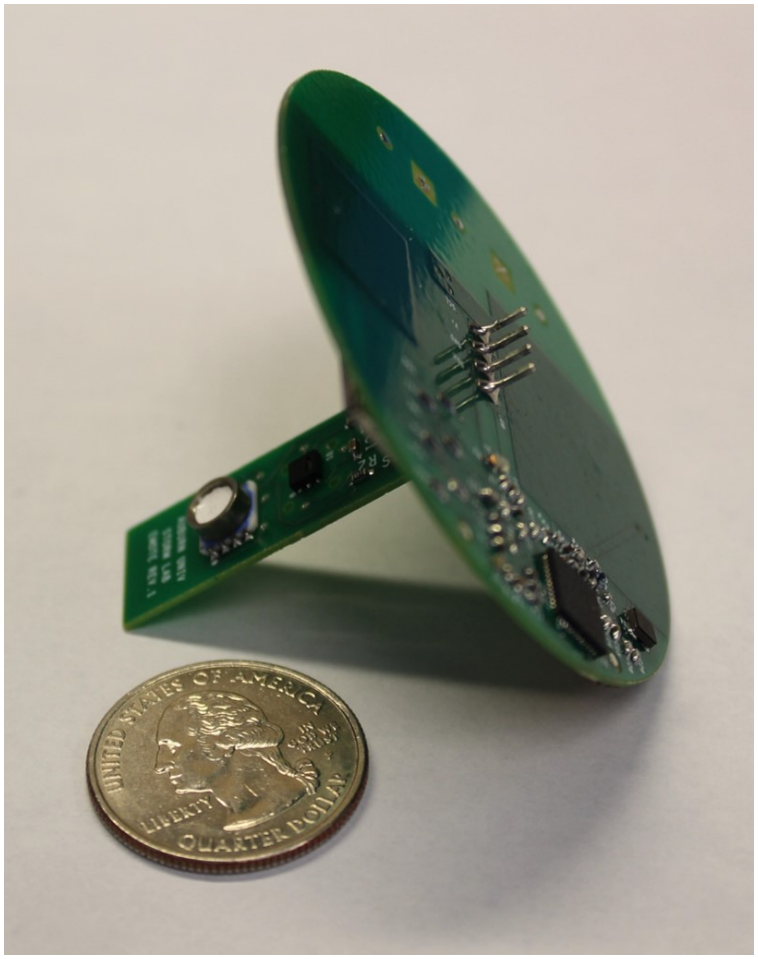

Figure 3.2: Fabricated eMote Prototype with a U.S. Quarter for Scale

The eMote prototype was fabricated on FR4 substrate, specifically Isola Group's 370HR with thickness of 32 mils (0.8 mm). An FR4 type substrate was used to reduce the cost of the eMotes as FR4 is a readily available material which is simple to manufacture and commonly used in electronics. The test results and measured parameters from the prototypes can be seen in Table 3.1. A total of 20 eMotes were fabricated and tested. The fall velocity of the original design was tested by dropping the eMote prototype off the roof of a building on Auburn University's campus. From the limited amount of testing conducted and simulations performed in ANSYS Fluent, it was seen that the device tumbled when falling and had a fall velocity that was too high. Figure 3.3 shows the time evolution of the eMote shape over 0.1 s where a Fluent simulation confirms the tumbling of the "cap-and-stem" design. Simulations

Table 3.1: eMote Prototype Specifications

Design Measurements	**Value**
Size	6 x 4.25 cm
Mass	12 g
Fall Velocity	10 m/s
Measurement Freq	0.5 Hz
Operational Time	<1 hour
Max Range	1 km

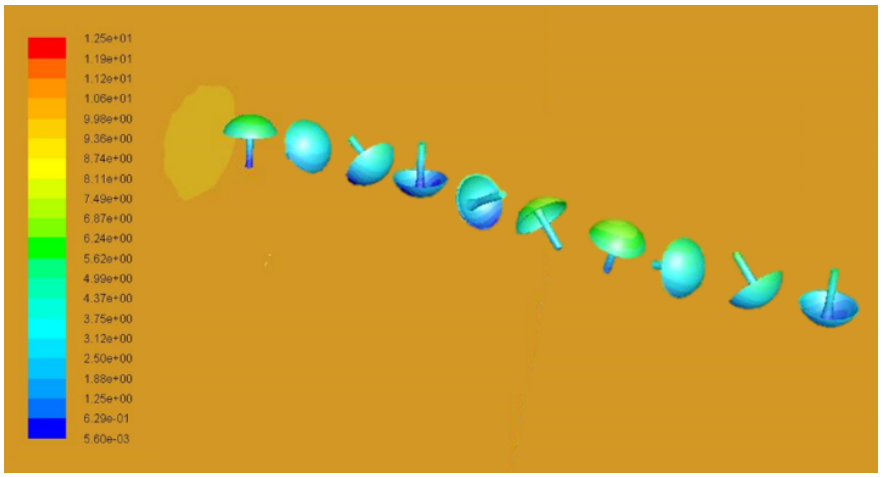

Figure 3.3: Fluent Simulation of Cap and Stem eMote

and empirical testing also showed the prototype eMotes had a tendency to tumble during fall when subject to cross-winds. The operational time was based on using 3 zinc air batteries in series. The max range was tested by pointing an 8.5 dB yagi-uda antenna and tracking the eMote as it was moved away from the receiver.

The antennas were also characterised and validated. The antennas were designed in ANSYS HFSS and they were measured in an anechoic chamber on Auburn University's campus. The design of the antennas was based on a PIFA. A PIFA was created for both the GPS antenna and for the ISM band transmit antenna. The dimensions of the antenna board can be seen in Figure 3.4. The PIFA design was chosen as it was an electrically small antenna that could fit into our designed substrate. The devices also had a nominal amount

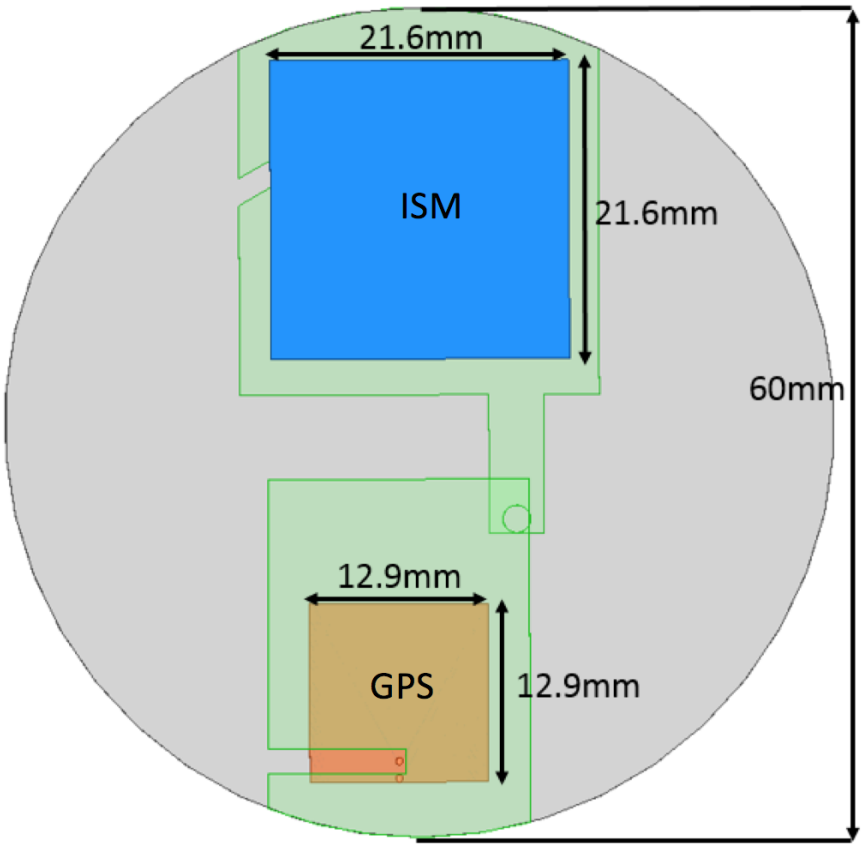

Figure 3.4: Diagram of Antenna PCB with Dimensions

of gain. The pattern for the ISM band PIFA can be seen in Figure 3.5 and the pattern for the GPS band PIFA can be seen in Figure 3.6. The VSWR of the ISM band antenna and the GPS L1 band antenna can be seen in Figures 3.7 and 3.8, respectively. The 3D antenna patterns can be seen in Appendix A.1 and A.2.

The antenna pattern plots show that directivity was achieved in the design. This was desirable for the original envisioned implementation, which would have either a ground based or airborne receiver for the ISM band data transmission. This was a path that was changed during later versions as most of the testing showed the best approach would be to have a receiver located to the side of the eMote.

In order to receive the data transmissions from the eMote, a new antenna system had to be developed. An additional issue with the initial PIFAs was a low radiation efficiency. This was due to both an issue with the layout of the antenna during the fabrication stage,

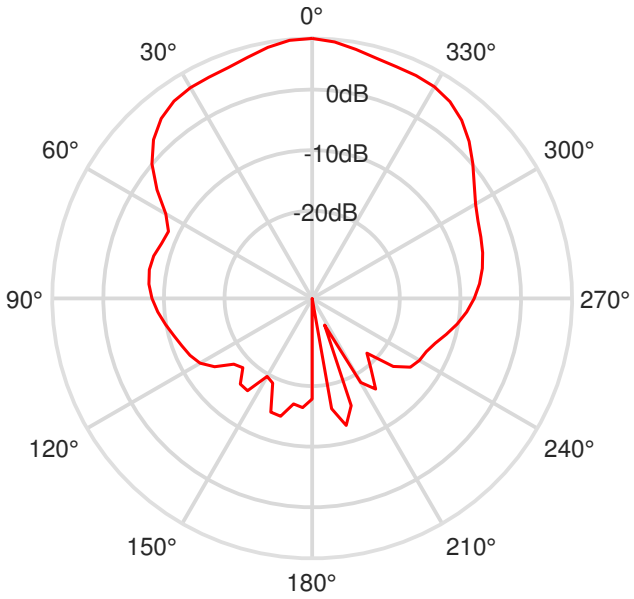

Figure 3.5: Simulated Radiation Pattern of ISM Band PIFA

and an issue with the stated permittivity of the substrate, as outlined in [24]. Another issue encountered with the antenna design was the small bandwidth. The bandwidths worked well for the ISM band transmission and GPS L1 band reception, but the GPS bandwidth was not wide enough to receive other GNSS constellation satellites. Future designs focused on increasing this bandwidth, among other important performance parameters such as fall speed and the prototype eMote tumbling during operation.

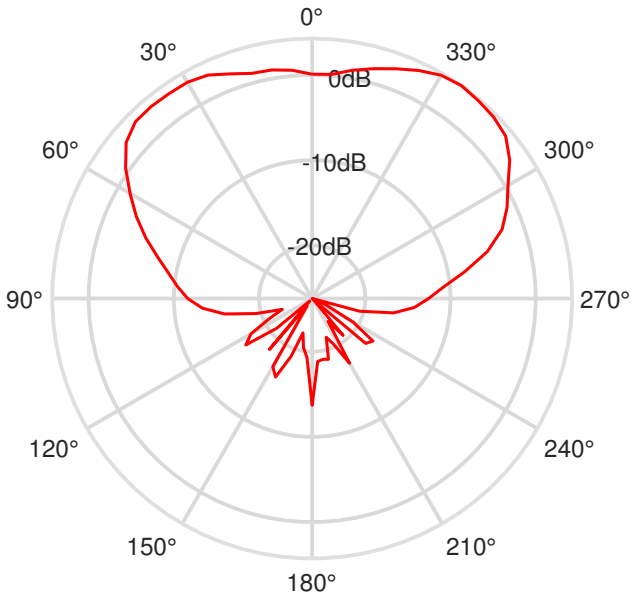

Figure 3.6: Simulated Radiation Pattern of GPS PIFA

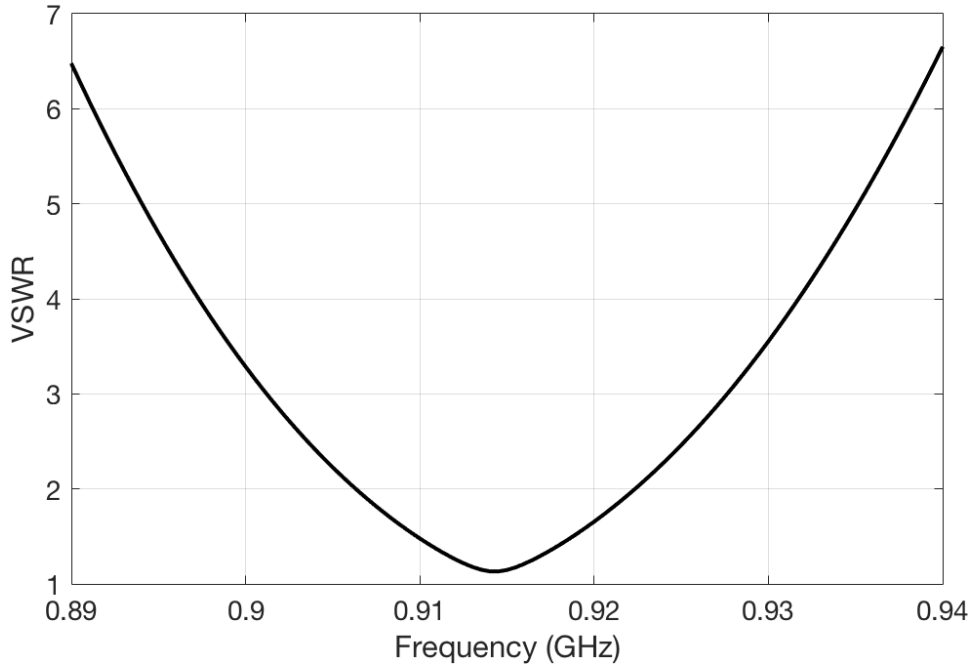

Figure 3.7: Simulated Voltage Standing Wave Ratio of ISM Band PIFA

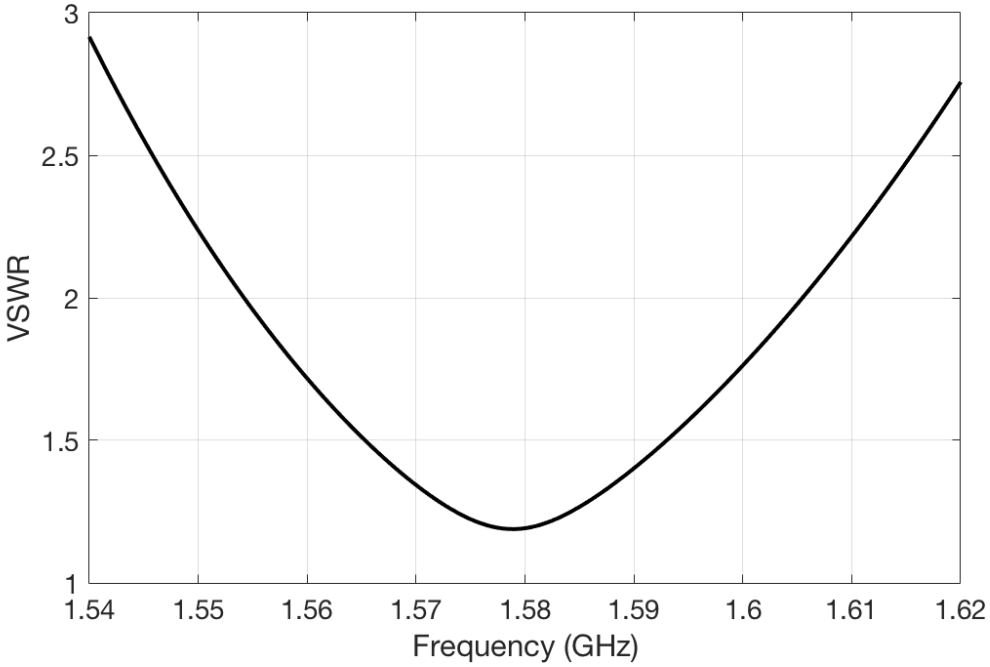

Figure 3.8: Simulated Voltage Standing Wave Ratio of GPS PIFA

Chapter 4

Flexible Dipoles

As mentioned in Chapter 3, the original design involving two PIFAs on an integrated substrate was not sufficient for the eMote system. The initial design had a short maximum range due to both fabrication and design issues. The initial design also fell faster than desired and would tumble when falling. Therefore, the goal was to pivot to a design that could work at longer ranges and be a more robust, efficient antenna structure. This lead to research into flexible dipoles. Dipole antennas were introduced in Section 2.2.

A new approach was needed to solve issues with the initial design, which was a National Oceanic and Atmospheric Administration Phase 1 Small Business Innovation Research (SBIR) grant [62]. The original design goal provided by the sponsor was to create a weather sensor that could be manufactured cheaply and released into violent weather systems, such as tornadoes, to measure the atmosphere until the sensor ceased operation. With this design, it was assumed the receiver would be located on the ground away from the eMote and the range would need to only be a few kilometers. For the Phase 2 SBIR, the goal was to create a system that could be utilized for a wider variety of atmospheric sensing scenarios.

4.1 Review of Printed Dipoles

A review of flexible dipole antennas was conducted prior to embarking on the new antenna design. It was noted that while wire dipoles are an antenna that has been heavily researched and analyzed, very little analysis has been conducted on flexible dipoles. Printed dipoles (also known as ribbon dipoles) are based on the classical dipole antenna but are printed or etched on the substrate [38]. Printed dipoles and monopoles have been utilized to create antennas for compact electronics such as internet-of-things devices [63], cell phones

[64], RFID devices [65], and antenna arrays [66, 67]. Printed dipoles have patterns similar to Hertzian dipoles [68], and have already been successfully integrated on flexible substrates [69, 70]. Another advantage of printed dipoles is that the bandwidth of the antenna can be increased by widening the radiating element [23]. Several of these topics were reviewed with the description of the Method of Moments in Section 2.2.1.

4.2 Design

The flexible dipoles were designed to operate at 1 GHz. This frequency was chosen as it was not too far from the frequencies of the final design and offered a round number. A primary goal for the antennas was to create a device that would be robust and operate over a wider band while achieving a much higher radiation efficiency than the PIFAs previously designed.

4.2.1 Simulation

The simulations to design the antenna were conducted in ANSYS Electronics Desktop (HFSS) and followed an iterative approach. The design started by creating a 1/2 λ thin dipole on the substrate. After noting the insufficient bandwidth, the antenna was widened. As the antenna was widened, the length was decreased to maintain the proper radiation frequency. After a series of simulations and tuning, the final dimensions of dipoles were 4 mm wide with a length of 60 mm per radiating element.

The antenna model can be seen in Figure 4.1. In the figure, the dipole is slightly curved. Since the dipole was designed to operate on a flexible substrate, bending is expected during typical operation. From the bending simulation it was deemed that the bending of the dipole would slightly increase the resonance of the antenna. Section 5.3.3 provides additional information about the change in resonance of a bent dipole. The designed antenna had a bandwidth of approximately 1.02 to 1.14 GHz as seen in Figure 4.2. The radiation pattern

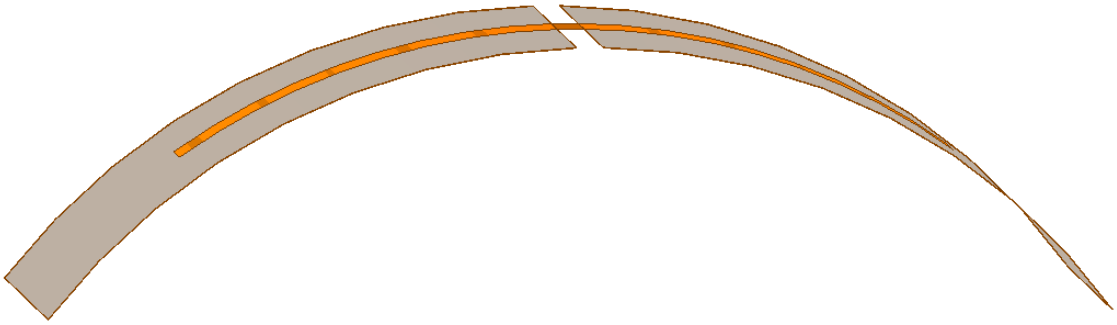

Figure 4.1: Flexible Dipole Model in HFSS

closely matches that of a standard dipole as seen in Figure 4.3. The 3D radiated pattern is provided in Appendix A.3 .

4.2.2 Measured Results

Ten dipoles were fabricated based on the simulation results to radiate at approximately 1 GHz. The dipoles were created on 4 mil thick Pyralux AP and were fabricated in-house utilizing photolithographic transfer and a liquid etchant. A fabricated dipole can be seen in Figure 4.4. The antennas were measured to validate the VSWR and the radiation pattern to ensure that flexible dipoles could be fabricated and used on the eMote.

The VSWR was measured using a Keysight FieldFox N9951A, and the radiation pattern was measured with a Diamond Antenna Measurement Systems DAMS7000 with the FieldFox as the measurement device. All measurements were conducted with calibrated equipment in an anechoic chamber to minimize noise. In Figure 4.2 the VSWR is shown. From the VSWR, the bandwidth was determined to be approximately 0.955 to 1.1 GHz which was a decrease compared to the simulation. It was determined there was a slight over-etching in our fabrication process. The procedure was modified for all future liquid etching processing to account for the over-etching. The radiation pattern was then measured and compared to the simulation which can be seen in Figure 4.3. It was noted that the simulated and measured radiation patterns are reasonably close.

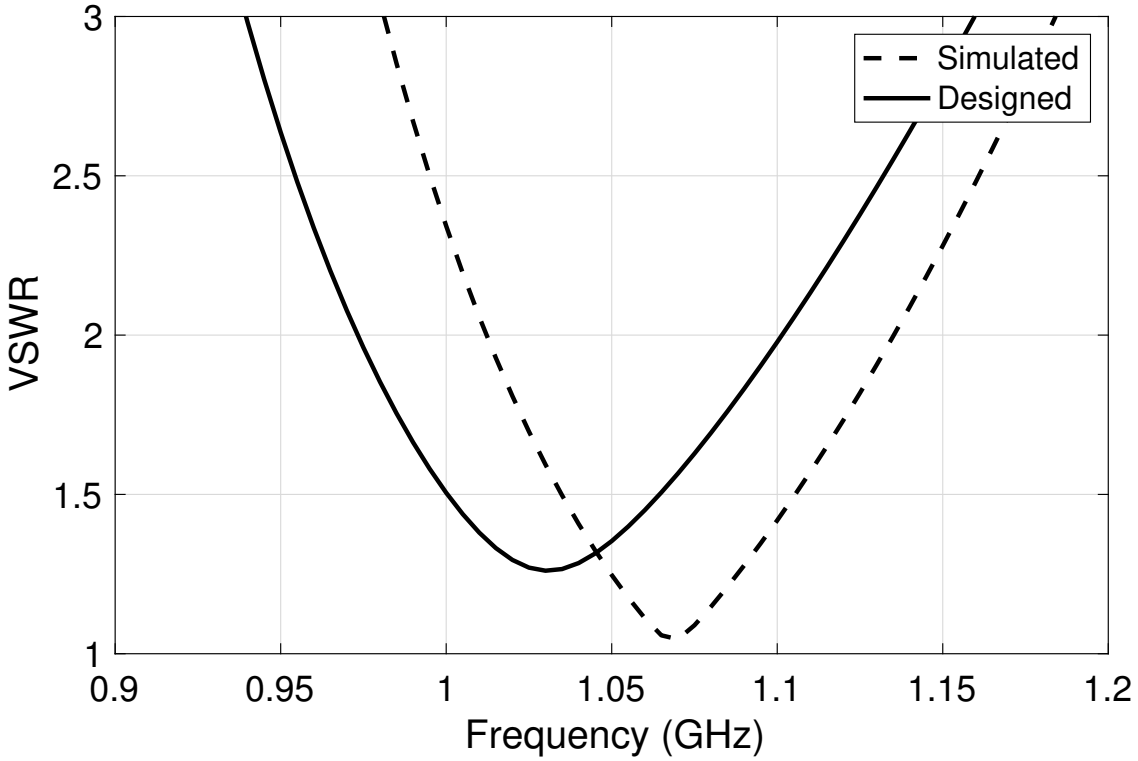

Figure 4.2: Measured and Simulated VSWR of Flexible Dipole

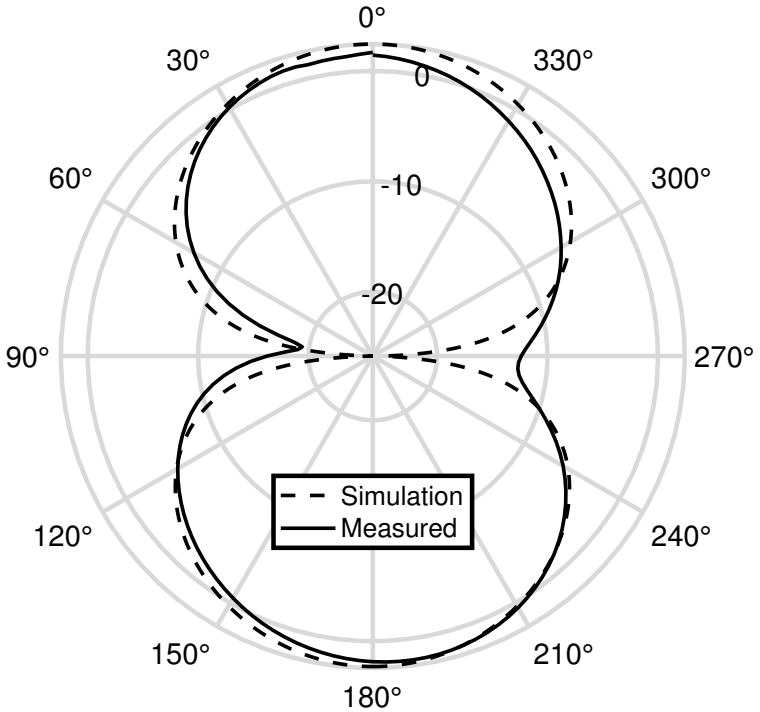

Figure 4.3: Measured and Simulated Radiation Pattern of Flexible Dipole

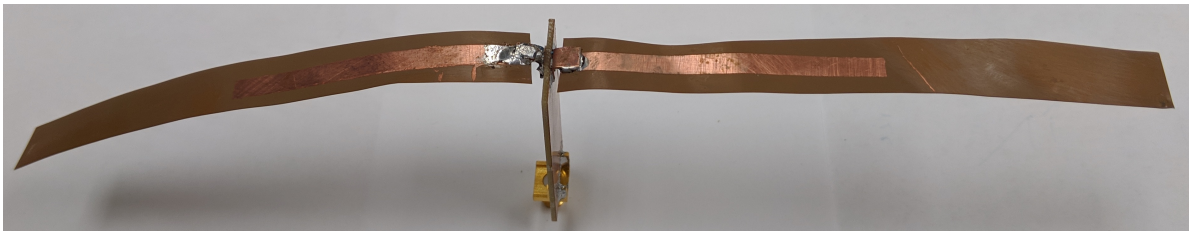

Figure 4.4: Fabricated Flexible Dipole Attached to Measurement PCB

Chapter 5

eMote Design

5.1 System Level

The goal of the GlobalSense system is to collect atmospheric data and transmit this data back to a receiver station. The eMote collects relative humidity, temperature, atmospheric pressure, and GPS data (including position, heading, and speed) which is then transmitted back to a receiver platform. In the revised eMote, the "cap-and-stem" design was dropped for a single PCB design and the final PCB can be seen in Figure 5.1 with the label 113 on it denoting the serial number of the eMote. The sensors utilized are Sensirion's SHT25 for temperature and relative humidity and Measurement Specialties's MS5803-01BA07 for temperature and atmospheric pressure. The microcontroller is Texas Instrument's CC430F5137, which has an integrated cc1101 RF transceiver and the GPS receiver is the U-blox's MAX-M8Q. There is also a 9 degree of freedom IMU on the PCB which may be used for future applications. The sensors all communicate to the microcontroller via I^2C interface. There is a battery holder located at the bottom of the eMote which holds a 1/3N cell lithium battery which provides power through a 3 V regulator. The eMote has 2 push buttons, 3 LEDs and a reed switch. The buttons were configured so that one button resets the eMote and places it in a low power mode and the other button wakes the eMote out of the low power mode and activates all the peripherals. The reed switch is in parallel with the latter button and can also be used to start the eMote or group of eMotes by simply waving a magnet near them. The eMotes were manufactured by Advanced Circuits.

The antennas are then attached to the eMote utilizing copper brackets which are soldered to pads on the PCB. Both the transmitter and the GPS have single-ended (unbalanced)

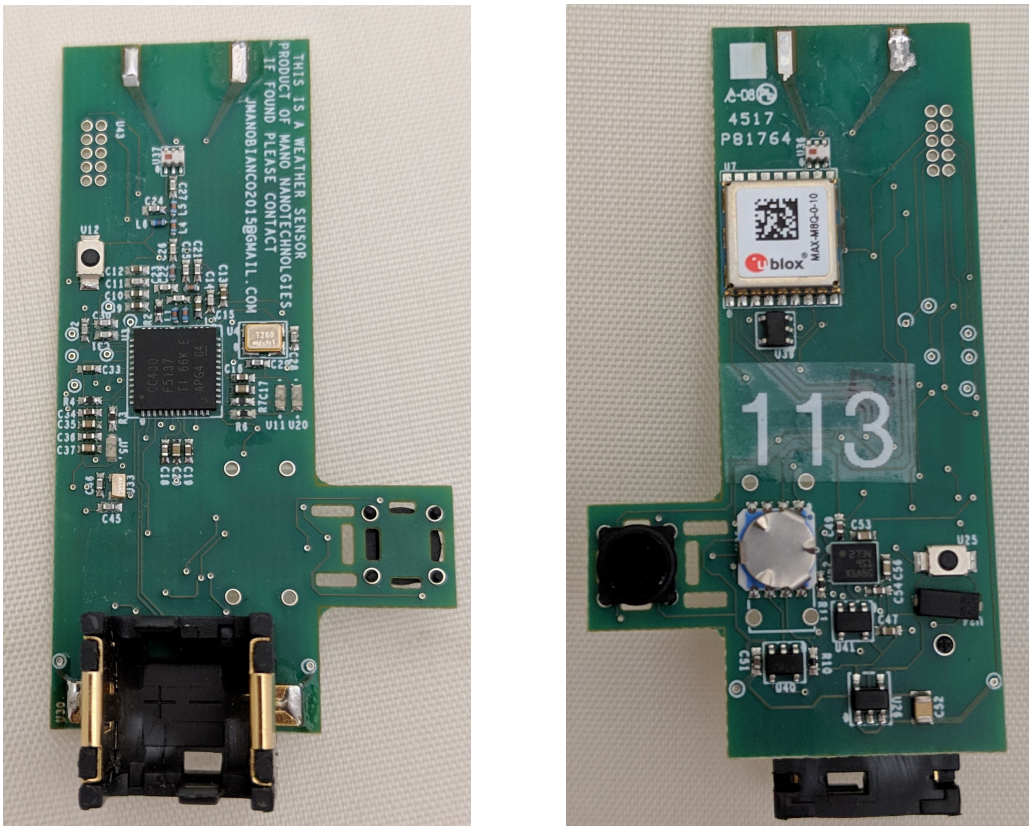

(a) (b)

Figure 5.1: eMote Revised PCB Design (a) Front Side and (b) Back Side

RF inputs and outputs. In order to adapt them to the dipoles, which are a balanced system, baluns were utilized. The baluns selected were wideband, compact ceramic baluns manufactured by Mini-Circuits, part number NCS1.5-232+.

The first revised PCB was designed in Cadence Allegro, and 20 units were manufactured. The first batch was purposefully small in order to correct for issues after testing following an interative design approach. With this group, a few minor issues were addressed, with the primary issue being a slow response from the temperature sensor. This is due to the thermal mass of the eMote leading to a hysteresis in the temperature chamber testing. To reduce the thermal mass seen by the sensor, it was placed on a protrusion isolated from the body by cutouts. Another major improvement was updating the programming interface into the grid of vias at the top of the PCB. 120 units of the final eMote design were then manufactured.

5.2 Mechanical Design

With the original design, the average fall velocity was too high for the device to be deemed successful. This led to a complete redesign of the eMote. In the redesign, careful attention was given to the mechanical design of the structure to decrease the fall speed while maintaining electrical performance.

5.2.1 Biomimetic Inspiration

It is simple to imagine that decreasing the ratio of the mass with respect to surface area of an object should lead to a decreased fall velocity. But, the question is how can that be done without sacrificing critical performance parameters? This inspired a look into methods that have evolved in nature to slow falling objects. The study of using or emulating nature in either the production or implementation of systems is known as biomimicry.

Several products and systems have been developed that use biomimicry in an attempt to create a more useful device. Researchers have created walking robots [71, 72] utilizing biomimetics for their designs. Vibrissae have been implemented into systems to provide haptic feedback [73]. Government programs such as the DARPA Nano Air Vehicle program [74] have also funded biomimetic designs for specific applications. Biomimetic design has also seen some limited application in antennas to minimize the size of arrays [75, 76].

The design of the system was inspired by the evolution of the maple seed, which is a type of winged fruit, known as a samara. The samara evolved to provide the tree with a method of distributing seeds in a unique way by rotating and drifting in the wind [77, 78]. In Figure 5.2 you can see a photo of maple seeds found while hiking in Providence Canyon, Georgia. In this image, you can see several seeds with the wing on one side and the heavy seed on the other.

Figure 5.2: Photograph of Maple Seeds

During the literature review, a device was found that mimicked the design of the single winged samara [79]. This device's physical design showcased elegant characteristics that could be easily adapted to electronics and served as the inspiration for future design iterations. Issues with this device were found as the fall speed, mass, and complicated construction did not meet the demands of eMote. Another difficulty was that a single winged samara would not work well with the anticipated electrical system. The antenna/rotor structure design focused on the asymmetrical two-winged samara found in fossils [80].

By decreasing the mass and increasing the drag forces, the device falls slower. The revised design was inspired by the samara, which has evolved to fall and drift with a low terminal velocity. The evolution of the maple seed shows that greater asymmetry yields better auto-rotation of the seed [80, 81]. This auto-rotation allows increased wing loading of the rotating device due to the leading edge vortices generated by the spinning wings [82]. The auto-rotation provides more stability in turbulent conditions [83], thereby hindering tumbling during free-fall.

This biological structure inspired the creation of printed dipoles, or ribbon dipoles, on thin flexible substrates to emulate the wings of a maple seed. The eMote emulates the maple seed in that the antennas of the eMote operate as the rotors, and the battery located at the bottom of the eMote creates the low center of gravity. The eMote system weighs about 11 g, of which the battery with its container constitutes about 5 g, or nearly half of the total system weight.

5.2.2 Rotor Design

In the eMote system, the flexible substrate serves as both the rotor mechanism and the substrate for the antennas. Thus, antennas were designed to meet both the mechanical and electrical needs of the system. Different designs were fabricated and tested to create a structure that would enter autorotation when falling to minimize fall speed. After small scale preliminary drop testing was completed, four different wing sizes were created for larger

scale testing. The sizes were A, $A+$, B, and $B+$ where rotors A and $A+$ had the same length but differing widths and rotors B and $B+$ had the same lengths but differing widths. The dimensions of each can be seen in Table 5.1 and Figure 5.3 along with the dimensions of the radiating elements for the Pyralux AP substrate, which were held constant across wing sizes.

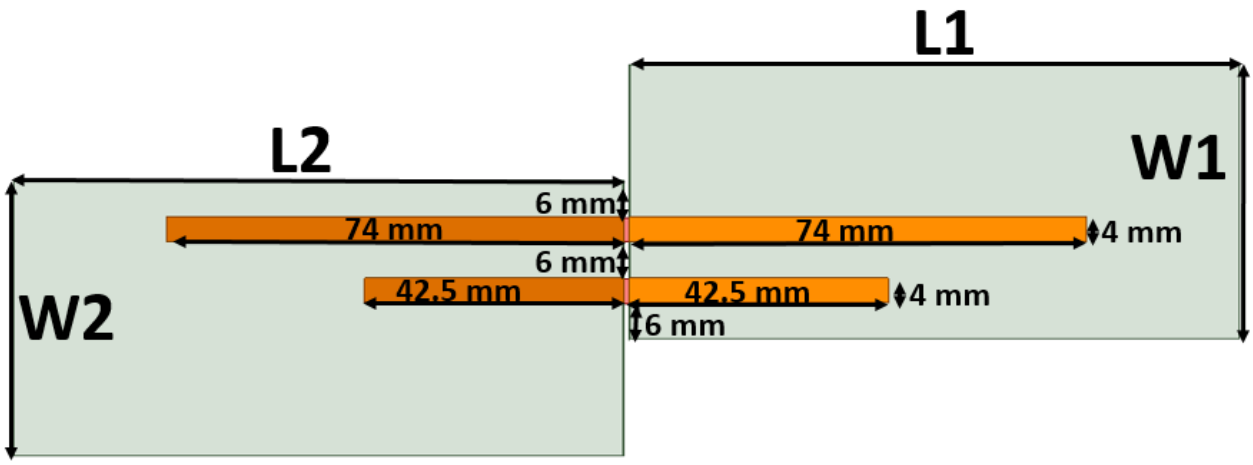

Figure 5.3: Dimensions of Asymmetric Tested Antennas

Table 5.1: Sizes of Tested Rotors

Type	**L (mm)**	**W (mm)**
A	100	45
A+	100	60
B	130	45
B+	130	60

Several different types of materials were tested to find the best combination of price, RF properties, and mechanical properties. The antennas were fabricated on materials that were selected for both their flexibility and ability to operate as antenna substrates. The materials

selected were Rogers Corporation's Ultralam, DuPont's Pyralux AP, and DuPont's Pyralux TK. Several different thicknesses were selected for the drop testing to find the ideal balance between rigidity and flexibility.

The first material tested was a Rogers Corporation substrate as they are well known for their quality RF capable substrates. The Rogers Ultralam material was a liquid crystalline polymer, or LCP, based substrate [84]. It was a thin, flexible material with both sides clad in copper. It had a permittivity, or dielectric constant, of 3.14 and a loss tangent of 0.0025. Since it was an LCP, the dielectric was a white material and an image of a fabricated antenna on Ultralam can be seen in Figure 5.4. Another advantage of Ultralam was the low moisture absorption. Due to a combination of test results, comparatively high costs, and the mention by a sales engineer that the material was soon to be discontinued, this material was not selected for the final design.

The next two materials investigated where DuPont's Pyralux AP [85] and DuPont's Pyralux TK [86]. The Pyralux AP material is a double-sided, copper-clad laminate with an all polyimide (Kapton) composite bonded to copper foil. This is a robust film which has a low moisture absorption. With this material, the copper is well affixed to the polyimide underlay which makes it slightly more difficult to etch than other materials as it is difficult to ablate with lasers, therefore it must be chemically etched. This is advantageous for the eMote application as it will prevent the copper microstrip antennas traces from delaminating from the underlay during operation.

The Pyralux TK material is a similar to the Pyralux AP material, but with the addition of a fluoropolymer (Teflon) layer between the polyimide and the copper foil. The addition of this layer is to provide better high frequency performance as the Teflon provides a lower loss tangent along with other desirable high frequency properties. This was the last material that was investigated. It was found to have a similar performance to the Pyralux AP for flight testing, except Teflon layer causes the copper to more readily delaminate from the underlay. Additionally, the substrate is more expensive than the Pyralux AP. As the eMote antennas

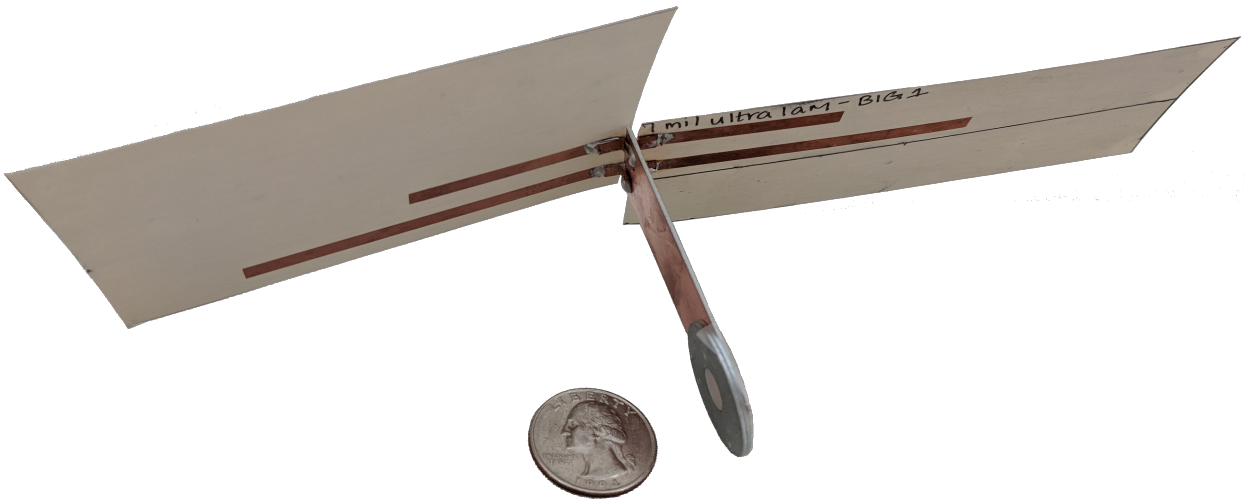

Figure 5.4: Drop Test Unit With A,A+ 7 mil Ultralam Rotors and Quarter for Scale

operate at frequencies that are relatively low, the decreased loss tangent did not overcome the disadvantage of cost and the increased propensity to delaminate.

5.2.3 Rotor Fabrication

The rotors were fabricated utilizing standard photolithography techniques. The photoresist was DuPont Riston MultiMaster MM115 series which is a roll type material that is laminated with heat and pressure to the substrate. This is a negative type photoresist which means that the portions that are exposed become crosslinked polymerized, and more difficult to dissolve in developer, thereby leaving the exposed copper behind when etched. The photresist was exposed with a flip-top UV system and then developed and etched with a Keepro liquid Etching System. A processed antenna on Pyralux AP can be seen in Figure 5.5.

5.2.4 Drop Testing

In order to test the initial rotor and antenna structure designs, mock-ups of the antennas on flexible substrates were fabricated and attached to 0.8 mm thick, 11 mm wide by 60 mm long FR4 boards that were the same size as the designed eMote modules. The FR4 boards

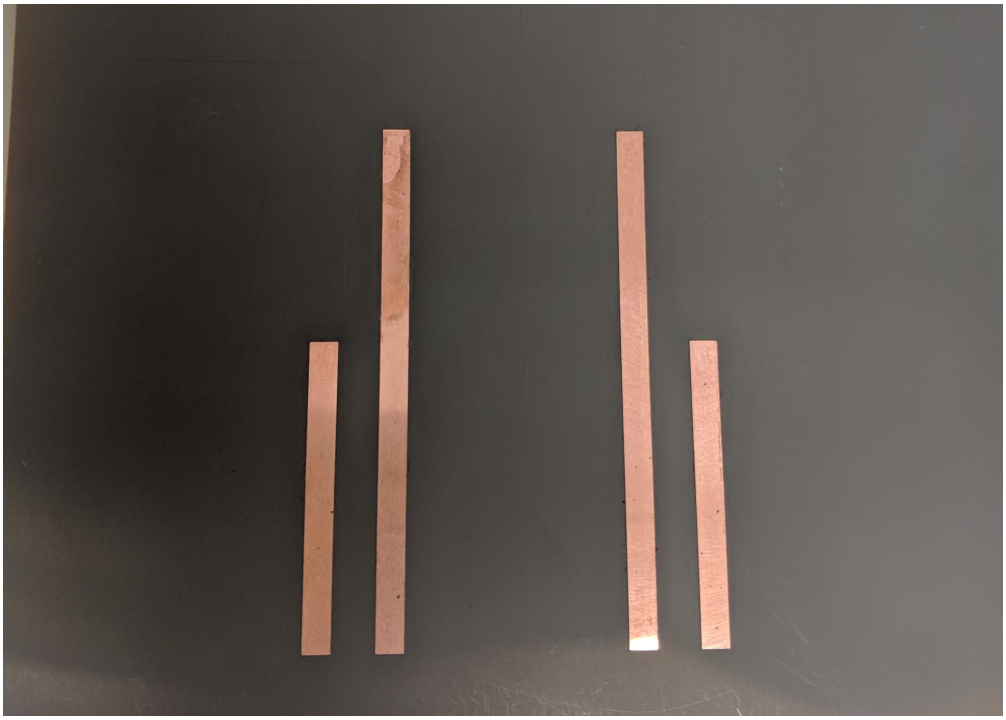

Figure 5.5: Antenna Patterned on Pyralux AP

were weighted at the bottom with washers to approximate the weight of the batteries to emulate the mass and center of gravity of the fabricated eMote sensor boards. The drop test units had a mass of approximately 10 g. The antennas were fabricated on different thicknesses and widths of DuPont Pyralux AP and Rogers Corp Ultralam. A representative sample of different configurations was created; however, the number of configurations was limited due to time and budgetary constraints. A drop unit with an Ultralam rotor can be seen in Figure 5.4. These drop units were then dropped off the roof of a building for a fall of roughly 15 m during a day with mild to no crosswinds. Each board was dropped 3 times and the mean of the average fall speeds are presented in Table 5.2. The average fall speed was calculated by timing the fall of the eMotes and dividing that by the height of 15 m.

In the first round of drop testing, the drop units with thicker rotors were more likely to glide than those with thinner rotors. The gliding performance was less desirable as the units fell faster than the rotating units. These units glided because the edges of the wings did not flex as easily to create the additional drag force that would force the device to rotate. The

Table 5.2: Fall Times of Different Rotor Structures with Three 15 m Drop Tests

Substrate	**Thickness**	**Size**	**Average Fall Speed**
Ultralam	7 mil	B,A	3.7 m/s
Ultralam	7 mil	B,A+	4.1 m/s
Ultralam	7 mil	A,A+	3.8 m/s
Pyralux AP	6 mil	B,A	4.6 m/s
Pyralux AP	6 mil	B,A+	3.8 m/s
Pyralux AP	6 mil	A,A	2.9 m/s
Ultralam	5 mil	B,B	4.4 m/s
Ultralam	5 mil	B,A	4.5 m/s
Ultralam	5 mil	B,A+	4.4 m/s
Ultralam	5 mil	A,A	4.1 m/s
Pyralux AP	4 mil	A,A	4.9 m/s
Pyralux AP	4 mil	B,A+	2.1 m/s
Pyralux AP	4 mil	B,A	2.0 m/s
Pyralux AP	4 mil	A,A+	2.4 m/s

Rogers Ultralam material was significantly stiffer than the Pyralux material so it was simple to remove this material as a contender. From these series of tests, it was determined that the 4 mil thick Pyralux AP had the best falling characteristics. A small batch of 2 mil thick Pyralux AP antennas were made and tested, but it was quickly deemed that the material was too thin and bent too easily, thereby not autorotating.

Several antennas of the 4 mil Pyralux AP were then attached to the fabricated eMote boards, as seen in Figure 1.3. These units underwent additional drop testing to find the optimal mechanical design. In these secondary tests, 2 or 3 units with each rotor structure were dropped several times from a quadcopter at heights between 50 m and 100 m. Units were also dropped 18 times from a height of 16 m in the Auburn University Arena which is an indoor, controlled climate. In this test, 2 or 3 units of each size were dropped. The

Table 5.3: Fall Speeds Averaged over Indoor and Outdoor Drops

Size	Avg Fall Speed (Indoor)	Avg Fall Speed (Outdoor)
A,A	3.1 m/s	2.9 m/s
A,A+	4.1 m/s	2.7 m/s
B,A	2.4 m/s	2.5 m/s
B,A+	2.5 m/s	3.4 m/s

average fall speeds from these tests are presented in Table 5.3. This table illustrates the actual eMote fall speed averaged over many drops at higher altitudes and shows a more accurate average fall speed than drops with the emulated test device. With these data, the B,A configuration was selected as the final design, which has rotor dimensions of 130 mm by 45 mm and 100 mm by 45 mm, as it had the lowest average fall speeds.

5.3 Antenna Design

The system needed to have an antenna to transmit the recorded atmospheric and GPS data back to the receiver station. For the data transmission, the devices utilize the 902-928 MHz ISM band. The antennas were designed to operate over a bandwidth greater than required in order to tolerate minor manufacturing errors and ensure reliable system performance. The system also needed an antenna to receive GPS data. It was designed for the GPS L1 band, which operates between 1565.17 and 1585.63 MHz. Again, the goal was to design an antenna with a larger than required bandwidth to ensure optimal performance and to possibly receive some of the other GNSS signals to increase the number of received satellites.

5.3.1 Simulation

With the substrate dimensions determined through mechanical testing, the antennas were designed and simulated in ANSYS Electronics Desktop. The chosen substrate was DuPont Pyralux AP9141R, which has been proven as an RF capable substrate [87, 88]. The

layout was created in Electronics Desktop and a screenshot with the sizes of the antennas denoted can be seen in Figure 5.3. Since the devices are designed to transmit at a low power, the antenna requires a good impedance match over the 902-928 MHz ISM band along with high efficiency. Similarly, as GPS is a low-power, circularly polarized signal, the antenna needs to be well matched over the 1.563-1.587 GHz GPS L1 band. The designed GPS antenna is linearly polarized, which will add a 3 dB loss associated with the cross-polarization [23].

Figure 5.9 compares the simulated and measured radiation patterns. In the Appendix A.4 the 3D radiation pattern of the ISM band dipole can be seen and in Appendix A.5 and A.6 two angles of the 3D radiation pattern of the GPS dipole antenna can be seen. In the 3D patterns, the perturbation of the GPS antenna radiation pattern due to the coupling of the ISM band antenna can be seen, which was noted in the measured radiation patterns. The radiation pattern closely matches that of the standard dipole for both the ISM and GPS band antennas with the noted GPS perturbations. The simulated antennas are well matched over the bands of interest as seen in Figures 5.6 and 5.7. The bandwidth of these antennas are defined as a VSWR of less than 2. The simulated ISM band dipole has a VSWR below 2 from 870 MHz to 970 MHz for a bandwidth of approximately 100 MHz, while the simulated GPS band antenna has a VSWR below 2 from 1.51 GHz to 1.64 GHz for a bandwidth of approximately 130 MHz.

5.3.2 Measured Results

Approximately 130 antennas were fabricated. To measure the device, the antennas were connected to PCBs comprised of a low loss substrate with SMA connectors attached, seen in Figure 5.10, for connection to the network analyzer. A small set of antennas were fabricated in-house for initial prototyping, but most were fabricated out-of-house. Antennas were attached to the eMote sensor boards which are a 0.8 mm thick FR4 substrate containing a microcontroller, RF transceiver, sensors, and battery. The antennas were attached using high-purity copper brackets to maintain the desired structure while still having good

conductivity. The fully fabricated eMote can be seen in Figure 1.3. To verify that the fabricated devices worked as simulated, 20 antennas were measured. The VSWR was measured using a Keysight FieldFox N9951A, and the radiation pattern was measured with a Diamond Antenna Measurement Systems DAMS7000 with the FieldFox as the measurement device. All measurements were conducted with calibrated equipment in an anechoic chamber to minimize noise.

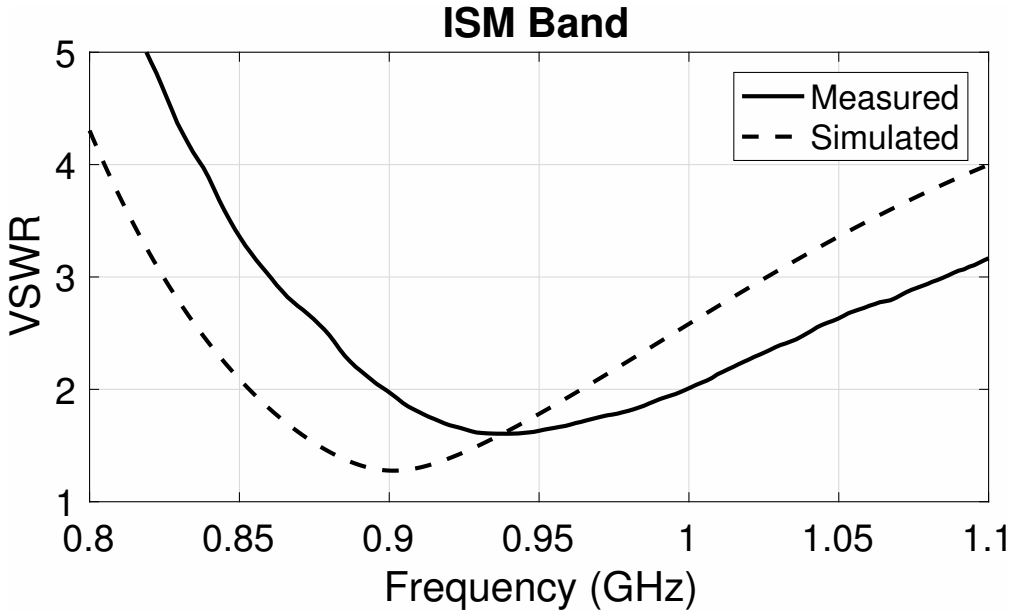

Figure 5.6: Simulated and Average Measured VSWR of the ISM Band Antenna

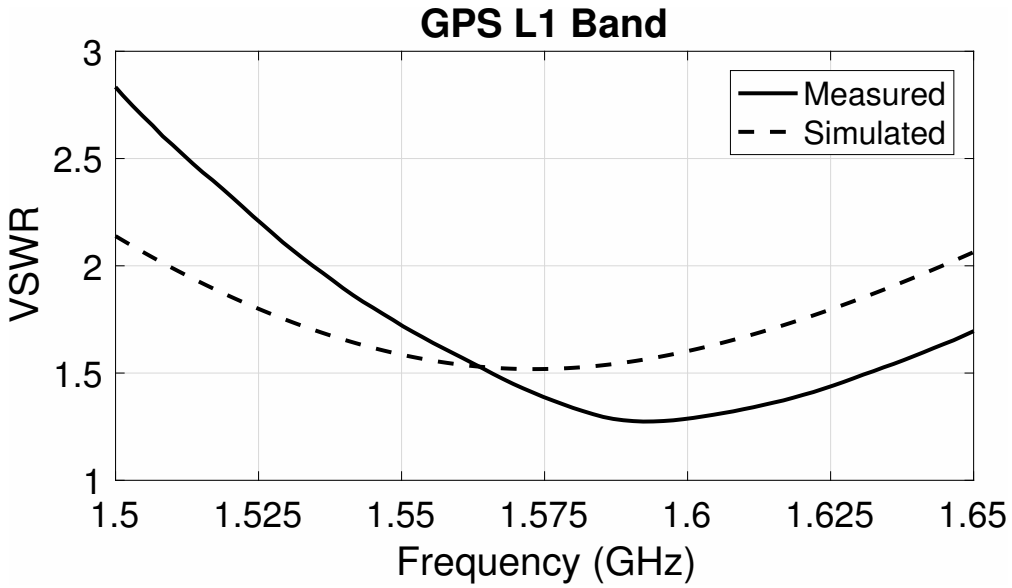

Figure 5.7: Simulated and Average Measured VSWR of the GPS L1 Band Antenna

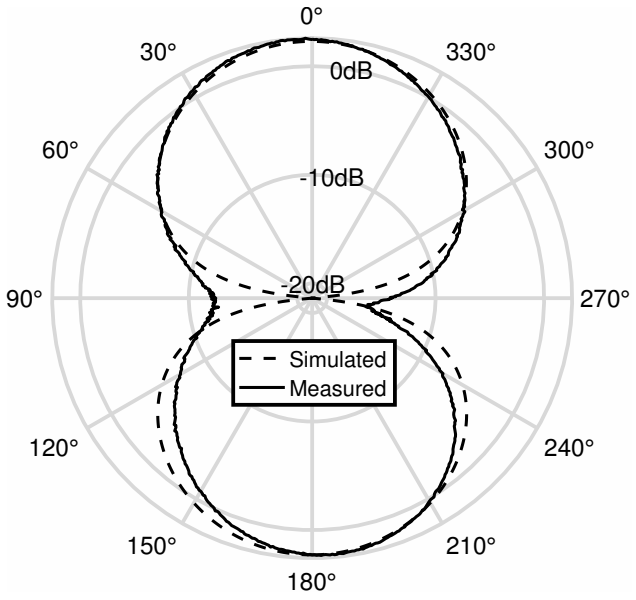

Figure 5.8: Simulated and Measured Gain (Broadside) in dB for ISM Band Dipole

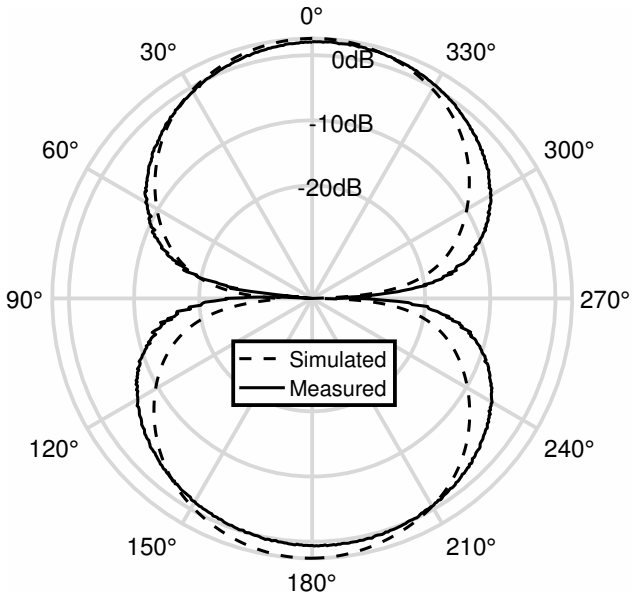

Figure 5.9: Simulated and Measured Gain (Broadside) in dB for GPS Dipole

Table 5.4: Measured Radiation Pattern Characteristics

	Gain 0°	**HPBW 0°**	**Gain 180°**	**HPBW 180°**
ISM	2.6 dBi	72 degrees	2.32 dBi	65 degrees
GPS	2.14 dBi	70 degrees	0.56 dBi	80 degrees

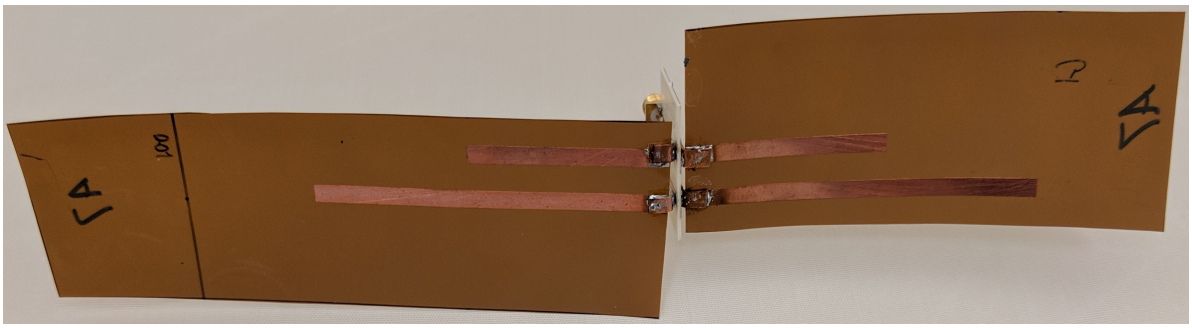

Figure 5.10: Dual Dipole with Feed PCB for Measurement

To measure the antennas, both rotors were soldered to a PCB made of Rogers RT/duriod 5880 laminate with matched transmission lines. The PCBs were fabricated in-house using an LPKF S103 PCB milling system. The measured VSWR, seen in Figures 5.6 and 5.7, for both antennas show deviation from the simulated results. Since the measured VSWR shifted

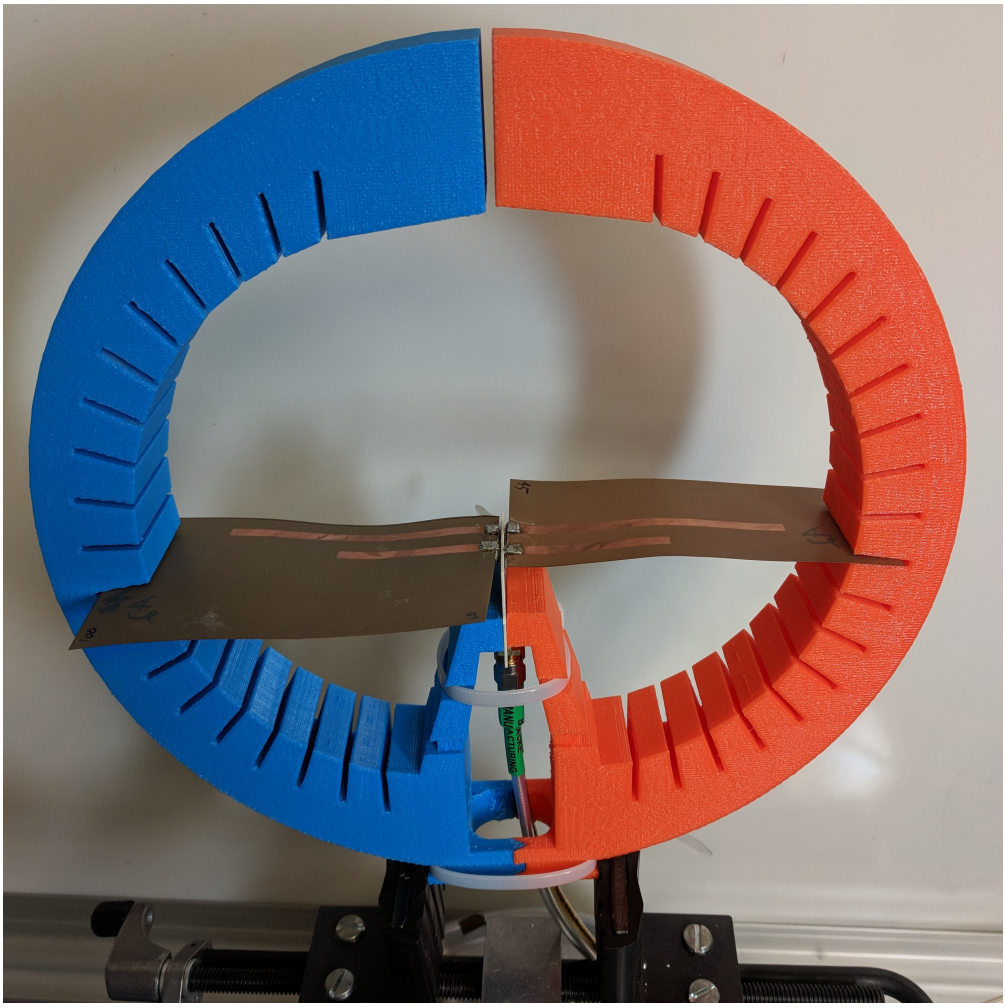

Figure 5.11: Antenna Flex Test System

upward for both devices, it was noted that the antennas which were primarily manufactured out-of-house were depanelized improperly and the copper was shortened by approximately 1 mm on most of the antennas. Even though there was an issue with the manufacturing tolerances, the large bandwidth of the antennas still included the desired operating frequencies. The measured ISM band dipole has a VSWR below 2 between 900 MHz and 1 GHz for a bandwidth of approximately 100 MHz. The measured GPS L1 Band dipole has a VSWR below 2 from 1.56 GHz to 1.7 GHz for a bandwidth of 140 MHz. To verify that the removal of 1 mm of copper would increase the center frequency, a simulation was conducted which did agree with the measured results.

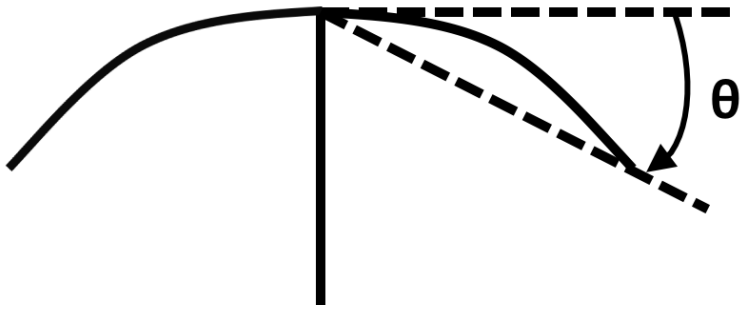

Figure 5.12: Angle Definition for Antenna Bend Testing

To measure the radiation pattern, seen in Figure 5.9, the antenna was set on a rotating platform 2 meters away from a 13 dB yagi-uda antenna. The 0 degree position has the rotors parallel to the ground, as seen in Figure 5.11, with the ISM antenna facing the front and the GPS antenna behind it. It was rotated along the plane parallel to the ground with measurements taken every 0.5 degrees. The gain and half-power beam-width (HPBW) at both maxima are displayed in Table 5.4. The lobe for the GPS antenna at 180 degrees had a much lower gain than the lobe at 0 degrees. The gain at the 180 degree position is reduced due to mild coupling effects with the larger ISM antenna located a few millimeters away. The radiation efficiency of the antennas is greater than 90 percent.

5.3.3 Bend Testing

To verify that the antennas will work during the bending associated with a typical fall, a test fixture was 3D printed with slots at 10 degree angle increments. The fixture, as seen in Figure 5.11, was printed with polylactic acid (PLA) plastic at a very low fill rate to minimize interference. The antennas were bent and measured over a range of +80 degrees to -40 degrees. A representation of how the bend angle was defined can be seen in Figure 5.12. A positive bend angle has the antennas curving upward away from the PCB, which naturally happens when falling, and a negative angle has the antennas bending downward toward the PCB, which may occur when the device encounters turbulence. The range of bend angles measured included the anticipated range with an additional 20 degree margin on either side.

Exact bend angles at specific wind conditions have not been measured, but all bend angles correlate with testing under mild to moderate winds with less than 5% device failure. The goal is to produce the devices at a low cost and deploy at large scale, so a small number of device failures can be tolerated.

The antennas were measured with a Keysight FieldFox network analyzer in an anechoic chamber. The measured VSWR at different bend angles for both the ISM and GPS antennas can be seen in Figures 5.13 and 5.14 respectively. When the antennas were bent, the center frequency increased as the horizontal length from tip to tip of the dipoles was reduced. This orientation of the radiating elements has seen some application in long distance communications [89]. This test validates the current antenna design for our application, as the antennas are anticipated to bend less than the maximum positions measured.

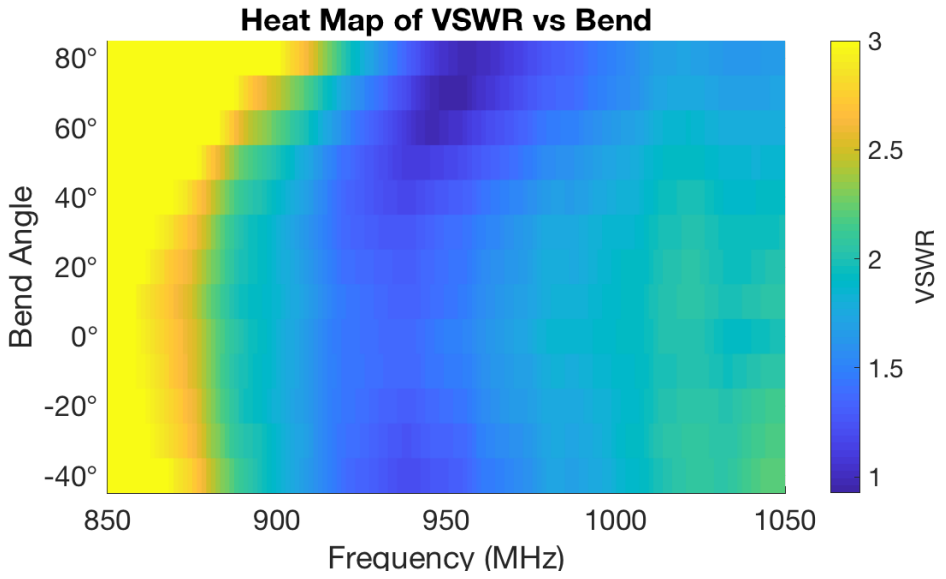

Figure 5.13: Measured VSWR During Bend Testing for ISM Band Dipole

5.4 eMote Polarization

With the current antenna design, one potential issue is the rotation of the eMote. Since dipoles are linearly polarized, when the eMote spins nulls will be pointed towards the receiver during some transmissions. As can be seen in the 3D radiation patterns in the Appendix,

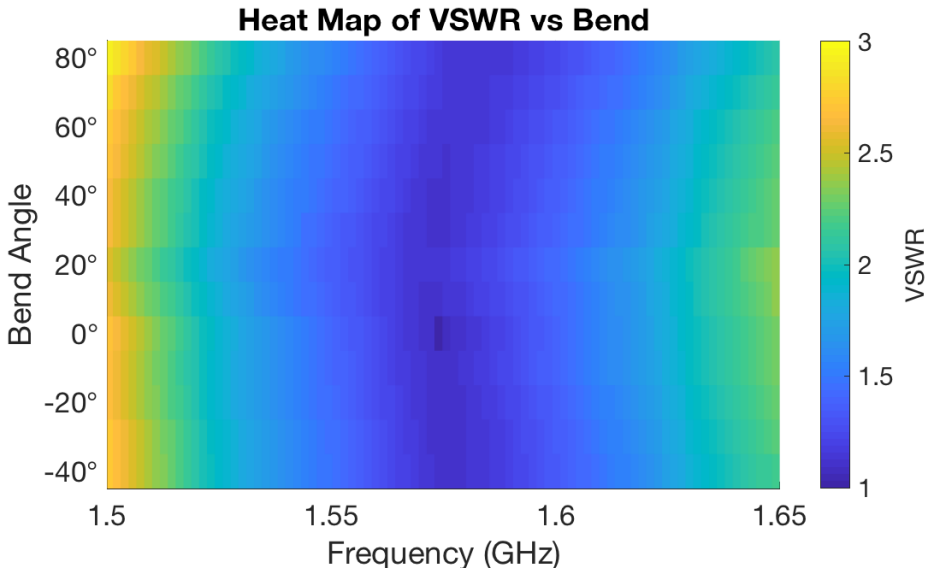

Figure 5.14: Measured VSWR During Bend Testing for GPS L1 Band Dipole

dipoles have a donut-like pattern where the E-field radiates outward broadside from the antenna. As shown in the diagram in Figure 5.15, as the eMote rotates when falling it will not always be broadside to the receive antenna. When the eMote is broadside to the receiver, the packet should be received, but packets will not be received when the eMote antenna is perpendicular to the receive antenna. In order to rectify this issue, the polarization of the antenna must be changed. In the current design, the E-field is horizontally polarized with respect to ground. One solution to this issue is to make the eMote polarized vertically with respect to ground. Unfortunately, this issue cannot be simply resolved by modifying the copper structure on the wings.

5.4.1 Vertically Polarized Antenna

One way to address this problem is to add a wire sticking upward from the eMote and adding a copper layer to the eMote PCB. With this modification, the eMote transmit antenna will be a variation of a dipole with one wide leg and one thin leg. The vertically polarized antenna was simulated in Electronics Desktop with the simulated layout and dimensions seen in Figure 5.16. In the simulation, the wire protruding from the eMote is one-quarter the

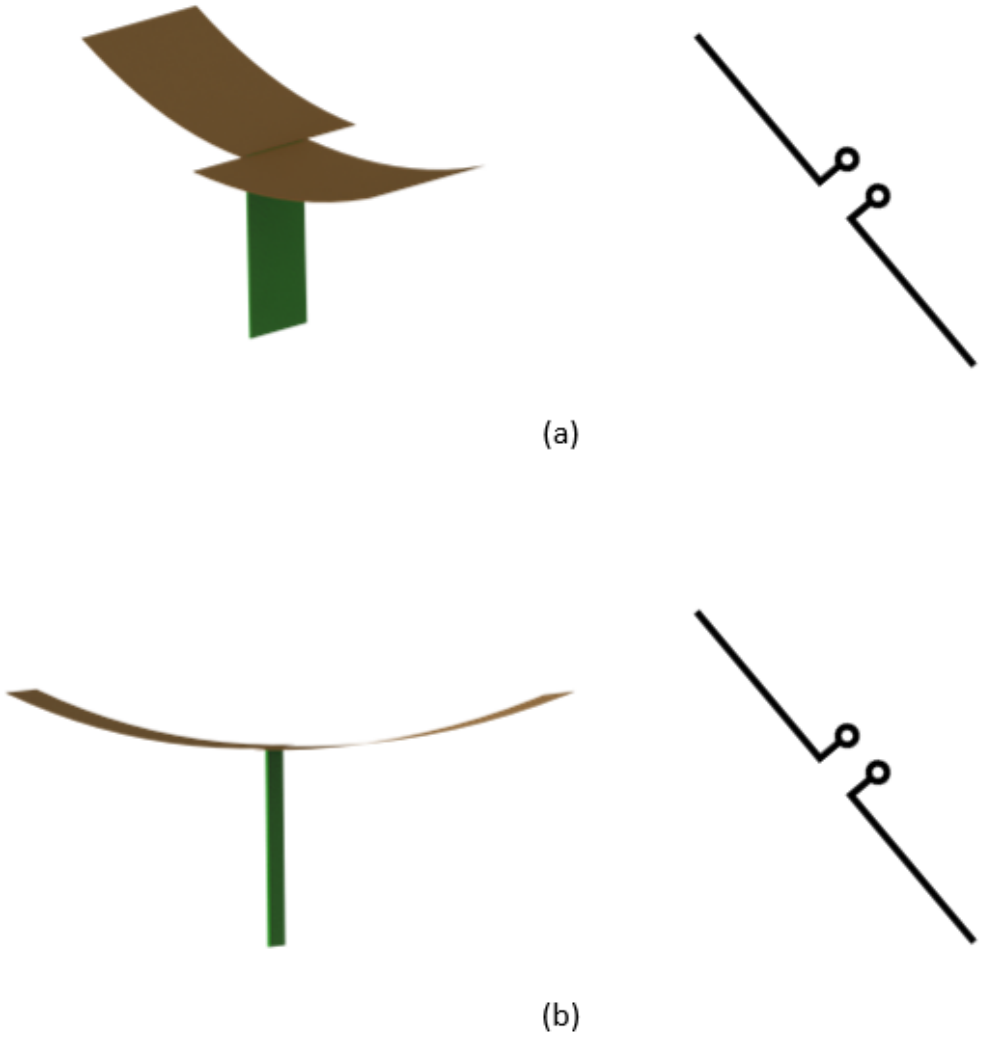

Figure 5.15: Diagram Showing Dipole Alignment. In (a) Receiver and Transmitter are Aligned, in (b) Receiver and Transmitter are not Aligned

wavelength and the lower copper segment was set to the size of the eMote body. The length of the wire was shortened slightly in HFSS to minimize the reactance. It has a simulated radiation pattern that looks like a dipole as seen in Figure 5.19. The 3D antenna pattern can be seen in Appendix A.7. Since one leg of the dipole is the PCB, which is a wider strip of copper than the other leg, the pattern is not uniform. From the simulated VSWR shown in Figure 5.18, it can be seen that it is well matched over the band of interest. The simulated structure had a VSWR of less than 2 for 860 to 960 MHz.

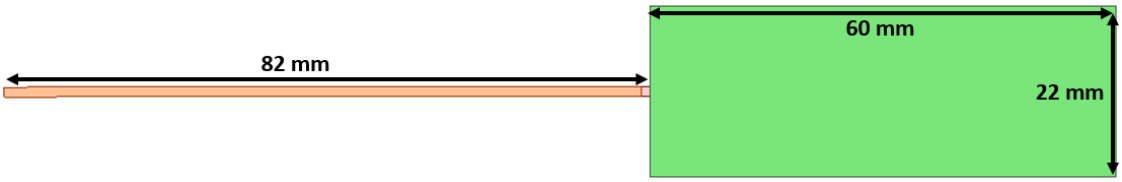

Figure 5.16: Dimensions of Simulated Vertically Polarized Antenna Test Unit

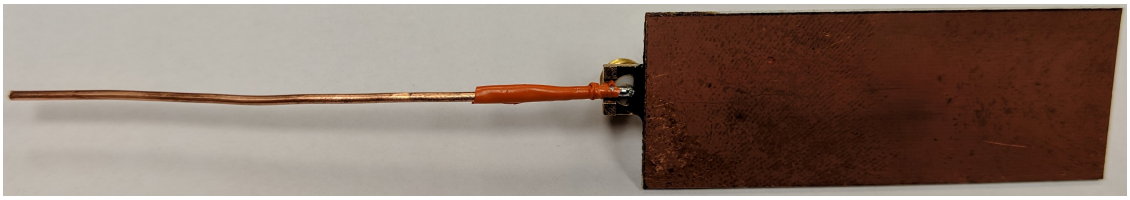

Figure 5.17: Vertically Polarized Antenna Test Unit

It was fabricated by attaching a wire to a section of substrate cut to size with an LPFK s103. The wire was trimmed to minimize the reactance, thereby minimizing the reflection. The wire length after trimming was about 81 mm with a 50 mil diameter. The device was connected for measurement with an SMA connector. Ten devices were fabricated and tested. A fabricated unit can be seen in Figure 5.17. The VSWR can be seen in Figure 5.18, and the bandwidth with a VSWR less than 2 is approximately 850 MHz to 970 MHz. The measured radiation pattern can be seen in Figure 5.19, and is similar to the simulated pattern but with a 2 dB decrease in gain over the PCB side of the dipole. This testing was deemed successful, so a device incorporating the vertically polarized ISM band transmit antenna and horizontally polarized GPS antenna was investigated.

5.4.2 Vertically Polarized Transmit Antenna with GPS Antenna

The new device will need to incorporate the newly created antenna with the existing GPS antenna on a rotor to maintain the required performance for both the GPS reception and autorotation. This device was created and simulated. Images of the simulated device can be seen in Figure 5.20. The simulated 3D radiation patterns can be seen in the Appendix Figures A.8 and A.9. This simulated device contains the same size and thickness of rotors as original eMote to maintain the same mechanical performance. Since the rotors on the

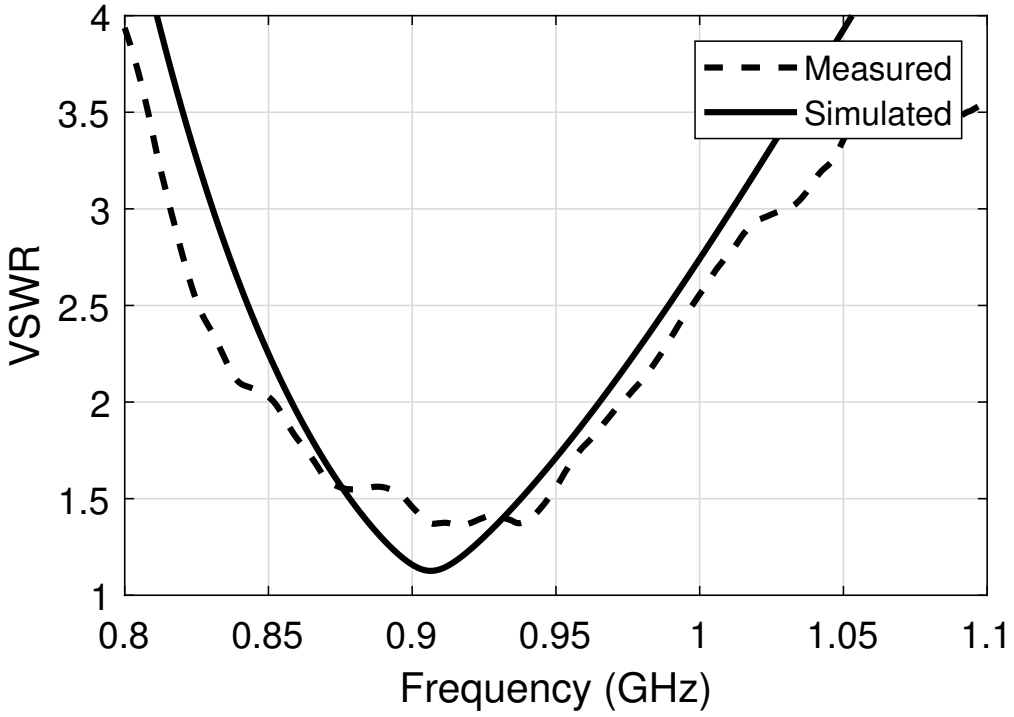

Figure 5.18: Measured and Simulated Vertical Dipole VSWR

eMote are attached with the antenna pads, a bracket will have to be designed and attached to maintain the wing orientation when falling.

The simulated system performs well over the frequency bands of interest. The VSWR for the modified ISM band antenna can be seen in Figure 5.21. From the VSWR, it can be seen that the bandwidth is approximately 860 MHz - 1 GHz. The VSWR for the GPS antenna is seen in Figure 5.22 and the bandwidth is approximately 1.49 - 1.65 GHz. The radiation pattern for the ISM band and GPS antennas can be seen in Figures 5.23 and 5.24 respectively. The max gain of the GPS antenna is approximately 2 dB larger than that of the ISM band antenna.

5.4.3 Implementation of the Revised Antenna Structure

Unfortunately this antenna system was not implemented into a new version of the eMote design as the funding and time did not permit this revision. The device would be relatively

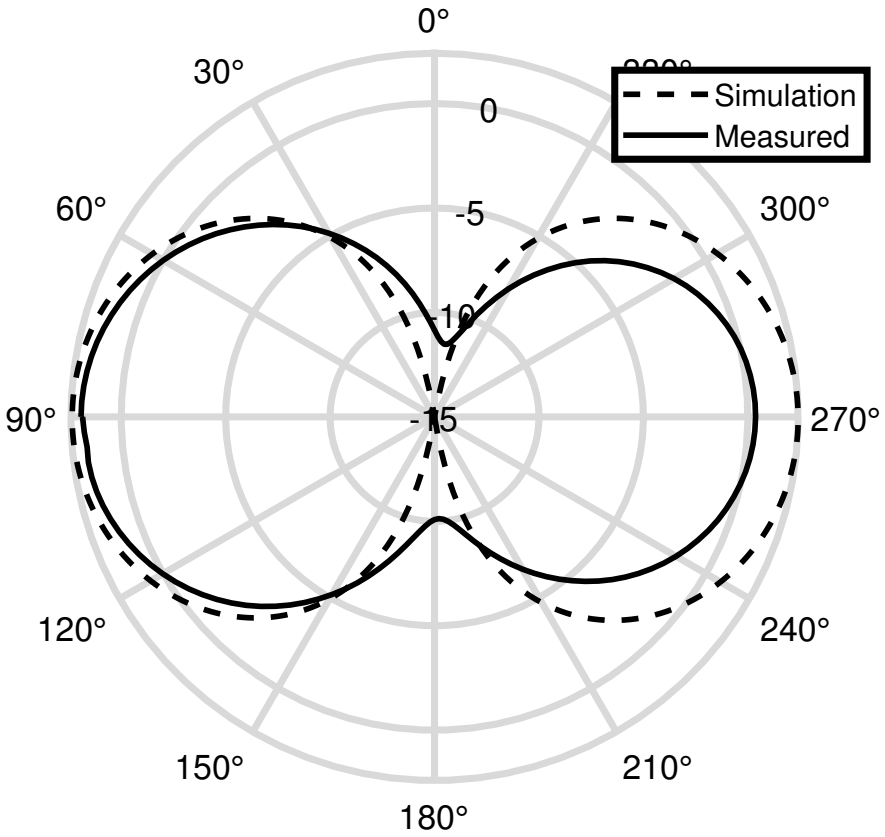

Figure 5.19: Measured and Simulated Vertical Dipole Pattern

simple to implement into a future design if funding was available by increasing the layer count of the eMote PCB and adding a dedicated copper layer to the PCB.

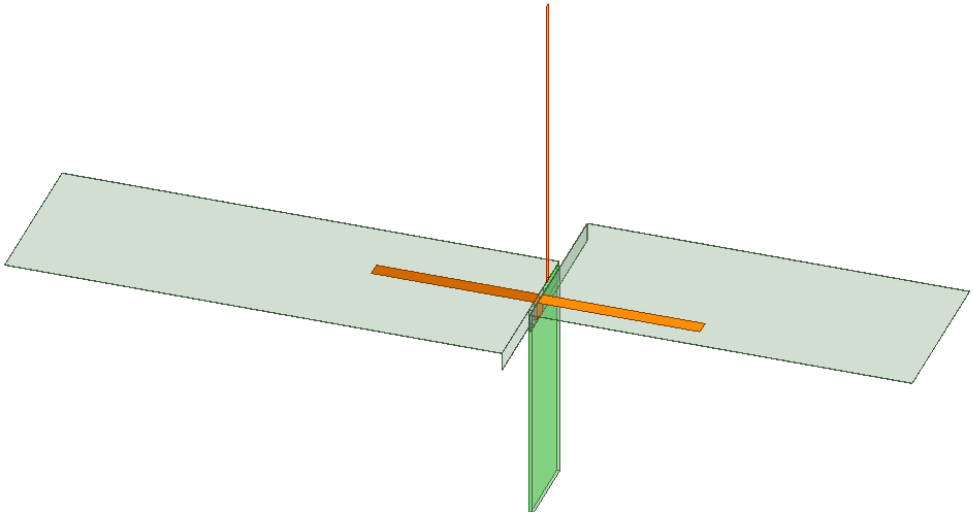

(a)

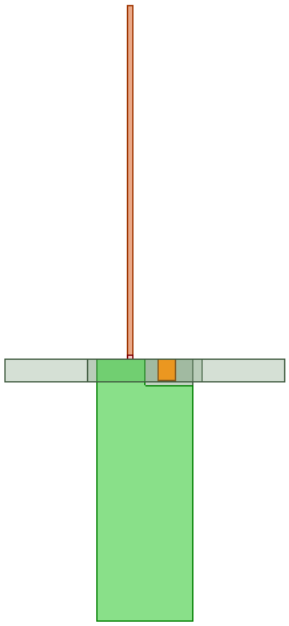

(b)

Figure 5.20: Two Views of the Simulated eMote System with the Vertically Polarized Dipole

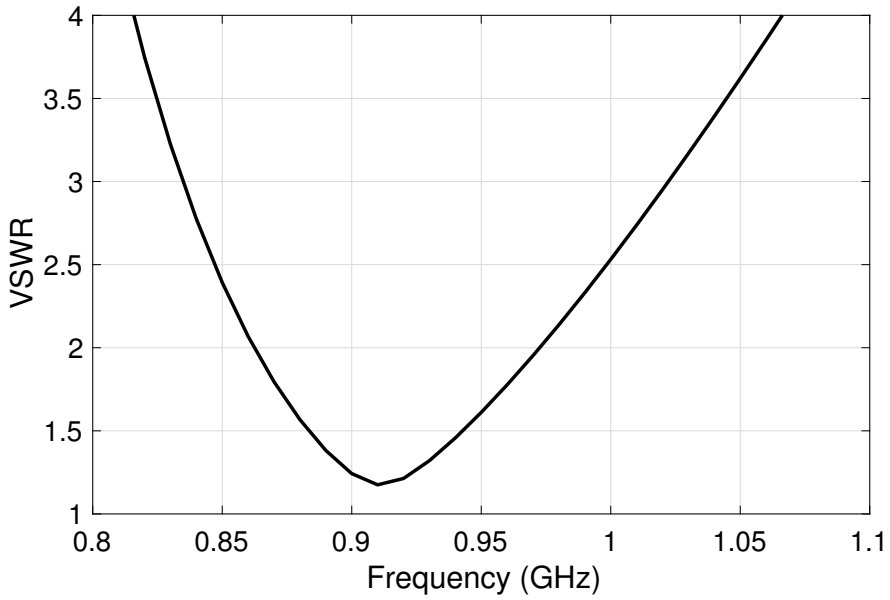

Figure 5.21: Simulated Vertical Dipole VSWR of Revised eMote

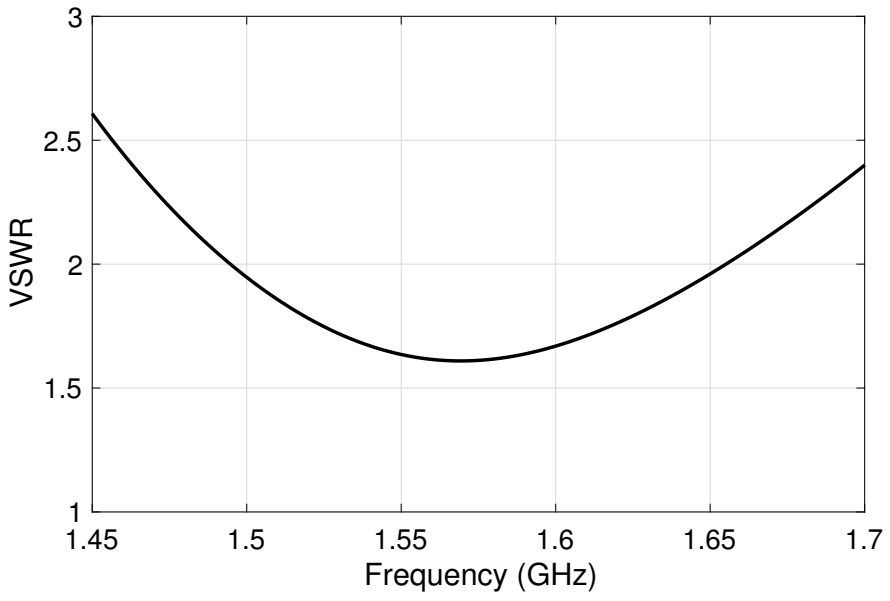

Figure 5.22: Simulated GNSS Dipole VSWR of Revised eMote

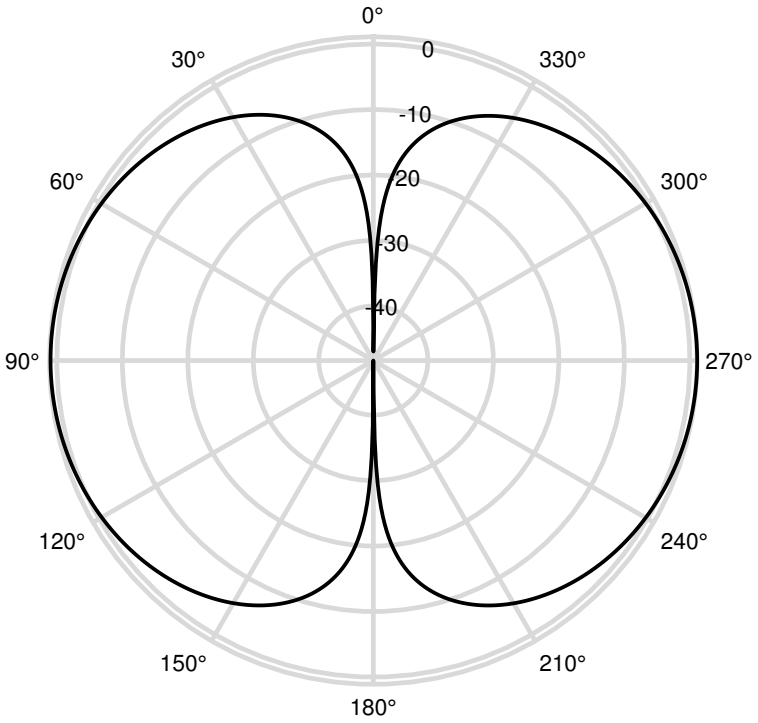

Figure 5.23: Simulated Vertical Dipole Antenna Pattern of Revised eMote

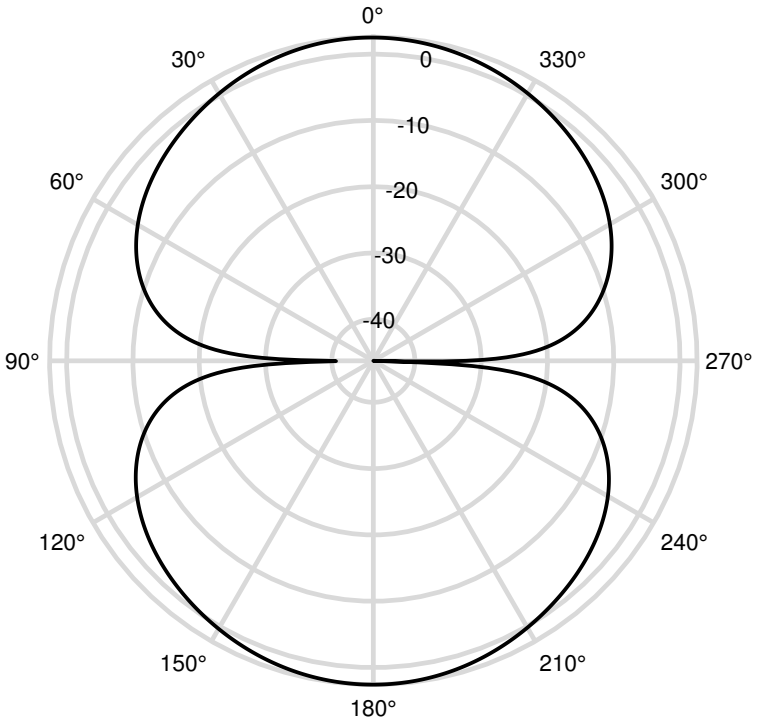

Figure 5.24: Simulated GNSS Dipole Antenna Pattern of Revised eMote

Chapter 6

eMote System Level Testing

6.1 Range Testing

In order to validate that the eMote would perform at a reasonable distance in the field, range testing was conducted. The range testing was conducted in the laboratory and in the field. Laboratory testing was conducted in an anechoic chamber with in-line attenuators to emulate range. Field testing was conducted by launching the eMotes on mylar balloons.

6.1.1 Anechoic Chamber Testing

To first validate the range of the system, the anechoic chamber was used. The word anechoic is derived from an-echoic or literally "without echo" [90]. These chambers were originally designed to remove audible noise and prevent the reflection of audible noise. This concept was transitioned to work at RF frequencies allowing the antenna system to be characterized in an environment that emulates free space as there is little reflection from the wave fronts hitting the wall. These rooms are often referred to as antenna ranges by RF and antenna engineers. The chamber at Auburn University employs pyramidal radiation absorbent material (RAM) to minimize reflections and reduce the RF noise. In Figure 6.1 an image of the anechoic chamber in Broun Hall is presented showing an L band horn pointing at a device under test.

In order to calculate the effective range of the system, the gain of the antenna must be calculated. In order to calculate the gain of the antenna, the loss due to free space transmission must be accounted for. Conveniently, the Friis transmission equation can be utilized to account for the path loss. The transmission equation relies upon the power of the transmitter, power of the receiver, gain of the transmit antenna, gain of the receive antenna,

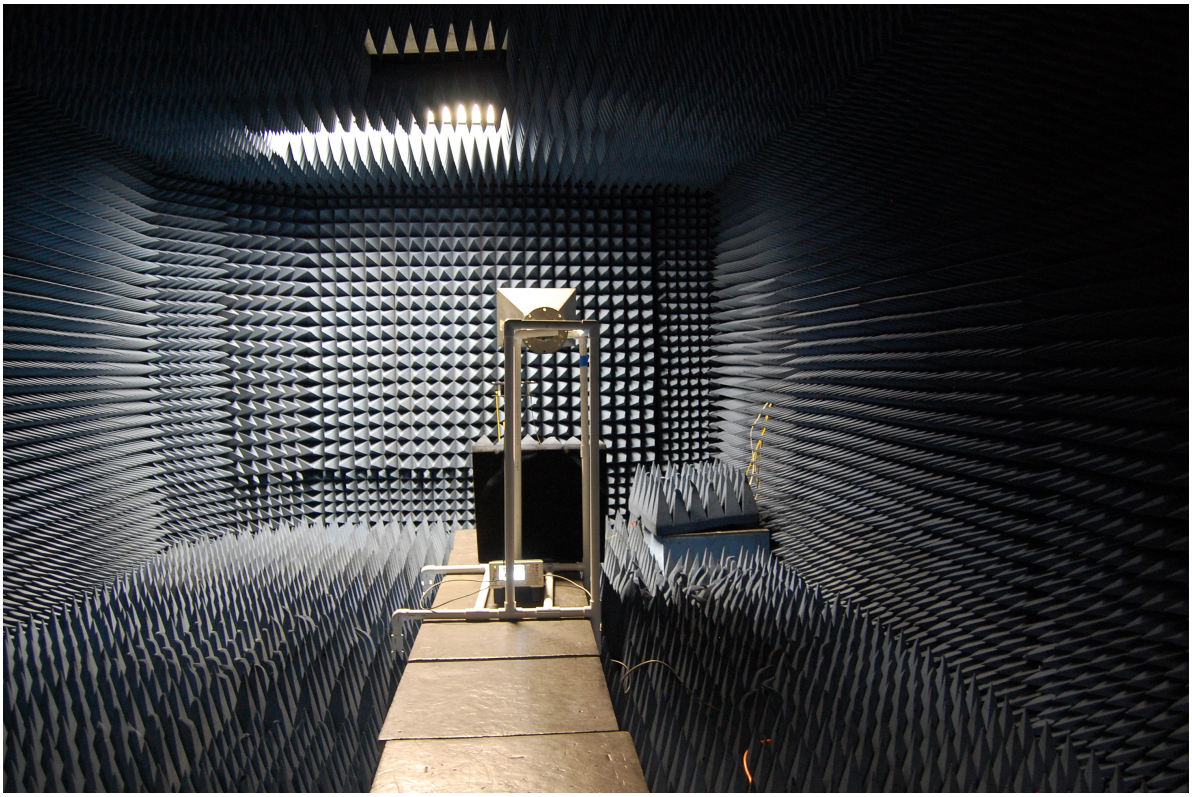

Figure 6.1: Anechoic Chamber with L-Band Horn

and the effective aperture of the antenna. The transmission equation assumes antennas are correctly polarized and pointed. It also does not incorporate noise or multipath effects.

Theorem 6.1 *Friis Transmission Equation*

$$P_r = P_t \frac{G_t G_r \lambda^2}{(4\pi R)^2}$$

Where P_r is the received power, P_t is the transmitted power, G_t is the transmit antenna gain, and G_r is the receive antenna gain. The equation can be rearranged to put it in a convenient logarithmic form.

Theorem 6.2 *Transmission Equation in dB Form*

$$P_r(dBm) = P_t(dBm) + G_t(dBm) + G_r(dBm) - 20log(R(km)) - 20log(f(MHz)) - 32.44$$

From the logarithmic form, it is trivial to rearrange the equation to solve for the gain of the transmit antenna.

Theorem 6.3 *Gain of transmit antenna*

$$G_t(dBm) = P_r(dBm) - P_t(dBm) - G_r(dBm) + 20log(R(km)) + 20log(f(MHz)) + 32.44$$

The free space path loss are the last three terms of theorem 6.2.

Theorem 6.4 *Free Space Path Loss*

$$L_{fs} = 20log(R(km)) + 20log(MHz) + 32.44$$

In the anechoic chamber, to test both the gain of the ISM band and GPS antennas, the eMote antennas were connected to a SMA breakout board and set up on a rotating platform approximately 1.525 m from the reference antenna. For the GPS antenna, the reference was a 20 dB rectangular horn, and for the ISM band antenna the reference was a 14 dB yagi-uda antenna. From the theorem 6.4, the free space path loss at 915 MHz at the range of 1.525 meters is 35.484 dB. To calculate the gain of the design ISM band transmit antenna, theorem 6.3 is used and compared with the gain of a reference antenna. The addition of a well defined reference antenna allows for the calibration of the eMote gain as the received power of the reference antenna can be directly compared to the eMote antenna. In Figure 6.2 the antenna pattern of the dipole and an 8.5 dB yagi-uda antenna can be compared. The yagi-uda antenna has a much larger gain in one direction, which inherently makes it less isotropic.

Then, utilizing the anechoic chamber, the sensitivity of the receiver system was estimated. This was completed by connecting a development board for the eMote transmitter which had a coaxial output connected directly to the receiver through low-loss RF coaxial cabling. The transmitter was placed inside the anechoic chamber and the receiver was placed

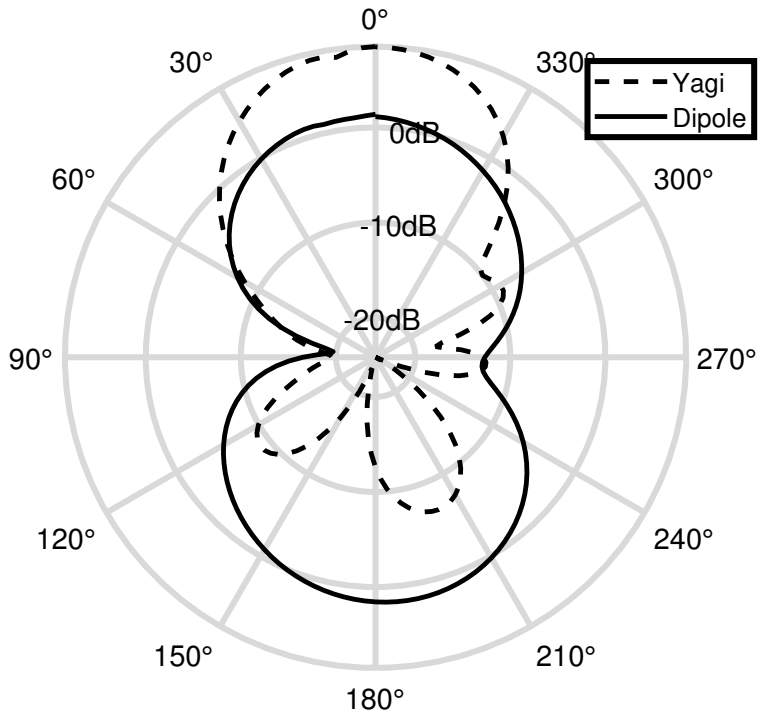

Figure 6.2: Comparison of Measured Yagi Gain to Dipole Gain

outside the chamber to mitigate coupling effects. Range was then emulated by placing attenuators in-line with the coaxial cable. From this test, the sensitivity of the receiver was calculated to be -111 dBm with the selected baud rate, modulation scheme, and forward error correction. With the receiver sensitivity known, the link budget could be calculated. In Table 6.1 the link budget for the eMote ISM band transmitter and the GPS receiver is estimated with the designed antennas and receivers.

Ranges of up to 50 km were originally deemed theoretically possible with a receive antenna gain of 14 dBi and perfect alignment as verified in the chamber. In a system level implementation with a higher gain dish antenna, 100 km ranges are anticipated with a link margin of approximately 10 dB. The range could be increased by adding a power amplifier to the eMote; however, the battery lifetime would be reduced.

Table 6.1: eMote Link Margin

	eMote to Base Station	*GPS to eMote*
Path Loss (50 km TX)	-126 dB	-182 dB
Rain Fade	-2 dB	-2 dB
TX Power	+10 dBm	+44 dBm
TX Antenna Gain	+2 dBi	+13 dBi
RX Antenna Gain	+14 dBi	+2 dBi
Polarization Mismatch	0 dB	-3 dB
Cable Insertion Loss	-1 dB	0 dB
Signal Strength at Receiver	-103 dBm	-122 dBm
Receiver Sensitivity	-111 dBm	-167 dBm
Link Margin	7 dB	39 dB

6.1.2 Balloon Release Range Testing

In order to test the actual system range, several tests were conducted. Since it is not possible to find a direct line of sight on the order of several kilometers, the range was tested by releasing balloons with eMotes attached to them and tracking the received signal. This test was conducted three times on the campus of Auburn University. For each test, mylar balloons were attached to an eMote and they were tracked with yagi-uda antennas from the roof of the electrical engineering building, Broun Hall.

For the first test at Auburn University, two eMotes were tethered to a balloon and launched from the roof of a building. The receivers were located on the roof and the balloon was tracked with two receiver units. The last received packet showed the balloon at an altitude of nearly 4 km and GPS data indicated that the unit was approximately 15 km away laterally for a total range of nearly 15.5 km. Prior to the test, the effect of the temperature on the battery at high altitude was not considered. The last packet received showed a temperature near 0° C and a critically low battery voltage; therefore, the transmitter failed. This system was later recovered when it was found approximately 200 km away.

A second balloon launch tethered a single eMote to the balloon. For this test a battery with a larger capacity and more temperature resilience was used. The balloon traveled 18.9 km from the start location before the balloon failed, as indicated by received altitude data reporting a rapid descent of the system. This system was not recovered because the fall data implied it landed in a densely wooded area. An image of this test with the position and altitude over a map can be seen in Figure 6.3

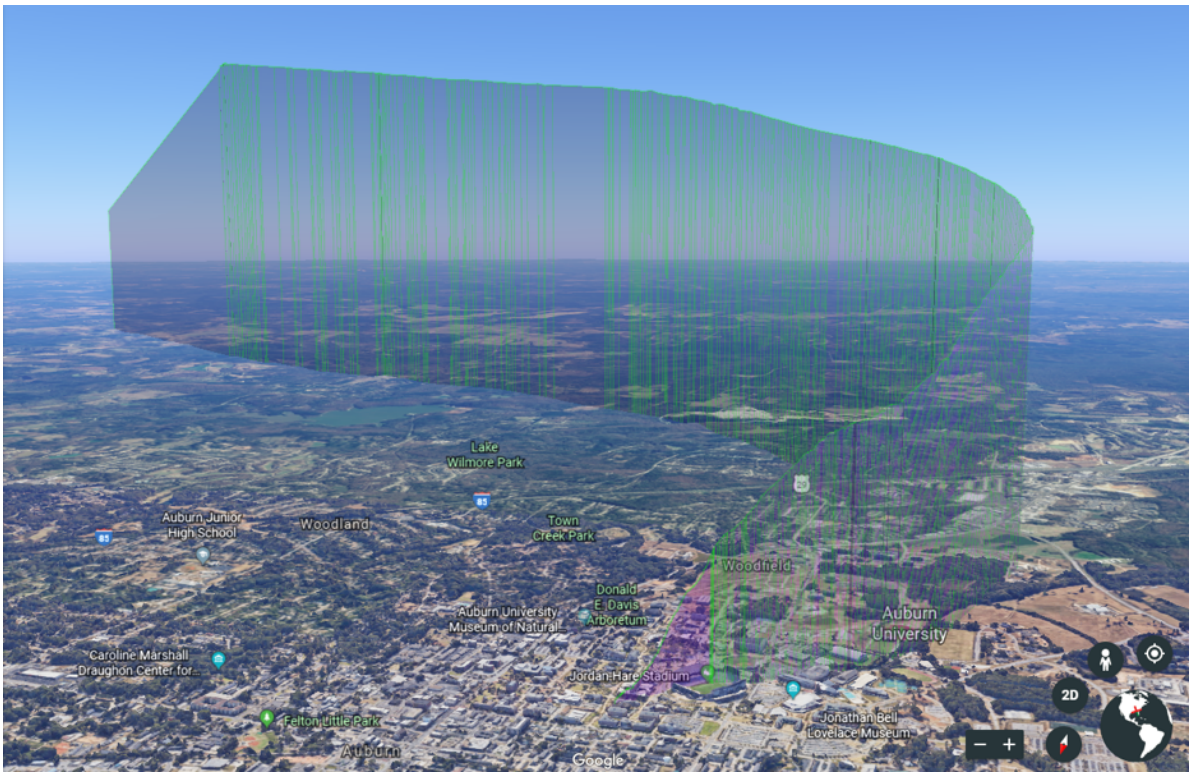

Figure 6.3: Range Test Flight with Altitudes Shown

A third and final balloon launch was attempted at Auburn University. For this test, emphasis was given to provide enough redundancies to hopefully mitigate the issues with previous failures. For this test, two balloon systems were created. Each system had two mylar balloons tethered to one eMote. Each eMote transmitted on a different channel and transmitted one packet per second. The eMotes had two industrial grade AAA batteries which are higher capacity batteries than utilized for typical operation, the 1/3N cell lithium ion batteries. Two receivers for each channel where utilized with yagi-uda antennas that

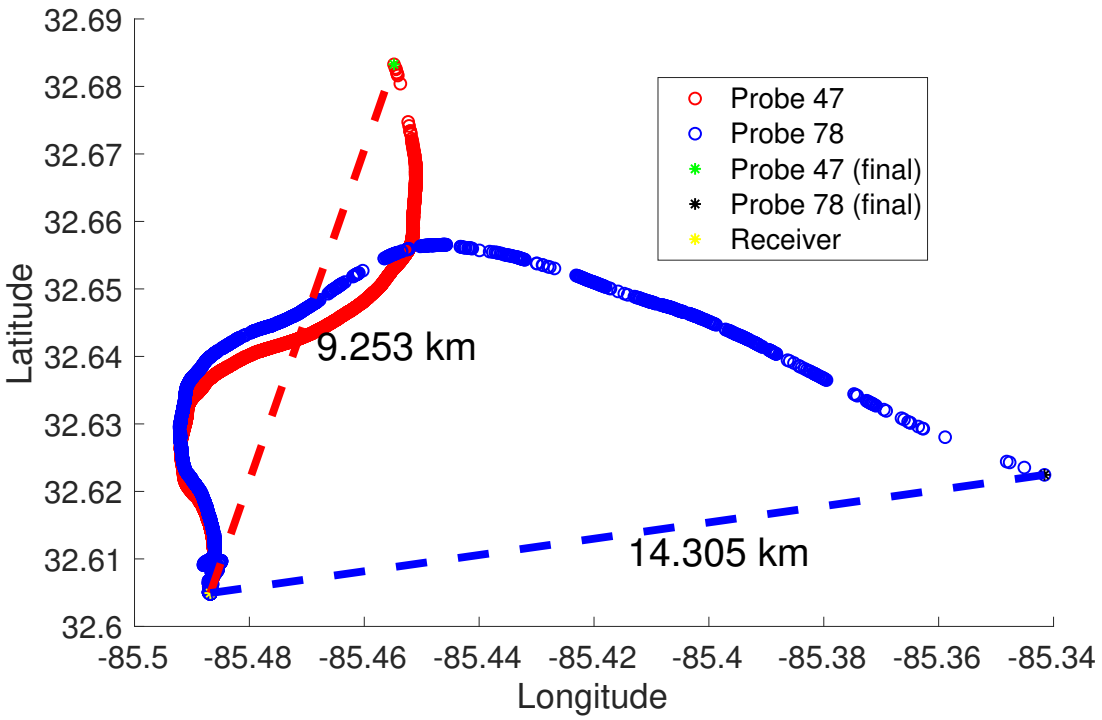

Figure 6.4: Range Test Flight Path with Max Range Denoted

tracked the eMotes. In this test, the balloons were released around 6:30pm local time, or 0030 UTC. The two eMotes tested were numbers 47 and 78. Probe 48 flew to an elevation of approximately 2.5 km before it began a rapid descent, denoting probable balloon failure. The eMote was tracked for approximately 9 km before packets were no longer received. eMote 78 had a more successful test, rising to an altitude of approximately 4.3 km before it became neutrally buoyant. The paths of the eMotes closely correlated until eMote 78 rose above 3 km and entered fast high altitude northwesterly winds (winds blowing from the north west towards the south east). After about 14 km the packets became intermittent and the final packet was received at a range of approximately 14.3 km. See Figure 6.4 for the flight path and calculated range of the tethered eMotes.

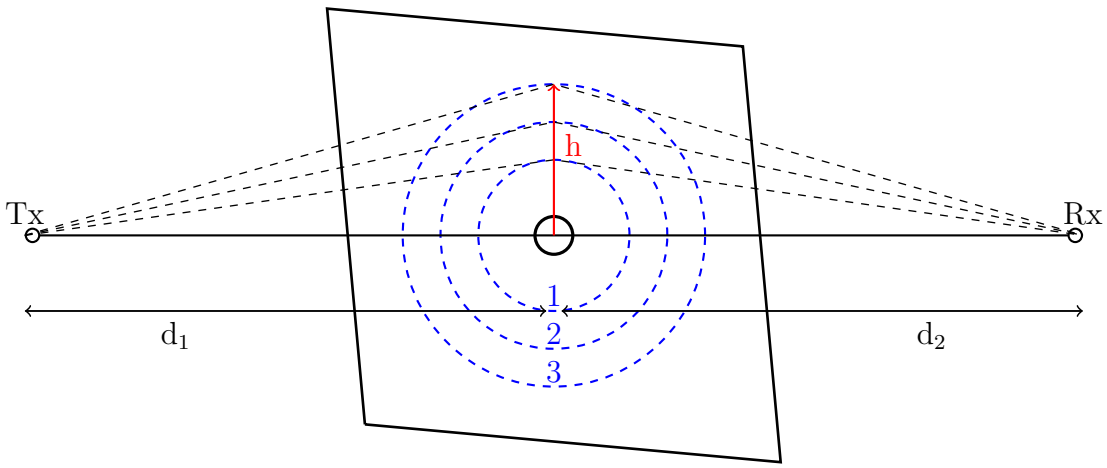

Figure 6.5: Concentric Circles in a Plane which Define Boundaries of Successive Fresnel Zones

6.1.3 Range Limitations

With these data from the balloon testing, it was noted that the range of the eMotes was less than estimated. This led to an investigation as to the reason why. The first step was to validate that line of sight could be achieved and that no issues with blocked signals or multipath caused the failure. Blocked signals were not anticipated as a significant issue as the eMote transmitter was several km high in the tests. In order to remove multipath as a concern, Fresnel zones were considered. Fresnel zones represent successive regions where secondary waves have a path length from the transmitter that are $n\lambda/2$ greater than the total path length of a direct line-of-sight path length [91]. With that definition, concentric circles known as Fresnel zones can be made which predict the interference from multipath effects as demonstrated in Figure 6.5. Since during the range test the receiver was located about 15 m above the ground, and the transmitter was located over 4 km above the ground in the last test, neither multipath nor the Earth's curvature should not have been a significant contribution to the reduced range of the system. A rule of thumb in line-of-sight microwave transmission links is as long as 55% of the first Fresnel zone is kept clear, then further Fresnel zone clearance does not significantly alter diffraction (multipath) loss [91].

The maximum range being less than anticipated range is estimated to be caused by two primary issues. The first issue is that all of the testing was conducted in areas with a large presence of RF noise. Auburn University has a significant amount of ISM band transmitters located across campus for the transmission of various data. Additionally, several labs are conducting research on advanced communication schemes, which involve sporadic ISM band transmissions. Another issue, which is believed to be the primary issue, is that a large loss was not included in the link budget. The primary factor for the decrease in range is attributed to the noise environment at the test location. The receiver sensitivity was calculated in the anechoic chamber which has a very low noise floor or ambient RF noise. As the testing was conducted outside on Auburn's campus, the noise floor is much higher, decreasing the receiver's sensitivity and therefore overall system range. This issue would be less of an issue when the eMotes are utilized in a lower noise floor environment.

In order to account for these issues, the power of the eMote transmitter could be increased. The eMote transmits at a power of +10 dBm. Radiosondes and dropsondes transmit at significantly higher power (50 - 100 dBm) to achieve larger range. A power amplifier could be added to the eMote if a larger capacity battery was implemented. If the transmit power was increased to 50 dBm a range of 100 km could be achieved with a link margin exceeding 10 dB.

6.2 Sensor Validation

To validate the eMote operation, several tests were conducted on Auburn University's campus. The accuracy of the GPS position, the accuracy of the reported altitude, and the accuracy of the sensors were validated. Additionally the time-division multiple access (TDMA) transmission scheme was validated to prove it could be scaled as designed.

6.2.1 GPS Testing

The first system validated was the GPS system accuracy. This was conducted with both static and dynamic tests. For the dynamic testing, the eMote was placed in a golf cart and driven around campus while transmitting to a receiver. The GPS for the eMote is configured to update its position every second and the eMote would transmit its position every second. The receiver saved the data, which was post processed in Matlab and can be seen in Figure 6.6. From this image it can be seen that the GPS tracked the eMote very accurately except in the presence of a large object, Jordan-Hare Stadium, which is a large college football stadium. This is to be expected as GPS experiences issues due to multipath in the presence of large objects [92, 93]. This is not anticipated to be an issue during standard eMote operation, which would not be in an urban environment.

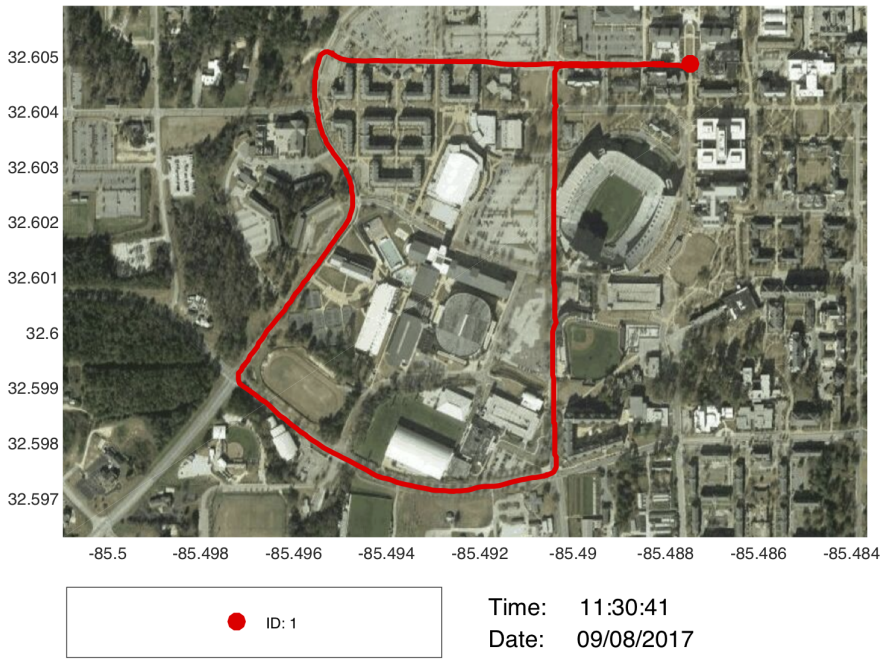

Figure 6.6: Map of GPS Reported Position

6.2.2 Altitude Testing

One issue noticed early in the development of the eMote was that GPS-reported altitude showed significant error. Global positioning systems work by calculating the distance from the receiver to known location of the satellite transmitter. While satellites are constantly orbiting the earth, the GPS receiver system can only receive the data sent from above and the sides. This system allows for excellent accuracy with respect to latitude and longitude if there are multiple satellites in view of the receiver. Unfortunately, when deriving altitude data, all of the satellites are above the receiver as they do not transmit through the earth, which leads to the error adding [94, 95]. In order to examine this error, a test was conducted by flying an eMote up on a quadcopter, hovering, then landing. The GPS data is compared to the pressure sensor on the eMote which can be used as an altimeter. These data shown in Figure 6.7 show that, as expected, the GPS does not provide accurate altitude data therefore it should be calculated from the pressure sensor.

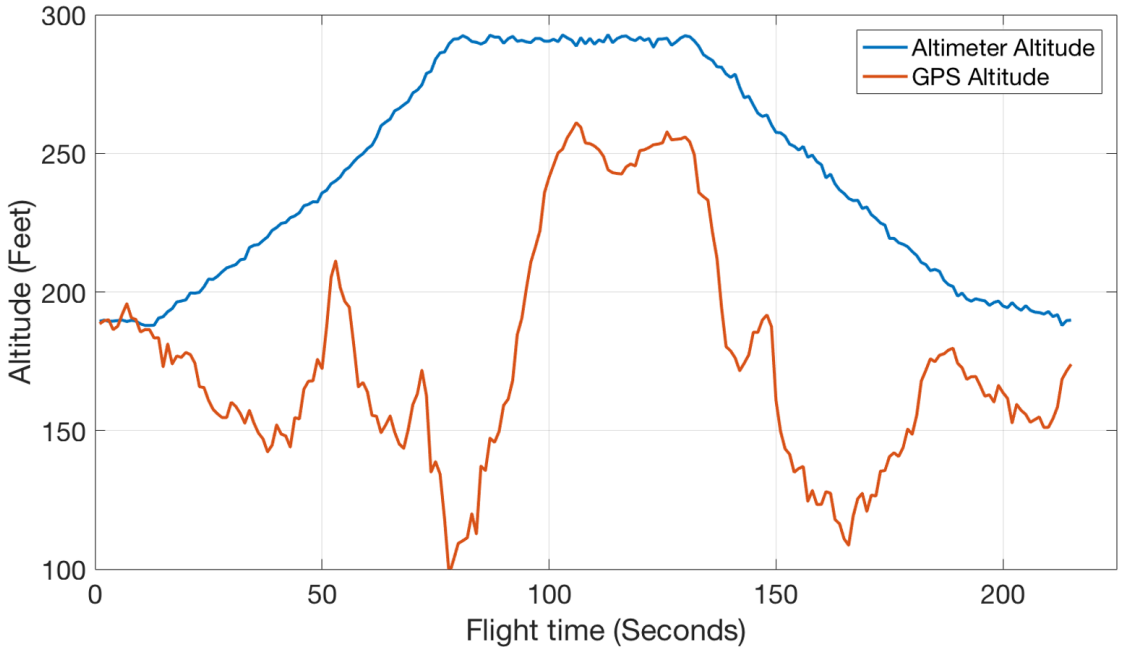

Figure 6.7: Analysis of GPS Reported Altitude

Table 6.2: Manufacturer Stated Accuracies vs. WMO and NOAA Accuracy Requirements

Measurement	**Sensor**	**MSA**	**Standards**	
			WMO	**NOAA**
Temperature	SHT25 MS5803	±0.72 °F ±1.44 °F	±3.6 °F	±1 °F
Air Pressure	MS5803	±1.5 mbar	±1 mbar	±0.7 mbar
Relative Humidity	SHT25	±1.8 %	±5 %	±1.5 %
Wind Speed (indirect)	Max M8	±0.5 m/s	±1 m/s	±0.51 m/s
GPS Coordinates	Max M8	±2 m	N/A	N/A
GPS Time Stamp	Max M8	±50 ns	N/A	N/A

6.2.3 Sensor Accuracy

To validate the sensors, testing was completed in calibrated chambers at Auburn University. In the preliminary chamber testing, it was noticed that there was hysteresis in the temperature sensor data. This was caused by the thermal mass of the PCB slowing the rate of change of the sensors. This was corrected in the final design when the protrusion with several cut-outs for thermal isolation was added to the PCB. This protrusion contains the SHT25 sensor which senses both temperature and relative humidity. The sensor accuracies are reported in Table 6.2 [96, 97]. The sensors accuracies are well within the World Meteorological Organization (WMO) and National Oceanic and Atmospheric Administration (NOAA) standards.

In-situ testing was also completed by setting the sensors out on Auburn University's campus. During this testing, it was noticed that the eMotes experience thermal offsets due to solar irradiated heating. This is deemed not to be a major issue during device implementation as the sensors will be spinning in the air. The wind from the spinning eMote should aspirate the system. A final sensor test was conducted overnight on the campus of Auburn University on April 16th - 17th, 2019. In this test, seven sensors were placed around the northern quadrant of the university, and the sensor data was recorded by a base station located on the roof of Broun Hall, the electrical and computer engineering building. The

sensors collected data from approximately 9 am on the 16th until approximately 4 pm on the 17th, all times in CDT (central daylight time). The collected data can be seen in Figure 6.8, and the eMote positions can be seen in Figure 6.9.

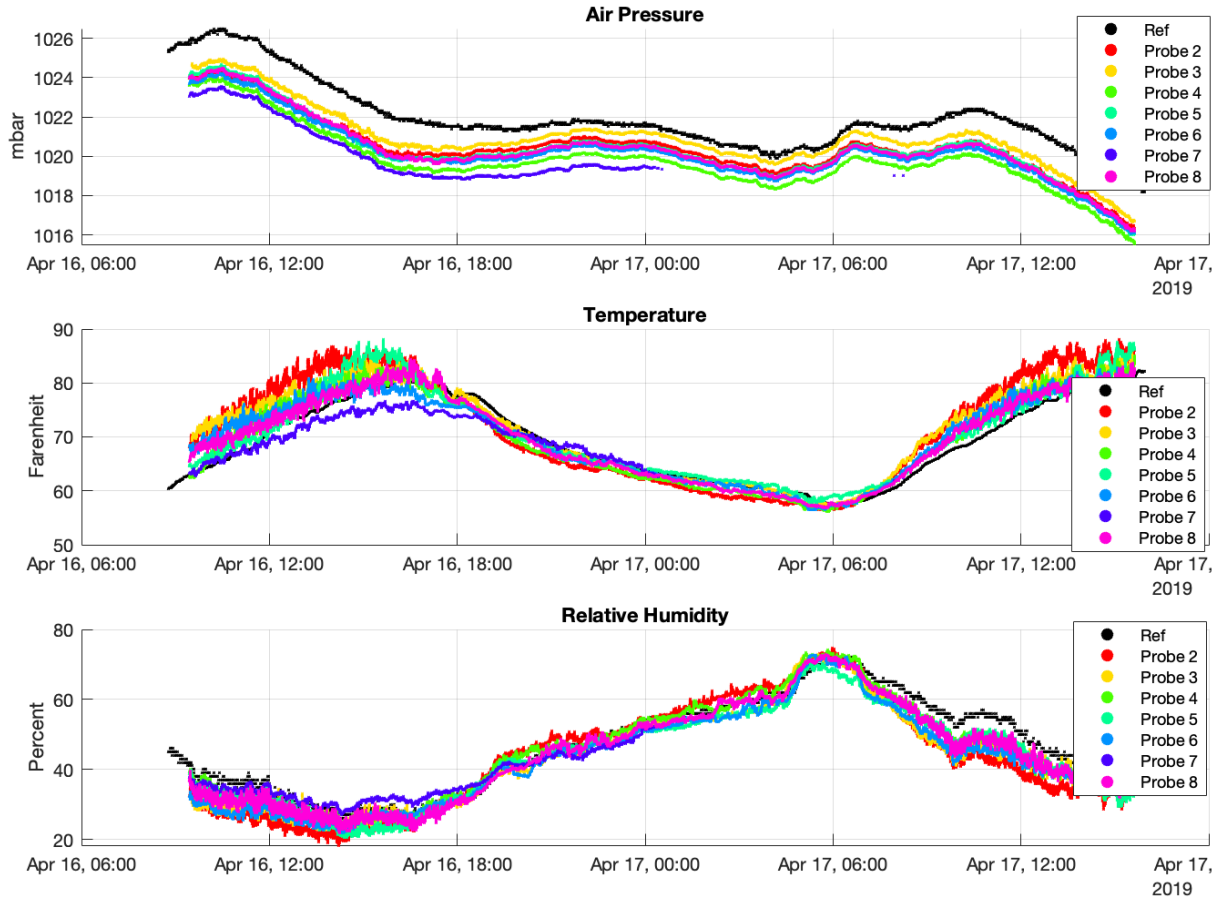

Figure 6.8: Overnight Sensor Test Results

From the data, it can be seen that the eMotes report very similar data during the night when there is no solar bias. During the day, Probes 2, 3, and 5 show significant solar bias as those sensors report temperatures nearly 10 degrees higher than the shaded probes. Similarly, these units show bias in the air pressure and humidity readings since these sensors use the recorded temperature in their calculations. Fortunately when the sensors are falling and are appropriately aspirated, the solar bias effects are mostly mitigated. Other issues with this test include the failure of Probe 7. The test was conducted by leaving the sensors unattended throughout the evening, and it appears around 1 am, either a person or an animal disturbed

Figure 6.9: Sensor Placement for Overnight Sensor Test

the sensor and destroyed the antenna which is why packets were no longer received. The test also included a reference sensor which had a shaded aspirated sensor suite. This reference closely aligns with the reported sensor data after sunset when the eMotes were shaded.

6.2.4 Scalability Testing

The eMote system is designed to include eMote sensors which transmit the collected atmospheric data back to a base station for processing [98]. Each RF front end is a Texas Instruments CC1101 radio module attached to a Tiva-C microcontroller configured to receive data from a single channel. Multiple RF front ends are networked together via Ethernet to a single computer, which runs several Python scripts to log the received data to both comma separated value (csv) files and a database for post-processing and real-time visualization

respectively. The RF front end includes both a hardware CRC check that will delete packets that have a bit error, as well as hardware FEC decoding.

The eMotes transmit in the 915 MHz ISM band which is 902 - 928 MHz. In this band, the eMotes transmit in 200 kHz channels, which allows for 130 channels. Within these channels, the eMotes utilize time division multiple access (TDMA) to slot each channel into 16 transmission slots. The eMotes' software assigns the transmission channel and time slot based on its assigned ID number. The eMotes use GPS time to synchronise their clocks for transmission. Under the typical configuration, each eMote transmits once per second. Each channel requires one RF front end, which are networked together and connected to a singular computer. If each channel was fully populated, up to 2080 eMotes could operate concurrently. The number of supported eMotes can be changed by increasing or decreasing the time between transmissions. This is 2 orders of magnitude more sensors than other previously developed systems. A system with this number of transmitters can allow for a much higher density of *in-situ* data collection and can tolerate the loss of several sensors without compromising the quality of the collected data.

To validate that the eMotes could properly utilize a TDMA scheme as designed, a scaled test was conducted on the campus of Auburn University on an open field. See Figure 6.10 to see the eMote placement. For this test, 83 eMotes were set in a field utilizing 6 channels. This test collected data for 126 minutes. Packets were reliably received from 90% of the eMotes and approximately 55% of the transmitted packets were received. In this test, the eMotes were located on the ground as was the receiver, so it is believed that multipath issues decreased the total number of received packets due to interference as the clearance conditions to reduce multipath discussed in Section 6.1.3 were not achieved.

6.3 Helikite Launches

To validate eMote field performance, the devices were tested in partnership with Sandia National Laboratories. Atmospheric researchers used the eMote in some testing on high

Figure 6.10: Test of 80 Coherent eMotes with Reported GPS Positions Mapped

density sensing in both Oliktok Point, Alaska and in the Chihuahuan Desert near White Sands, New Mexico. For Sandia's testing, they have a portable system with a 35 m^3 helikite with a lift capacity of 14.5 kg attached to a winch system that was used to lift the balloon along with their calibration sensors. A helikite is essentially a hybrid between a kite and a balloon where the kite tail allows the balloon to point with the wind. This system can be seen in Figure 6.11, and eMotes being lifted by a balloon can be seen in Figure 6.13.

6.3.1 New Mexico

In order to validate the eMote system, a test was conducted in the Chihuahuan Desert near White Sands, New Mexico on April 5^{th}, 2018. This test was conducted in partnership with Sandia National Laboratories. This site was utilized as the land is under restricted airspace R-5107B, which allowed the test group to exceed the 400 ft limitation for testing at

Figure 6.11: Balloon with Wench System

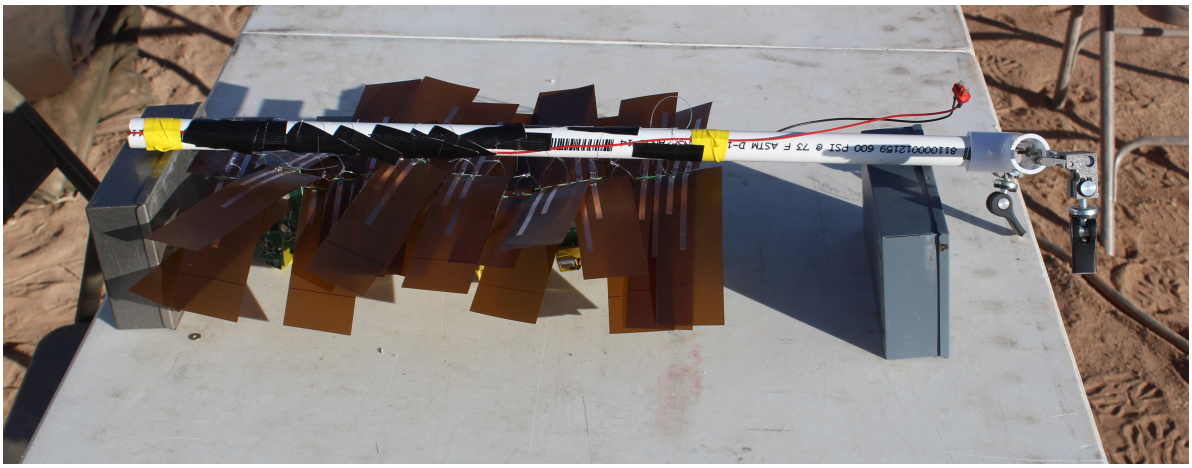

Figure 6.12: eMotes on Tethered Release

Auburn University. The test location was centered at 32.6180° north latitude, -106.70697° west longitude, and roughly 1,334 meters above sea level. For this experiment, three tests were conducted. The first test was a drop from 500 ft, the second test was a drop from 1000 ft, and the third test was completed at 500 ft above ground level. A fourth test at the maximum allowable altitude of 1500 ft was planned, but was not completed due to

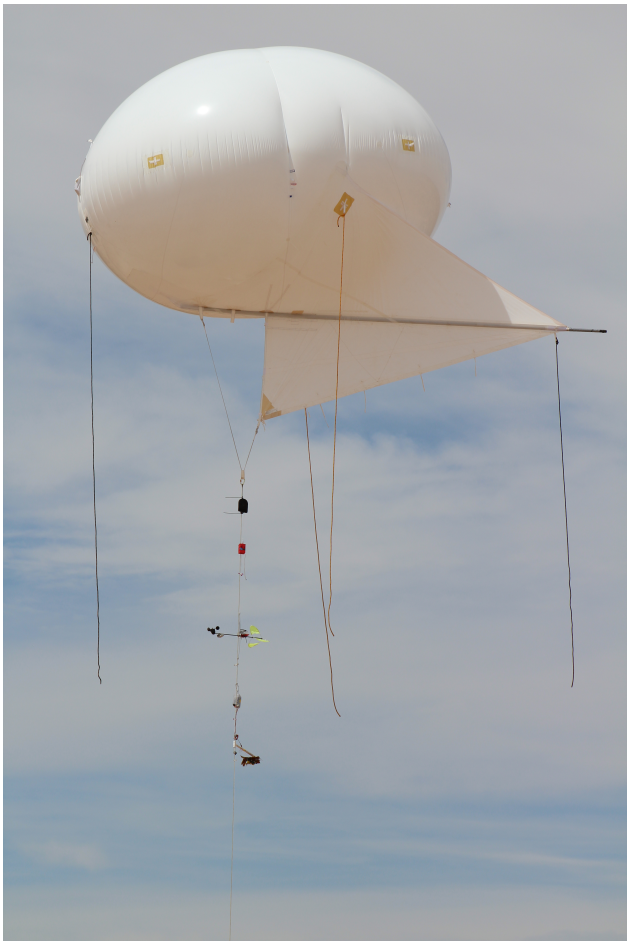

Figure 6.13: Balloon with Tethered eMotes and Reference Sensors

increasing wind speeds making eMote recovery difficult. Each test dropped approximately 15 eMotes. In Figure 6.14 you can see the eMotes on the balloon tether connected to the release mechanism, and in Figure 6.15 you can see the eMotes shortly after they are released. The images are still captures from GoPro cameras that were mounted to the tether which recorded video that was later analyzed.

In order to drop the eMotes remotely, the crew from Sandia created a system that can be seen in Figure 6.12. The device was a PVC boom which had a wire hanging below it which would heat up when current flowed through it. The eMotes were attached to the wire with a mono-filament fishing line where the line could be melted when heated to release the eMotes. The testing was conducted in a USDA protected research area so all eMotes and material had to be collected after the test was completed.

Figure 6.14: Image from Camera on Balloon Tether Showing eMotes before Falling

The first test went up to 500 ft and was conducted at approximately 9 am local time zone or 1400 UTC. This test had mild wind speeds with the average reported between 2 and 3 m/s by the anemometer mounted to the balloon tether. When the eMotes released, they fell in a fairly close pack until they landed in the desert.

The second test went up to 1000 ft before they were release and was conducted at approximately 1045 local time or 1645 UTC. This test had slightly stronger reported winds at 3 to 4 m/s with gusts reported up to 6 m/s. Since these eMotes were released from a higher altitude with higher winds, they drifted further from the drop site and had a larger spread upon landing. The landing positions of the eMotes can be see in Figure 6.16.

The final test was conducted later and at a lower altitude of 500 ft to account for the increased afternoon wind speeds. This test was conducted at 1300 local time or 1930 UTC. The reported wind speeds from the mounted anemometer were an average of 6 m/s with gusts exceeding 10 m/s. With the much higher winds, the eMotes spread more when falling, with the final positions shown in Figure 6.16.

Figure 6.15: eMotes After Release in New Mexico

6.3.2 Alaska

The Alaskan test was conducted by researchers from Sandia National Labs. The eMotes were tested in conjunction with other sensors. No members from Auburn went to assist with the test. For this test, 5 eMotes were elevated with a 79 m^3 helikite to an altitude of 1.25 km before they were released. In Figure 6.17 an image of the eMotes on the tether can be seen. There was some technical issue that was not noticed by the group from Sandia labs until after the test was completed and the eMotes were lost into the ocean, so only data from one eMote was collected successfully. The data from the one eMote did correlate with the data presented by their other sensors, so the test was deemed a partial success.

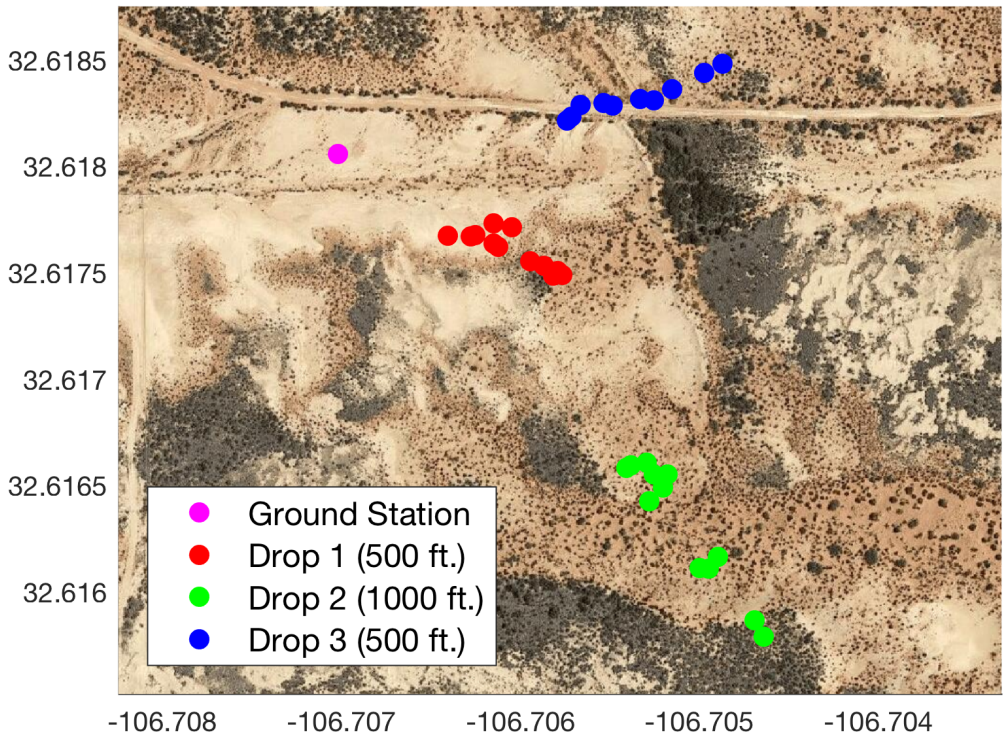

Figure 6.16: Map of Final Positions with GPS Coordinates

Figure 6.17: Image from Balloon in Alaska Test Showing eMotes

Chapter 7

Conclusion

In this dissertation, the design of antennas for an atmospheric probe has been presented. The work begins with a brief description of the origin of meteorology and weather sensing. The second chapter presents a quick overview of electromagnetics and antenna design then ends with a literature review in related state-of-the-art antenna design. Then, the third chapter presents the original design of dual PIFAs on a circular patch. In this, the shortcomings of such a design are explained along with a path forward. Chapter 4 presents an introduction to the design of flexible dipole antennas. Chapter 5 presents the design of dual flexible dipoles. The design of these antennas used biomimicry in a novel way to replicate the samara to generate autorotation when falling. Finally, the penultimate chapter presents a detailed listing of tests performed on the designed system.

The system designed is known as the GlobalSense eMote and is designed to improve contemporary *in-situ* atmospheric testing systems. Table 7.1 compares the eMote to the other commercially available sensors. From the table, it can be seen that the eMote vastly outperforms other sensors in all the categories except for range. In Section 6.1.3 a discussion is presented on how to increase the range to make the eMote more competitive in that regard. A final advantage the eMote presents is the comparatively low cost. The lowest cost commercial sensor, Vaisla's Radiosonde, sells for approximately $700 USD. While a market analysis of the eMote has not been conducted, the production run of 120 eMotes cost approximately $200 USD per device. If eMotes were produced in large quantities, it is estimated the production cost should drop below $100 USD per device, allowing them to be sold at a lower cost than the competition, even while maintaining a healthy profit.

Table 7.1: Comparison of eMote to State of the Art In-Situ Atmospheric Measuring Devices

Device	**Range (km)**	**Maximum Deployment**	**Fall Speed (m/s)**	**Weight (g)**
eMote	est. 20	2080	< 3	12
Qinetiq TASK [99]	150	2	unknown	88
Vaisala RD94 [7]	350	8	11 with parachute	350
Vaisala RS41 [100]	160	1	11 with parachute	113

The eMotes were tested and were shown to perform well both mechanically and electrically. The sensors were able to accurately collect data and transmit this data back to the receiver for post-processing. The devices fall significantly slower than any other device on the market and weigh approximately one-eighth that of the next closest competitor, reducing the risk of injury to people and damage to property when deployed.

The primary areas for improvement with the current device are an increased range and stable polarization of the antennas during falling. Solutions to both issues have been presented in this work. The range could be increased with the addition of an RF amplifier to increase the power output and thereby increase the range. The polarization could be solved by modifying the antenna structures. A path forward has been validated by simulation, but not physically realized due to time and budgetary constraints.

While forecasting has improved dramatically in recent centuries, more improvement is still needed. This is something specifically noticed in Alabama, where Auburn University is located, which has a high prevalence of violent, deadly tornadoes. Alabama is also hit by hurricanes, which cause significant damage and occasional loss of life. The most economical and effective way to reduce this loss of life is with more effective weather warning systems and improved forecasting [101]. Forecasting models would benefit from better *in-situ* data

collection devices, such as the GlobalSense eMote for which this dissertation presents the design of the novel antenna structure.

Bibliography

[1] Mary Reed. Weather talk: Weather god of the Hittites. *Weatherwise*, 44(2):38–39, 1991.

[2] India Meteorological Department. History of meteorological services in India, 2015.

[3] G. Hellmann. The dawn of meteorology. *Quarterly Journal of the Royal Meteorological Society*, 34(148):221–232, 1908.

[4] Aristotle. Meteorology, 350 B.C.E. Translated by E. W. Webster.

[5] Cleveland Abbe. The physical basis of long-range weather forecasts. *Monthly Weather Review*, 29(12):551–561, 1901.

[6] NOAA. The history of numerical weather prediction, 2017. celebrating200years.noaa.gov/foundations/numerical_wx_pred/.

[7] Vaisala. Vaisala dropsonde RD94, 2010.

[8] Murty Divakarla, Christopher Barnet, Mitchell Goldberg, Eric Maddy, Walter Wolf, Lawrence Flyn, Xiaozhen Xiong, Jennifer Wei, Lihang Zhou, and Xingpin Liu. Validation of atmospheric infrared sounder temperature and water vapor retrievals with matched radiosonde measurements and forecasts. *Journal of Geophysical Research*, 111(D9), 2006.

[9] William R. Moninger, Richard D. Mamrosh, and Patricia M. Pauley. Automated meteorological reports from commercial aircraft. *Bulletin of the American Meteorological Society*, 84(2):203–216, 2003.

[10] Jeffrey K. Lazo, Megan Lawson, Peter H. Larsen, and Donald M. Waldman. U.s. economic sensitivity to weather variability. *Bulletin of the American Meteorological Society*, 92(6):709–720, 2011.

[11] Thomas J. Teisberg, Rodney F. Weiher, and Alireza Khotanzad. The economic value of temperature forecasts in electricity generation. *Bulletin of the American Meteorological Society*, 86(12):1765–1771, 2005.

[12] Timothy A. Coleman and P. Grady Dixon. An objective analysis of tornado risk in the United States. *Weather and Forecasting*, 29(2):366–376, 2014.

[13] John Manobianco. Global environmental MEMS sensors (GEMS): A revolutionary observing system for the 21st century. *NOAA SBIR Phase I Final Report*, 2002.

[14] John Manobianco. Global environmental MEMS sensors (GEMS): A revolutionary observing system for the 21st century. *Phase II Final Report*, 2005.

[15] ANSYS Electronics Desktop, 2016. http://www.ansys.com/Products/Electronics/ANSYS-Electronics-Desktop.

[16] LPKF Laser and Electronics. Lpkf protomat s103: The specialist for RF- and microwave applications. http://www.lpkfusa.com/datasheets/prototyping/s103.pdf.

[17] Keysight. Keysight technologies fieldfox handheld analyzers. http://literature.cdn.keysight.com/litweb/pdf/5990-9783EN.pdf?id=2210837.

[18] Tektronix. Rsa306b usb real time spectrum analyzer datasheet. http://www.tek.com/datasheet/rsa306b-usb-real-time-spectrum-analyzer-0.

[19] Stuart Wentworth. *Applied Electromagnetics: Early Transmission Lines Approach*. Wiley, Hoboken, NJ, 2007.

[20] John Arthur. The fundamentals of electromagnetic theory revisited. *IEEE Antennas and Propagation Magazine*, 50(1):19–65, 2008.

[21] Umran S Inan, Aziz S Inan, and Ryan K Said. *Engineering Electromagnetics and Waves*. Prentice Hall, 2nd edition, 2015.

[22] David M. Pozar. *Microwave Engineering*. Wiley, New York, 4th edition, 2012.

[23] W. L. Stutzman and G. A. Thiele. *Antenna Theory and Design*. John Wiley and Sons, Inc., 3rd edition, 2013.

[24] J. Craig Prather. Dual antenna design for a novel airborne probe. Master's thesis, Auburn University, 2016.

[25] Roger F. Harrington. *Field Computation by Moment Methods*. Wiley-IEEE Press, 1993.

[26] Constantine A. Balanis. *Advanced Engineering Electromagnetics*. John Wiley & Sons, 2nd edition, 2012.

[27] J. C. Prather, M. Bolt, T. Horton, B. Bottenfield, S. Wentworth, and M. L. Adams. Biomimetic antenna design for an airborne atmospheric probe. *IEEE Transactions on Antennas and Propagation*, 67(1):48–55, Jan 2019.

[28] D. Rialet, A. Sharaiha, A. C. Tarot, and C. Delaveaud. Characterization of antennas on dielectric and magnetic substrates effective medium approximation. In *2009 3rd European Conference on Antennas and Propagation*, pages 3163–3166, March 2009.

[29] Keysight's momentum 3d planar em simulator, Version 2015. http://www.keysight.com/en/pc-1887116/momentum-3d-planar-em-simulator?nid=-33748.0&cc=US&lc=eng.

[30] Interface Specification IS-GPS-200H. Technical report, United States. Global Positioning Systems Directorate. Systems Engineering and Integration, 2013.

[31] Interface Specification IS-GPS-705 Revision d. Technical report, United States. Global Positioning Systems Directorate. Systems Engineering and Integration, September 2013.

[32] J. Garcia, A. Arriola, F. Casado, X. Chen, J. I. Sancho, and D. Valderas. Coverage and read range comparison of linearly and circularly polarised radio frequency identification ultra-high frequency tag antennas. *IET Microwaves, Antennas Propagation*, 6(9):1070–1078, June 2012.

[33] C. J. Hegarty and E. Chatre. Evolution of the global navigation satellite system (GNSS). *Proceedings of the IEEE*, 96(12), Dec 2008.

[34] Jacek Januszewski. GNSS frequencies, signals, receiver capabilities and applications. *Scientific Journals Maritime University of Szczecin*, 54:57–62, 2018.

[35] Joe Dichoso. FCC Basics of Unlicensed Transmitters. Technical report, Federal Communications Commission Office of Engineering Technology Laboratory Division, October 2007.

[36] International Telecommunication Union. Radio regulations, 2017.

[37] Understanding the FCC Regulations for Low-Power, Non-Licensed Transmitters. Technical report, Office of Engineering and Technology Federal Communications Commission, February 1996.

[38] Y. T. Lo and S. W. Lee, editors. *Antenna Handbook*, volume 2. Van Nostrand Reinhold, New York, 1993.

[39] Kin-Lu Wong, editor. *Compact and Broadband Microstrip Antennas*. John Wiley and Sons, New York, 2002.

[40] D. H. Smithgall and G. A. Wright. Quarter wave patch antenna, November 30 1999. US Patent 5,995,048.

[41] H. Iwasaki. A circularly polarized small-size microstrip antenna with a cross slot. *IEEE Transactions on Antennas and Propagation*, 44(10):1399–1401, Oct 1996.

[42] P. Sharma and K. Gupta. Analysis and optimized design of single feed circularly polarized microstrip antennas. *IEEE Transactions on Antennas and Propagation*, 31(6):949–955, Nov 1983.

[43] Chih-Yu Huang, Jian-Yi Wu, and Kin-Lu Wong. Cross-slot-coupled microstrip antenna and dielectric resonator antenna for circular polarization. *IEEE Transactions on Antennas and Propagation*, 47(4):605–609, April 1999.

[44] C. W. Su and J. S. Row. Slot-coupled microstrip antenna for broadband circular polarisation. *Electronics Letters*, 42(6):318–319, March 2006.

[45] X. L. Bao and M. J. Ammann. Dual-frequency circularly-polarized patch antenna with compact size and small frequency ratio. *IEEE Transactions on Antennas and Propagation*, 55(7):2104–2107, July 2007.

[46] F. Ferrero, C. Luxey, G. Jacquemod, and R. Staraj. Dual-band circularly polarized microstrip antenna for satellite applications. *IEEE Antennas and Wireless Propagation Letters*, 4:13–15, June 2005.

[47] Adam Z. Narbudowicz. *Advanced Circularly Polarised Microstrip Patch Antennas*. PhD thesis, Dublin Institute of Technology, 2013.

[48] Upadhyaya N. Rijal, Junping Geng, Xianling Liang, Ronghong Jin, Xiang Liu, and Kun Wang. Study on the planar circularly polarized antennas with swastika slot. *Progress In Electromagnetics Research C*, 39:11–24, 2013.

[49] N. C. Karmakar and M. E. Bialkowski. Circularly polarized aperture-coupled circular microstrip patch antennas for L-band applications. *IEEE Transactions on Antennas and Propagation*, 47(5):933–940, May 1999.

[50] D. M. Pozar and S. M. Duffy. A dual-band circularly polarized aperture-coupled stacked microstrip antenna for global positioning satellite. *IEEE Transactions on Antennas and Propagation*, 45(11):1618–1625, Nov 1997.

[51] Fa-Shian Chang, Kin-Lu Wong, and Tzung-Wern Chiou. Low-cost broadband circularly polarized patch antenna. *IEEE Transactions on Antennas and Propagation*, 51(10):3006–3009, Oct 2003.

[52] J. W. Baik, T. H. Lee, S. Pyo, S. M. Han, J. Jeong, and Y. S. Kim. Broadband circularly polarized crossed dipole with parasitic loop resonators and its arrays. *IEEE Transactions on Antennas and Propagation*, 59(1):80–88, Jan 2011.

[53] Wen-Shyang Chen, Kin-Lu Wong, and Chun-Kun Wu. Inset microstripline-fed circularly polarized microstrip antennas. *IEEE Transactions on Antennas and Propagation*, 48(8):1253–1254, Aug 2000.

[54] A. Petosa, N. Simons, R. Siushansian, A. Ittipiboon, and M. Cuhaci. Design and analysis of multisegment dielectric resonator antennas. *IEEE Transactions on Antennas and Propagation*, 48(5):738–742, May 2000.

[55] B. Mukherjee, P. Patel, and J. Mukherjee. Hemispherical dielectric resonator antenna based on apollonian gasket of circles - a fractal approach. *IEEE Transactions on Antennas and Propagation*, 62(1):40–47, Jan 2014.

[56] K. L. Wong and C. H. Chang. Printed $\lambda/8$-pifa for internal penta-band mobile phone antenna. In *2009 3rd European Conference on Antennas and Propagation*, pages 533–537, March 2009.

[57] C. R. Rowell and R. D. Murch. A capacitively loaded pifa for compact mobile telephone handsets. *IEEE Transactions on Antennas and Propagation*, 45(5):837–842, May 1997.

[58] A. Cabedo, J. Anguera, C. Picher, M. Ribo, and C. Puente. Multiband handset antenna combining a pifa, slots, and ground plane modes. *IEEE Transactions on Antennas and Propagation*, 57(9):2526–2533, Sept 2009.

[59] D. M. Nashaat, H. A. Elsadek, and H. Ghali. Single feed compact quad-band pifa antenna for wireless communication applications. *IEEE Transactions on Antennas and Propagation*, 53(8):2631–2635, Aug 2005.

[60] R. Feick, H. Carrasco, M. Olmos, and H. D. Hristov. Pifa input bandwidth enhancement by changing feed plate silhouette. *Electronics Letters*, 40(15):921–922, July 2004.

[61] K. L. Virga and Y. Rahmat-Samii. Low-profile enhanced-bandwidth pifa antennas for wireless communications packaging. *IEEE Transactions on Microwave Theory and Techniques*, 45(10):1879–1888, Oct 1997.

[62] M. Bolt, J. C. Prather, H. Harrell, T. Horton, J. Manobianco, and M. L. Adams. Design and testing of novel airborne atmospheric sensor nodes. *IEEE Geoscience and Remote Sensing Letters*, 15(1):73–77, Jan 2018.

[63] A. Cihangir, C. J. Panagamuwa, W. G. Whittow, F. Gianesello, and C. Luxey. Ultra-broadband antenna with robustness to body detuning for 4G eyewear devices. *IEEE Antennas and Wireless Propagation Letters*, 16:1225–1228, 2017.

[64] K. L. Wong and S. C. Chen. Printed single-strip monopole using a chip inductor for penta-band WWAN operation in the mobile phone. *IEEE Transactions on Antennas and Propagation*, 58(3):1011–1014, March 2010.

[65] Bin Lin, Jianhua Zhou, and Baiqiang You. A novel printed folded dipole antenna used for modern RFID system. In *2008 Third International Conference on Communications and Networking in China*, pages 774–778, Aug 2008.

[66] Kuan Lee, J. Clark, Ruey Chu, Nam Wong, and R. Tang. A dual band phased array using interleaved waveguides and dipoles printed on high dielectric substrate. In *1984 Antennas and Propagation Society International Symposium*, volume 22, pages 886–889, Jun 1984.

[67] Young-Ho Suh and Kai Chang. A new millimeter-wave printed dipole phased array antenna using microstrip-fed coplanar stripline Tee junctions. *IEEE Transactions on Antennas and Propagation*, 52(8):2019–2026, Aug 2004.

[68] Clement Mbinack and Emmanuel Tonye. Numerical calculation and design of variant topologies of printed dipole antennas. *International Journal of Science and Research*, 5(7):895 – 899, July.

[69] Qing Liu, K. Lee Ford, R. Langley, A. Robinson, and S. Lacour. Flexible dipole and monopole antennas. In *Proceedings of the 5th European Conference on Antennas and Propagation (EUCAP)*, pages 2052–2056, April 2011.

[70] Rameez Shamalik and Sushama Shelke. Design and simulation of flexible antenna for ISM band. *International Journal of Engineering Research and Applications (IJERA)*, 2(3):2248–9622, 2012.

[71] Y. Liu, X. Zang, Changle Li, Shuai Heng, Z. Lin, and J. Zhao. Design and control of a pneumatic-driven biomimetic knee joint for biped robot. In *2017 IEEE International Conference on Advanced Intelligent Mechatronics (AIM)*, pages 70–75, July 2017.

[72] G. Zhong, L. Chen, Z. Jiao, J. Li, and H. Deng. Locomotion control and gait planning of a novel hexapod robot using biomimetic neurons. *IEEE Transactions on Control Systems Technology*, PP(99):1–13, 2017.

[73] N. F. Lepora. Biomimetic active touch with fingertips and whiskers. *IEEE Transactions on Haptics*, 9(2):170–183, April 2016.

[74] Evan Ackerman. DARPA concludes nano air vehicle program, we wonder what's next. *IEEE Spectrum*, Jan 2011.

[75] M. Ranjbar Nikkhah, K. Ghaemi, and N. Behdad. A three-element biomimetic antenna array with an electrically small triangular lattice. *IEEE Transactions on Antennas and Propagation*, 65(8):4007–4016, Aug 2017.

[76] A. R. Masoumi, Y. Yusuf, and N. Behdad. Biomimetic antenna arrays based on the directional hearing mechanism of the parasitoid fly ormia ochracea. *IEEE Transactions on Antennas and Propagation*, 61(5):2500–2510, May 2013.

[77] F. M. Burrows. Wind-borne seed and fruit movement. *The New Phytologist*, 75(2):405–418, 1975.

[78] Douglas S. Green. The terminal velocity and dispersal of spinning samaras. *American Journal of Botany*, 67(8):1218–1224, 1980.

[79] Paul Pounds, Timothy Potie, Farid Kendoul, Surya Singh, Raja Jurdak, and Jonathan Roberts. *Automatic Distribution of Disposable Self-Deploying Sensor Modules*, pages 535–543. Springer International Publishing, Cham, 2016.

[80] Robert A. Stevenson, Dennis Evangelista, and Cindy V Looy. When conifers took flight: a biomechanical evaluation of an imperfect evolutionary takeoff. *Paleobiology*, 41(2):205 – 225, 2015.

[81] R. Ake Norberg. Autorotation, self-stability, and structure of single-winged fruits and seeds (samaras) with comparative remarks on animal flight. *Biological Reviews*, 48(4):561–596, 1973.

[82] D. Lentink, W. B. Dickson, J. L. van Leeuwen, and M. H. Dickinson. Leading-edge vortices elevate lift of autorotating plant seeds. *Science*, 324:1438– 1440, 2009.

[83] Kapil Varshney, Song Chang, and Z Jane Wang. The kinematics of falling maple seeds and the initial transition to a helical motion. *Nonlinearity*, 25(1):C1, 2012.

[84] Rogers Corporation. Ultralam 3000 liquid crystalline polymer circuit material double-clad laminates: Data sheet, 2015. https://www.rogerscorp.com/documents/730/acm/ULTRALAM-3000-LCP-laminate-data-sheet-ULTRALAM-3850.aspx.

[85] DuPont. DuPont Pyralux AP technical data sheet, 2012. https://www.dupont.com/content/dam/Dupont2.0/Products/Electronics-and-imaging/Literature/PyraluxAPclad_DataSheet.pdf .

[86] DuPont. DuPont Pyralux TK technical data sheet, 2015. https://www.dupont.com/content/dam/Dupont2.0/Products/Electronics-and-imaging/Literature/Pyralux_TK_DataSheet.pdf.

[87] Y. Zhou. Development of a polyimide-based flexible antenna. In *2013 USNC-URSI Radio Science Meeting (Joint with AP-S Symposium)*, pages 68–68, July 2013.

[88] A. Moussessian, L. Del Castillo, J. Huang, G. Sadowy, J. Hoffman, P. Smith, T. Hatake, C. Derksen, B. Lopez, and E. Caro. An active membrane phased array radar. In *IEEE MTT-S International Microwave Symposium Digest, 2005.*, pages 1–4, June 2005.

[89] W. J. Vogel and U. S. Hong. Measurement and modeling of land mobile satellite propagation at UHF and L-band. *IEEE Transactions on Antennas and Propagation*, 36(5):707–719, May 1988.

[90] Bell Labs. Anechoic chamber: History of the anechoic chamber and fundamental acoustics research, 2019. https://www.bell-labs.com/anechoic-chamber/.

[91] Theodore S. Rappaport. *Wireless Communications Principles and Practices*. Prentice Hall, 2nd edition, 2002.

[92] J. Meguro, T. Murata, J. Takiguchi, Y. Amano, and T. Hashizume. GPS multipath mitigation for urban area using omnidirectional infrared camera. *IEEE Transactions on Intelligent Transportation Systems*, 10(1):22–30, March 2009.

[93] S. Bauer, M. Obst, and G. Wanielik. 3D environment modeling for GPS multipath detection in urban areas. In *International Multi-Conference on Systems, Sygnals Devices*, pages 1–5, March 2012.

[94] Christian Dussault, Rhaume Courtois, Jean-Pierre Ouellet, and Jean Huot. Influence of satellite geometry and differential correction on GPS location accuracy. *Wildlife Society Bulletin (1973-2006)*, 29(1):171–179, 2001.

[95] P Ptasinski, F Cecelja, and W Balachandran. Altitude aiding for GPS systems using elevation map datasets. *The Journal of Navigation*, 55(3):451–462, 2002.

[96] World Meteorological Organization. Observing systems capability analysis and review tool, 2017.

[97] National Oceanic and Atmospheric Administration. NWS directives system, 2017.

[98] Tyler Horton, Michael Bolt, J. Craig Prather, John Manobianco, and Mark L. Adams. Airborne sensor network for atmospheric profiling. *Wireless Sensor Network*, 10(4):93–101, April 2018.

[99] Qinetiq. TASK: tactical atmospheric sounding kit, 2015.

[100] Vaisala. Vaisala radiosonde RS41-D, 2018.

[101] Kevin M. Simmons and Daniel Sutter. The 2011 tornadoes and the future of tornado research. *Bulletin of the American Meteorological Society*, 93(7):959–961, 2012.

Appendix A

Appendix

A.1 3D Antenna Patterns

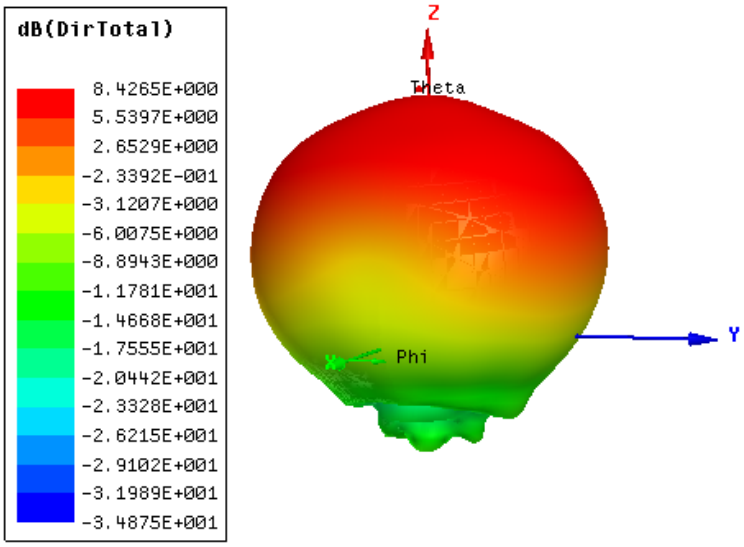

Figure A.1: Simulated 3D Antenna Pattern of the PIFA ISM Band Antenna

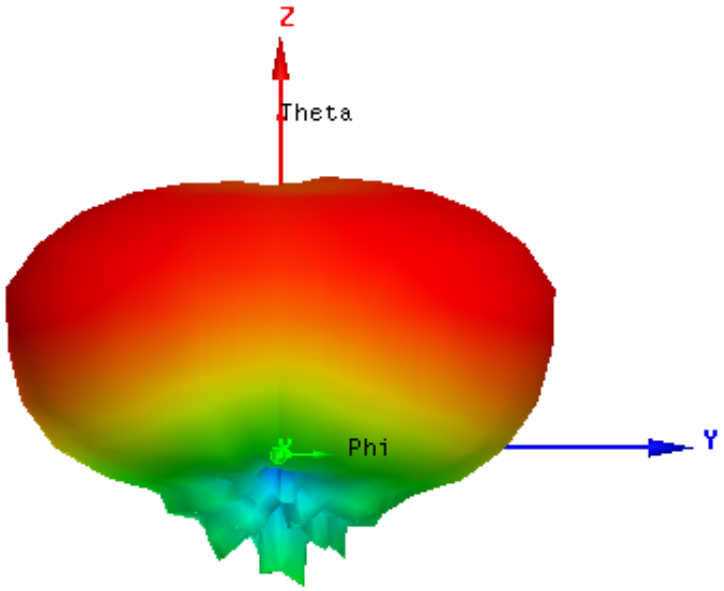

Figure A.2: Simulated 3D Antenna Pattern of the PIFA GPS Antenna

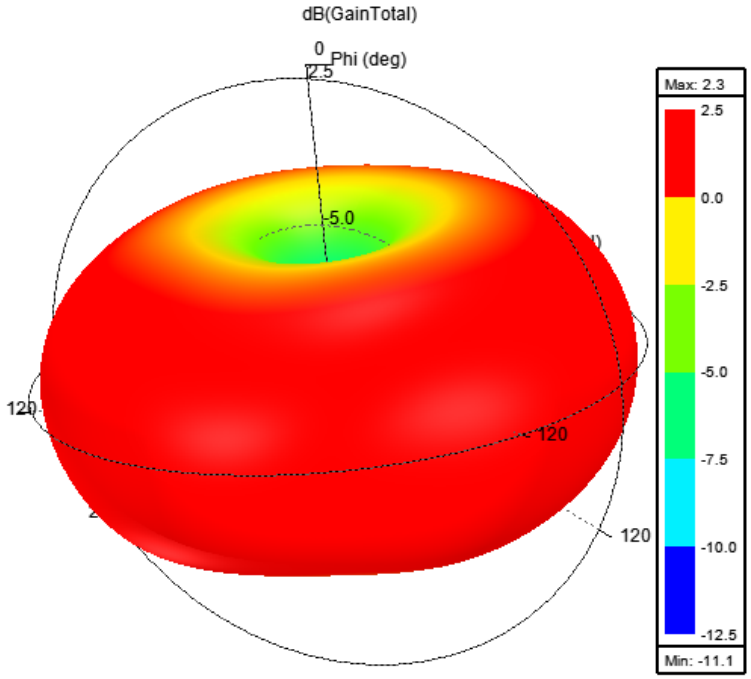

Figure A.3: Simulated 3D Antenna Pattern of the Flexible Dipole

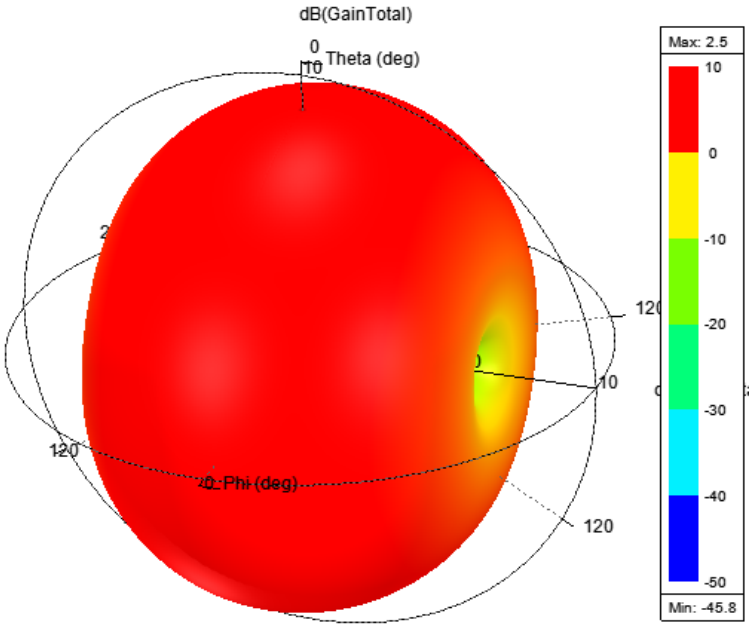

Figure A.4: Simulated 3D Antenna Pattern of the ISM Band Dipole

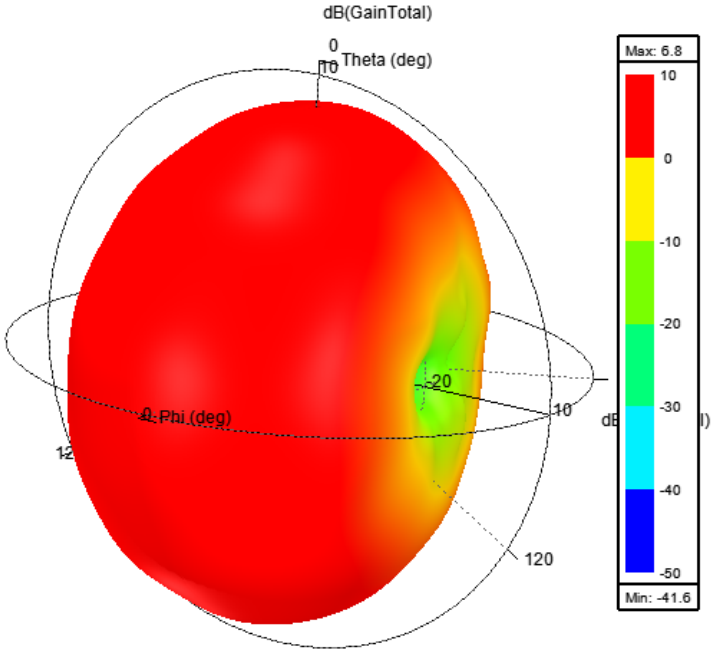

Figure A.5: Simulated 3D Antenna Pattern of the GPS L1 Band Dipole from Front

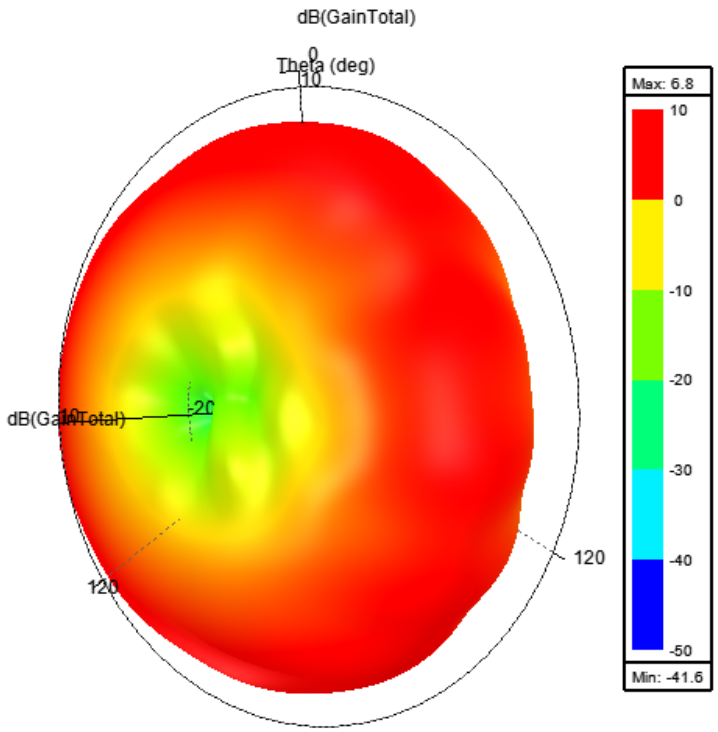

Figure A.6: Simulated 3D Antenna Pattern of the GPS L1 Band Dipole from Side Showing Distortions

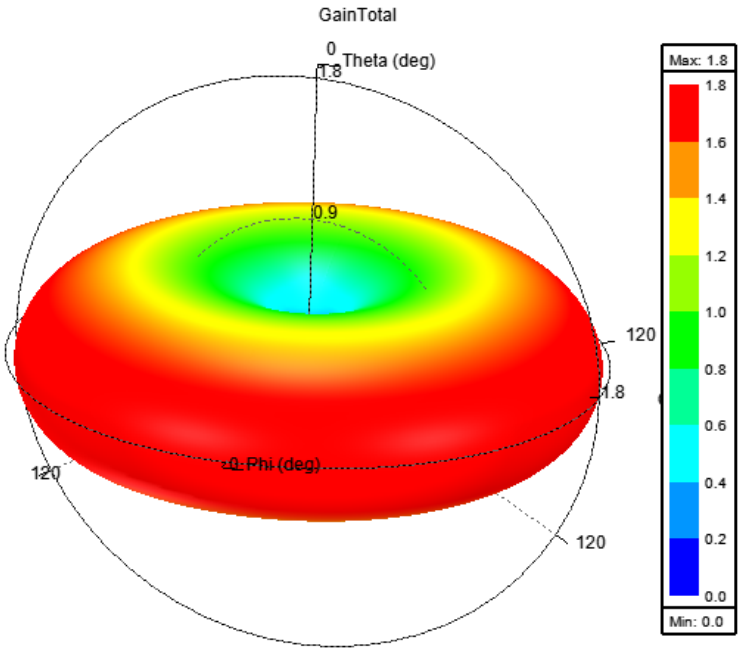

Figure A.7: Simulated 3D Antenna Pattern of the Vertically Polarized Dipole

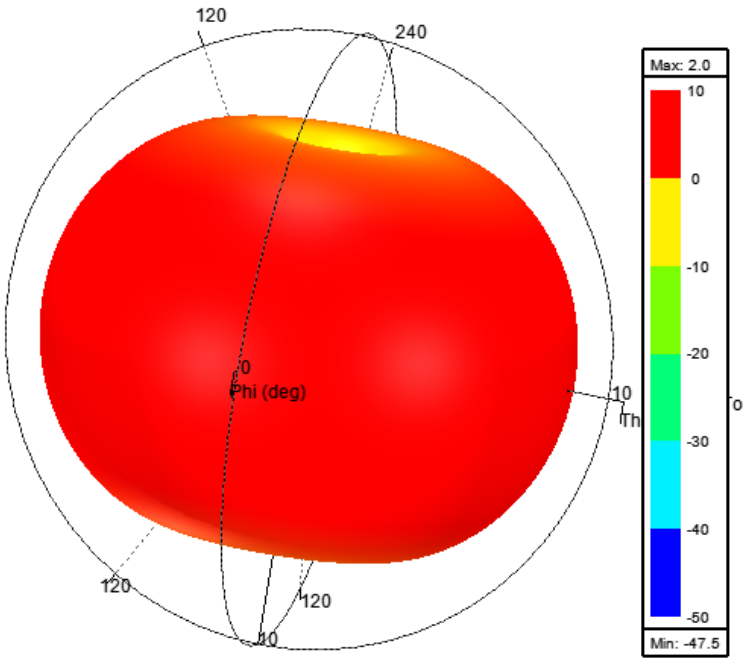

Figure A.8: Simulated 3D Antenna Pattern of the Vertically Polarized ISM Dipole

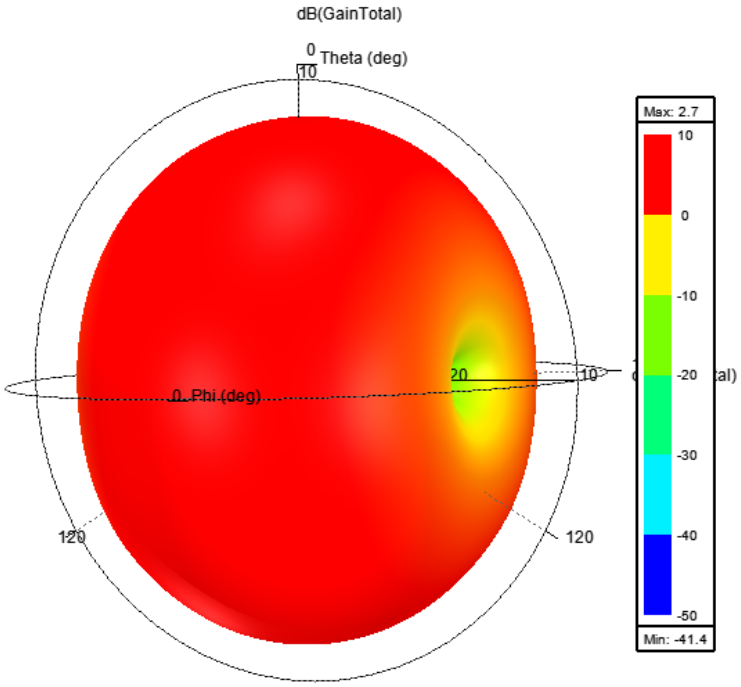

Figure A.9: Simulated 3D Antenna Pattern of the GPS Dipole with Vertically Polarized Dipole

A.2 MATLAB Code for Antennas Toolbox Wire Dipole

```
% Craig Prather May 2018
% Based off MATLAB Example Code
% This program requires Antenna Toolbox be installed to run
% This will design and simulate a Linear Wire Antenna
% user also needs to input f (freq) and a (wire width)
% current version calculates for 2 input widths (at & aw)

close all; clc; format compact;
f=1e9;          %design freq in Hz
at = 0.0015;    %thiner thickness of wire
aw = 0.004;     %wider thickness of wire
c = 3e8;
lam = c/f;      %lambda at design freq
freq = linspace(1e3,f*4,401);   %freq range to plot over
%f2 = linspace(1e3,f*2,201);     %for smaller range of F
L=lam/2; %length of 1 m

%Ant = design(dipole,f) %uncomment to let MATLAB design antenna at f
%this will create thinner dipoles
Ant= dipole('Length',L,'Width',at);
Ant4= dipole('Length',L,'Width',at,'FeedOffset',L*.25);
Ant8= dipole('Length',L,'Width',at,'FeedOffset',L*.5-L*1/8);
Ant38= dipole('Length',L,'Width',at,'FeedOffset',L*.5-L*3/8);
%this will create wider dipoles
Antw= dipole('Length',L,'Width',aw);
Ant4w= dipole('Length',L,'Width',aw,'FeedOffset',L*.25);
Ant8w= dipole('Length',L,'Width',aw,'FeedOffset',L*.5-L*1/8);
Ant38w= dipole('Length',L,'Width',aw,'FeedOffset',L*.5-L*3/8);

%% This will show the designed wider dipoles
show(Antw)
set(gca,'fontsize', 16);
title('Wider Antenna')
figure
show(Ant4w)
set(gca,'fontsize', 16);
title('Fed offset by L/4')
figure
show(Ant8w)
set(gca,'fontsize', 16);
title('Fed offset by L/8')
figure
show(Ant38w)
set(gca,'fontsize', 16);
title('Fed offset by L*3/8')
%% Use break points to step through as desired
figure; %this fig will show the dipole with mesh overlaid
mesh(Antw)
set(gca,'fontsize', 16);

figure;%will show current distribution on thin dipole
```

```
current(Ant,f)
view(90,0)
set(gca,'fontsize',16);
title('Current Distribution on Thinner Antenna')

figure;%will show current distribution on wider dipole
current(Ant,f)
view(90,0)
set(gca,'fontsize',16);
title('Current Distribution on Wider Antenna')

%% This will calculate the input impedence and VSWR for each designed ant
Z = impedance(Ant, freq);
Z4 = impedance(Ant4, freq);
Z8 = impedance(Ant8, freq);
Z38 = impedance(Ant38, freq);
Zw = impedance(Antw, freq);
Z4w = impedance(Ant4w, freq);
Z8w = impedance(Ant8w, freq);
Z38w = impedance(Ant38w, freq);

%%%% PLOT Z AND X FOR THINNER DIPOLE %%%%
figure;
subplot(2,1,1) %will plot just Real part of Z
plot(freq,real(Z),'linewidth',2)
%ylim([-0,2000]) %limit Y axis
xticks([0*f f 2*f 3*f 4*f])
xticklabels({'0','.5','1','1.5','2'})
grid on;
ylabel('Input Resistance (Ra) \Omega')
%xlabel('L/\lambda')
legend(sprintf('a = %g\\lambda', at))
title('Input R and X for Dipole Antenna')
set(gca,'fontsize', 14);

subplot(2,1,2) %will plot only reactance
plot(freq,imag(Z),'linewidth',2)
ylim([-1000,800])
xticks([0*f f 2*f 3*f 4*f])
xticklabels({'0','.5','1','1.5','2'})
grid on
ylabel('Input Reactance (Xa) \Omega')
xlabel('L/\lambda')
legend(sprintf('a = %g\\lambda', at))
set(gca,'fontsize', 14);

%%%% PLOT G AND B FOR THINNER DIPOLE %%%%
figure;
subplot(2,1,1) %will plot only G conductance
plot(freq,real(Z.^-1),'linewidth',2)
hold on
plot(freq,real(Z8.^-1),'linewidth',2)
plot(freq,real(Z4.^-1),'linewidth',2)
plot(freq,real(Z38.^-1),'linewidth',2)
```

```
%ylim([-2000,2000])
xticks([0*f f 2*f 3*f 4*f])
xticklabels({'0','.5','1','1.5','2'})
grid on
ylabel('G (Conductance) \Omega')
xlabel('L/\lambda')
legend('Source at Center','Source at \lambda/8','Source at \lambda/4',...
    'Source at \lambda*3/8')
title('Input G and B at Various Feed Locations for Thin Antenna')
set(gca,'fontsize', 16);

subplot(2,1,2) %will plot only B susceptance
plot(freq,imag(Z.^-1),'linewidth',2)
hold on
plot(freq,imag(Z8.^-1),'linewidth',2)
plot(freq,imag(Z4.^-1),'linewidth',2)
plot(freq,imag(Z38.^-1),'linewidth',2)
%ylim([-2000,2000])
xticks([0*f f 2*f 3*f 4*f])
xticklabels({'0','.5','1','1.5','2'})
grid on
ylabel('B (Susceptance) \Omega')
xlabel('L/\lambda')
legend('Source at Center','Source at \lambda/8','Source at \lambda/4',...
    'Source at \lambda*3/8')
set(gca,'fontsize', 16);

%%%% PLOT Z AND X FOR WIDER DIPOLE %%%%
figure;
subplot(2,1,1) %will plot just Real part of Z
plot(freq,real(Zw),'linewidth',2)
%ylim([-0,2000])
xticks([0*f f 2*f 3*f 4*f])
xticklabels({'0','.5','1','1.5','2'})
grid on;
ylabel('Input Resistance (Ra) \Omega')
%xlabel('L/\lambda')
legend(sprintf('a = %g\\lambda', at))
title('Input R and X for Wide Antenna')
set(gca,'fontsize', 16);

subplot(2,1,2) %will plot only reactance
plot(freq,imag(Zw),'linewidth',2)
ylim([-1000,800])
xticks([0*f f 2*f 3*f 4*f])
xticklabels({'0','.5','1','1.5','2'})
grid on
ylabel('Input Reactance (Xa) \Omega')
xlabel('L/\lambda')
legend(sprintf('a = %g\\lambda', at))
set(gca,'fontsize', 16);

%%%% PLOT G AND B FOR WIDER DIPOLE %%%%
figure;
```

```
subplot(2,1,1) %will plot only G conductance
plot(freq,real(Zw.^-1),'linewidth',2)
hold on
plot(freq,real(Z8w.^-1),'linewidth',2)
plot(freq,real(Z4w.^-1),'linewidth',2)
plot(freq,real(Z38w.^-1),'linewidth',2)
%ylim([-2000,2000])
xticks([0*f f 2*f 3*f 4*f])
xticklabels({'0','.5','1','1.5','2'})
grid on
ylabel('G (Conductance) \Omega')
xlabel('L/\lambda')
legend('Source at Center','Source at \lambda/8','Source at \lambda/4',...
    'Source at \lambda*3/8')
title('Input G and B at Various Feed Locations for Wide Antenna')
set(gca,'fontsize', 16);

subplot(2,1,2) %will plot only B susceptance
plot(freq,imag(Zw.^-1),'linewidth',2)
hold on
plot(freq,imag(Z8w.^-1),'linewidth',2)
plot(freq,imag(Z4w.^-1),'linewidth',2)
plot(freq,imag(Z38w.^-1),'linewidth',2)
%ylim([-2000,2000])
xticks([0*f f 2*f 3*f 4*f])
xticklabels({'0','.5','1','1.5','2'})
grid on
ylabel('B (Susceptance) \Omega')
xlabel('L/\lambda')
legend('Source at Center','Source at \lambda/8','Source at \lambda/4',...
    'Source at \lambda*3/8')
set(gca,'fontsize', 16);

%% Plot the VSWR
%%%% PLOT VSWR FOR THINNER DIPOLE %%%%
figure;
Vant=vswr(Ant, freq);
Vant4=vswr(Ant4,freq);
Vant8=vswr(Ant8,freq);
Vant38=vswr(Ant38,freq);
plot(freq/1e9,Vant,freq/1e9,Vant8,freq/1e9,Vant4,freq/1e9,Vant38,...
    'linewidth',2)
legend('Source at Center','Source at \lambda/8','Source at \lambda/4',...
    'Source at \lambda*3/8')
grid on
ylim([1 10])
ylabel('VSWR')
xlabel('Frequency (GHz)')
xlim([0.6 1.4])
title('VSWR for Thin Antenna')
set(gca,'fontsize', 16);

%%%% PLOT VSWR FOR WIDER DIPOLE %%%%
figure;
```

```
Vant=vswr(Antw, freq);
Vant4=vswr(Ant4w,freq);
Vant8=vswr(Ant8w,freq);
Vant38=vswr(Ant38w,freq);
plot(freq/1e9,Vant,freq/1e9,Vant8,freq/1e9,Vant4,freq/1e9,Vant38,...
    'linewidth',2)
legend('Source at Center','Source at \lambda/8','Source at \lambda/4',...
    'Source at \lambda*3/8')
grid on
ylim([1 10])
ylabel('VSWR')
xlabel('Frequency (GHz)')
xlim([0.6 1.4])
title('VSWR for Wide Antenna')
set(gca,'fontsize', 16);

%% Here be the currents
figure;
current(Ant, f);
view(90,0)
set(gca,'fontsize', 16);
title('Current on Thin Antenna')
%%%% WIDER DIPOLE CURRENT %%%%
figure;
current(Antw, f);
view(90,0)
set(gca,'fontsize', 16);
title('Current Distibution')

%% Plot some patterns
figure;
patternElevation(Ant,915e6)
title('E-plane of Thin Antenna')
figure;
patternElevation(Antw,915e6)
title('E-plane of Wide Antenna')
```

Publications

Peer-Reviewed Journals

J. Craig Prather, Yuan Meng, Michael Bolt, Tyler Horton, Mark L. Adams, Wireless Head Impact Monitoring System Utilizing Eye Movement as a Surrogate for Brain Movement, *International Journal of Electronics and Communications*, vol. 105, pp 54-61, April 2019.
https://doi.org/10.1016/j.aeue.2019.04.003

J. Craig Prather, Michael Bolt, Tyler Horton, Brent Bottenfield, Stuart Wentworth, and Mark L. Adams. Biomimetic Antenna Design for an Airborne Atmospheric Probe, *IEEE Transactions on Antennas and Propagation*, vol. 67, no. 1, pp. 48-55, Jan. 2019.
http://doi.org/10.1109/TAP.2018.2874773

Tyler Horton, Michael Bolt, J. Craig Prather, John Manobianco, Mark L. Adams. Airborne Sensor Network for Atmospheric Profiling, *Wireless Sensor Network*. vol. 10, no. 4, pp. 93-101, 2018.
http://doi.org/10.4236/wsn.2018.104005

Michael Bolt, J. Craig Prather, Haley Harrell, Tyler Horton, John Manobianco, and Mark L. Adams. Design and Testing of Novel Airborne Atmospheric Sensor Nodes, *IEEE Geoscience and Remote Sensing Letters*, vol. 15, no. 1, pp. 73-77, Jan. 2018.
http://doi.org/10.1109/LGRS.2017.2774203

J. Craig Prather, Michael Bolt, Haley Harrell, John Manobianco, and Mark L. Adams. Antenna Design for a Massive Multiple Input Environmental Sensor Network, *Digital Communications and Networks*, 2016, 2 (4):256-259.
http://doi.org/10.1016/j.dcan.2016.09.004

Thesis

J. Craig Prather. Dual Antenna Design for a Novel Airborne Probe. Masters Thesis, Auburn University, Auburn, Alabama, 2016.
http://hdl.handle.net/10415/5435

Conference Proceedings

J. Craig Prather and Stuart Wentworth. Design of Experiment in a Junior Level RF Systems Lab. *2018 ASEE Annual Conference and Exposition.*
https://peer.asee.org/30270

J. Craig Prather, Michael Bolt, Haley Harrell, Tyler Horton, John Manobianco, and Mark L. Adams. Atmospheric Probe for Real Time Weather Monitoring. *IMAPS 50th International Symposium on Microelectronics*, Fall 2017, Vol. 2017, No. 1, pp. 280-285.
https://doi.org/10.4071/isom-2017-WA45_133
Won Outstanding Student Paper Award
Won Best in Session

J. Craig Prather, Michael Bolt, Haley Harrell, Tyler Horton, and Mark L. Adams. (2017) Evaluation of an In Situ Atmospheric System for Real Time Weather Monitoring. *IMAPS Additional Conferences (Device Packaging, HiTEC, HiTEN, & CI-CMT)*, January 2017, Vol 2017, No. DPC, pp. 1-21.
https://doi.org/10.4071/2017DPC-TA3_Presentation2

J. Craig Prather, Michael Bolt, Brent Bottenfield, Thaddeus Roppel, Stuart Wentworth, and Mark L. Adams. Robotic Outreach to Attract Primary and Secondary Students to Engineering. *In 2017 ASEE Annual Conference and Exposition.*
https://peer.asee.org/28808

J. Craig Prather, Haley Harrell, Lesley Bartlett, and Stuart Wentworth. Enhanced Radio Lab Experience using ePortfolios. *In 2016 ASEE Annual Conference and Exposition*, June 2016.
https://peer.asee.org/26683

Mark L. Adams, Audrey Rose Shapland, Matthew Gutierrez, Haley Harrell, Jessica Blume, and Craig Prather. (2016) Enhancements of an In Situ Atmospheric System for Real Time Weather Monitoring. *IMAPS Additional Conferences (Device Packaging, HiTEC, HiTEN, & CI-CMT)*, January 2016, Vol. 2016, No. DPC, pp. 881-900.

Poster Presentations

J. Craig Prather and S. Wentworth, Design of Experiment in ECE, poster presented at the Conversations in Celebration of Teaching, Auburn University, January 25, 2019.

J. Craig Prather, M. Bolt, T. Horton, M. L. Adams, and S. Wentworth. Novel Atmospheric Sensor Antenna Design, poster presented at the Auburn University Graduate Engineering Research Showcase, Auburn University, October 24, 2018.

J. Craig Prather, M. Bolt, H. Harrell, T. Horton, B. Bottenfield, M. L. Adams, and S. Wentworth. Biomimetic Antenna Design, poster presented at the Auburn University Graduate Engineering Research Showcase, Auburn University, November 9, 2017.
Won Best of Department

H. Harrell, J. Craig Prather, and S. Wentworth, ePortfolios in an Electrical Engineering Lab, poster presented at the Conversations in Celebration of Teaching, Auburn University, January 27, 2017.

J. Craig Prather and M. Adams, Dual Antenna Design for a Novel Airborne Probe, poster presented at the Auburn University Graduate Engineering Research Showcase, Auburn University, October 20, 2016.